CURRENT-BLOCKADE PARTICLE-IMPACT ELECTROCHEMISTRY: A SINGLE-ENTITY APPROACH FOR DIGITAL (BIO)SENSING

Taghi Moazzenzade

CURRENT-BLOCKADE PARTICLE-IMPACT ELECTROCHEMISTRY: A SINGLE-ENTITY APPROACH FOR DIGITAL (BIO)SENSING

DISSERTATION

to obtain
the degree of doctor at the University of Twente,
on the authority of the rector magnificus,
prof. dr. ir. A. Veldkamp,
on account of the decision of the Doctorate Board
to be publicly defended
on Tuesday the 5th of September 2023 at 16.45 hours

by

Taghi Moazzenzade

born on the 17th of September, 1987
in Masal, Iran

This dissertation has been approved by:

Promotors
Prof. dr. S.G. Lemay
Prof. dr. ir. J. Huskens

The research described in this thesis was performed within the laboratories of the Bioelectronics (BE) and Molecular Nanofabrication (MNF) groups in the Faculty of Science and Technology (TNW), and MESA+ Institute at University of Twente.

Cover design: Taghi Moazzenzade
Printed by: Gildeprint
Lay-out: Taghi Moazzenzade
ISBN (print): 978-90-365-5769-6
ISBN (digital): 978-90-365-5770-2
URL: https://doi.org/10.3990/1.9789036557702

Graduation Committee:

Chair/secretary:	prof. dr. J.L. Herek (University of Twente)
Promotors:	prof. dr. S.G. Lemay (University of Twente)
	prof. dr. ir. J. Huskens (University of Twente)
Committee Members:	prof. dr. H. Zuilhof (Wageningen University)
	dr. F. Kanoufi (Université Paris Cité)
	dr. ir. S. Faez (Utrecht University)
	prof. dr. ir. L.I. Segerink (University of Twente)
	prof. dr. ir. P. Jonkheijm (University of Twente)

To Narges, Setiya, and my parents

Table of contents

Chapter 1	General introduction	1
Chapter 2	Stochastic electrochemistry at ultralow concentrations: the case for digital sensors	7
Chapter 3	Self-induced convection at microelectrodes via electroosmosis and its influence on impact electrochemistry	27
Chapter 4	Ring ultramicroelectrodes for current-blockade particle-impact electrochemistry	43
Chapter 5	Utilizing the oxygen reduction reaction in particle impact electrochemistry: a step toward mediator-free digital electrochemical sensors	65
Chapter 6	Designing a microparticle-based competitive displacement assay for the detection of ssDNA	81
Chapter 7	Single-entity electrochemistry for digital biosensing at ultralow concentrations	105
Chapter 8	Summary and outlook	123
Samenvatting		131
Scientific output		133
Acknowledgement		135

General introduction

Surface-based biosensors show great prospects for the detection and quantification of biomarkers as the molecular hallmarks of diseases.[1-3] These biosensors possess receptor-functionalized transducing element(s) in which the specific interaction of the biomarkers is transduced into a measurable signal in various readout mechanisms, such as optical,[4,5] electrochemical,[2,6] photoelectrochemical,[7] and mass changes.[8] These approaches enable the identification and quantification of biomolecules in biological fluids such as blood, plasma, urine, and saliva.[9] In particular, in cancer research, detecting biomarkers like circulating tumor cells (CTCs)[10], exosomes,[11] proteins,[12] RNA,[13] and circulating tumor DNA (ctDNA)[14] in biological fluids enables monitoring cancer progression, response to treatment, and drug resistance.[9] As an important goal, utilizing these sensors for the detection of biomarkers has shown great promise for the diagnosis of cancer at its early stages.[1,15]

Among surface-based biosensors, particle-based biosensors have shown great potential for detecting biomolecules at low concentrations.[16,17] These biosensors utilize micro- and nanoparticles as a label for signal amplification.[18,19] However, as the concentration of cancer biomarkers in biofluids can be extremely low, biosensors with high sensitivity and specificity are required.[20] This is a major challenge.

Particle-impact electrochemistry is a set of electrochemical methods that employ the collision of micro- and nanoscale particles in real time at the single-entity level.[21] This sensing approach utilizes miniaturized electrodes to evaluate the properties of individual particles such as their size, electroactivity, shape, and surface charge.[21] Collision of particles with the surface of an ultramicroelectrode (UME) leads to discrete signals in the current-time response.[20] Depending on the electroactivity of the particles and the electrodes, various types of discrete events such as step- or spike-like transients appear in the current-time curve.[21]

Among these approaches, current-blockade particle-impact electrochemistry studies the collision of non-electroactive particles at the single-entity level. In blockade impact, the proximity of insulating particles to the UME surface leads to discrete, step-like blockade signals in the current-time response.[22] This is because insulating particles hamper the diffusion-limited transport of redox mediators to the UME surface. The average step magnitude at a given concentration of redox molecule and electrode diameter, ΔI, is approximately proportional to the projected area of the particle on the electrode.[20,23] In addition, the particle concentration can be inferred from the frequency of current steps in a given regime of transport.[22,24]

This thesis aims to employ blockade impact electrochemistry as a single-entity method for the digital detection of single-strand DNA oligonucleotides. The motivation for this study is to design an electrochemical sensing method that can detect biomolecules in a digital on/off

manner instead of the conventional ensemble response.[20] Different aspects of blockade impact electrochemistry and particle-based sensing are discussed in the thesis; particle transport at different regimes in *Chapters 2* and *3*, electrode geometry and signal size distribution in *Chapter 4*, employing inner-sphere faradaic reaction in blockade impact in *Chapter 5*, and designing a competitive assay for particle-based detection in *Chapter 6*. The main goal is to expand the idea of single-entity biosensing and developing a high-sensitivity surface biosensor, a so-called digital biosensor, for the detection of biomarkers at ultralow concentrations in a practical time scale. This idea is discussed theoretically in *Chapter 2* and in more detail in *Chapter 7*.

In *Chapter 2*, single-entity electrochemical methods are introduced. This chapter first discuss the challenges regarding the detection of biomolecules at ultralow concentrations (pM-fM). It is discussed how employing miniaturized electrodes can be problematic for the detection of biomolecules at ultralow concentrations. The first part of the chapter revolves around the idea that, although small transducing elements possess high mass sensitivity, the mass transport of biomolecules to the electrode can be the main limiting step. The chapter concludes that parallelizing these single-entity elements can solve the mass transport problem leading to a new concept in sensing systems: digital sensors.

In *Chapter 3*, the effects of low supporting electrolyte concentrations have been investigated in blockade impact electrochemistry. In this chapter, examining the signal shape and microparticle trajectories provides insights into a fundamental aspect of electrochemical measurements at low salt regimes; electroosmotic flow (EOF). Finite element analysis and simultaneous optical-electrochemical measurement have been employed to evaluate the particle trajectory and signal shape at low salt concentrations. The chapter discusses how faradaic reactions at low supporting electrolyte concentrations induce convection in the fluid surrounding a UME due to EOF. In addition, it is investigated whether self-induced convection can become the dominant form of transport at low salt, violating the common assumption that convection can be neglected.

In *Chapter 4*, a new electrode geometry was designed and employed in blockade impact measurements. An intrinsic property of blockade impact measurements with a disk UME is that particles of a given diameter cause a broad distribution of current step sizes.[22,24] This is because the flux of the redox mediator is not uniform at the surface of the disk UME: the current density near the rim of the disk is higher than at the center. This inhomogeneous transport causes two problems. First, the current step size depends on the particle's landing location on the UME. Second, the higher density causes rearrangement of particles on the surface and false-positive signals. To overcome this limitation, a microfabricated ring UME was developed that is thinner than the particles to be detected.

Chapter 5 addresses a limitation in blockade impact electrochemistry for biosensing applications: employing synthetic redox mediators for signal generation. In this chapter, an inner-sphere faradaic reaction, the oxygen reduction reaction (ORR), has been employed in

blockade impact electrochemistry for detecting microparticles at physiological salt conditions. The motivation for utilizing the ORR in blockade impact is to enable single-entity electrochemical (bio)sensors without introducing synthetic redox mediators to circumvent their interference with biochemical processes and electrode fouling. The chapter investigates whether the concentration of O_2 in a physiological buffer (PBS) is sufficient for signal generation in the blockade impact method when using a proper material as the electrode. As a simple proof-of-concept, ORR-driven blockade impact electrochemistry is tested for the detection of positively charged microparticles in water. Due to the insensitivity of $\Delta I/I$ to the oxygen concentration, this method is a self-calibrating system for analyte detection at different oxygen concentrations in real-life samples.

In *Chapter 6*, a competitive assay is designed for microparticle dissociation from a surface *via* strand displacement of single-strand DNA oligonucleotides. The motivation for designing this competitive assay is to employ this method for DNA detection by blockade impact electrochemistry. The competitive assay is based on toehold-mediated strand displacement. Quartz crystal microbalance with dissipation monitoring (QCM-D) is employed for analysis of the competitive particle assay. Two different surface modification methods, thiol chemistry[25,26] and modified poly(l-lysine) (PLL) with oligo(ethylene glycol) (OEG),[27,28] have been used for immobilizing this dynamic actuator at the particle-substrate interface to dissociate particles specifically. In addition, suppressing non-specific adsorption in PLL chemistry has been investigated by employing the polyacrylic acid (PAA) polymer to invert the surface charge. Finally, particle dissociation from different modified surfaces is explained by the coupled resonator model in the particle binding step in QCM-D.

Chapter 7 investigates how parallelization can improve the concentration sensitivity in single-entity biosensors. The chapter indicates that, although single-entity transducing elements present infinite mass sensitivity, they need to be parallelized to possess a high concentration sensitivity. Hence, detecting biomolecules at ultralow concentrations can be achieved only when miniaturized elements work as parallelized addressable single-entity sensors: digital biosensors.

In the concluding chapter, particle-based biosensing by blockade impact electrochemistry is discussed. This chapter remarks on the challenges of utilizing microparticles for signal amplification blockade impact electrochemistry, and proposes directions for improving the sensitivity for future work.

References

(1) Arya, S. K.; Bhansali, S. Lung Cancer and Its Early Detection Using Biomarker-Based Biosensors. *Chem. Rev.* **2011**, *111*, 6783-6809.
(2) Labib, M.; Sargent, E. H.; Kelley, S. O. Electrochemical Methods for the Analysis of Clinically Relevant Biomolecules. *Chem. Rev.* **2016**, *116*, 9001-9090.
(3) Prakash, P.; Varma, M. A Pedagogical Introduction to Biomarker Detection in Surface-Based Biosensors. *J. Chem. Educ.* **2022**, *99*, 3694-3701.
(4) Kaur, B.; Kumar, S.; Kaushik, B. K. Recent Advancements In Optical Biosensors For Cancer Detection. *Biosens. Bioelectron.* **2022**, *197*, 113805.
(5) Borisov, S. M.; Wolfbeis, O. S. Optical Biosensors. *Chem. Rev.* **2008**, *108*, 423-461.
(6) Ronkainen, N. J.; Halsall, H. B.; Heineman, W. R. Electrochemical Biosensors. *Chem. Soc. Rev.* **2010**, *39*, 1747-1763.
(7) Zhao, W.-W.; Xu, J.-J.; Chen, H.-Y. Photoelectrochemical DNA Biosensors. *Chem. Rev.* **2014**, *114*, 7421-7441.
(8) Pohanka, M. Overview of Piezoelectric Biosensors, Immunosensors and DNA Sensors and Their Applications. *Materials* **2018**, *11*, 448.
(9) Ignatiadis, M.; Sledge, G. W.; Jeffrey, S. S. Liquid Biopsy Enters The Clinic — Implementation Issues And Future Challenges. *Nat Rev Clin Oncol* **2021**, *18*, 297-312.
(10) Visal, T. H.; den Hollander, P.; Cristofanilli, M.; Mani, S. A. Circulating Tumour Cells In The -Omics Era: How Far Are We From Achieving The 'Singularity'? *Br J Cancer* **2022**, *127*, 173-184.
(11) Zhou, B.; Xu, K.; Zheng, X.; Chen, T.; Wang, J.; Song, Y.; Shao, Y.; Zheng, S. Application Of Exosomes As Liquid Biopsy In Clinical Diagnosis. *Sig Transduct Target Ther* **2020**, *5*, 144.
(12) Ding, Z.; Wang, N.; Ji, N.; Chen, Z.-S. Proteomics Technologies For Cancer Liquid Biopsies. *Mol Cancer* **2022**, *21*, 53.
(13) Toden, S.; Goel, A. Non-Coding Rnas As Liquid Biopsy Biomarkers In Cancer. *Br J Cancer* **2022**, *126*, 351-360.
(14) Cescon, D. W.; Bratman, S. V.; Chan, S. M.; Siu, L. L. Circulating tumor DNA and liquid biopsy in oncology. *Nat Cancer* **2020**, *1*, 276-290.
(15) Hinestrosa, J. P.; Kurzrock, R.; Lewis, J. M.; Schork, N. J.; Schroeder, G.; Kamat, A. M.; Lowy, A. M.; Eskander, R. N.; Perrera, O.; Searson, D.; et al. Early-Stage Multi-Cancer Detection Using An Extracellular Vesicle Protein-Based Blood Test. *Commun Med* **2022**, *2*, 29.
(16) Mani, V.; Chikkaveeraiah, B. V.; Patel, V.; Gutkind, J. S.; Rusling, J. F. Ultrasensitive Immunosensor for Cancer Biomarker Proteins Using Gold Nanoparticle Film Electrodes and Multienzyme-Particle Amplification. *ACS Nano* **2009**, *3*, 585-594.
(17) Chinen, A. B.; Guan, C. M.; Ferrer, J. R.; Barnaby, S. N.; Merkel, T. J.; Mirkin, C. A. Nanoparticle Probes for the Detection of Cancer Biomarkers, Cells, and Tissues by Fluorescence. *Chem. Rev.* **2015**, *115*, 10530-10574.
(18) Shen, J.; Li, Y.; Gu, H.; Xia, F.; Zuo, X. Recent Development of Sandwich Assay Based on the Nanobiotechnologies for Proteins, Nucleic Acids, Small Molecules, and Ions. *Chem. Rev.* **2014**, *114*, 7631-7677.
(19) Saha, K.; Agasti, S. S.; Kim, C.; Li, X.; Rotello, V. M. Gold Nanoparticles in Chemical and Biological Sensing. *Chem. Rev.* **2012**, *112*, 2739-2779.

(20) Moazzenzade, T.; Huskens, J.; Lemay, S. G. Stochastic Electrochemistry at Ultralow Concentrations: the Case for Digital Sensors *Analyst* **2020**, *145*, 750-758.
(21) Sokolov, S. V.; Eloul, S.; Kätelhön, E.; Batchelor-McAuley, C.; Compton, R. G. Electrode–Particle Impacts: A Users Guide. *Phys. Chem. Chem. Phys.* **2017**, *19*, 28-43.
(22) Quinn, B. M.; van't Hof, P. G.; Lemay, S. G. Time-Resolved Electrochemical Detection Of Discrete Adsorption Events. *J. Am. Chem. Soc.* **2004**, *126*, 8360-8361.
(23) Deng, Z.; Elattar, R.; Maroun, F.; Renault, C. In Situ Measurement of the Size Distribution and Concentration of Insulating Particles by Electrochemical Collision on Hemispherical Ultramicroelectrodes. *Anal. Chem.* **2018**, *90*, 12923-12929.
(24) Fosdick, S. E.; Anderson, M. J.; Nettleton, E. G.; Crooks, R. M. Correlated Electrochemical and Optical Tracking of Discrete Collision Events. *J. Am. Chem. Soc.* **2013**, *135*, 5994-5997.
(25) Gong, P.; Levicky, R. DNA Surface Hybridization Regimes. *Proc. Natl. Acad. Sci. U.S.A.* **2008**, *105*, 5301-5306.
(26) Levicky, R.; Herne, T. M.; Tarlov, M. J.; Satija, S. K. Using Self-Assembly To Control the Structure of DNA Monolayers on Gold: A Neutron Reflectivity Study. *J. Am. Chem. Soc.* **1998**, *120*, 9787-9792.
(27) Di Iorio, D.; Marti, A.; Koeman, S.; Huskens, J. Clickable Poly-L-Lysine For The Formation Of Biorecognition Surfaces. *RSC Adv.* **2019**, *9*, 35608-35613.
(28) Movilli, J.; Rozzi, A.; Ricciardi, R.; Corradini, R.; Huskens, J. Control of Probe Density at DNA Biosensor Surfaces Using Poly(l-lysine) with Appended Reactive Groups. *Bioconjug. Chem.* **2018**, *29*, 4110-4118.

Stochastic electrochemistry at ultralow concentrations: the case for digital sensors

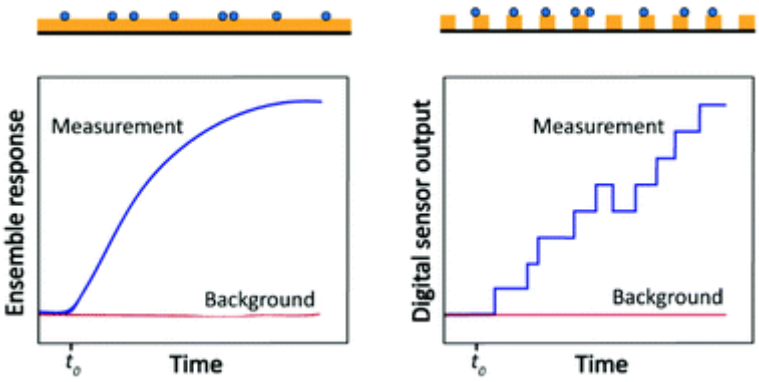

There is increasing demand, in particular from the medical field, for assays capable of detecting sub-pM macromolecular concentrations with high specificity. Methods for detecting single bio/macromolecules have already been developed based on a variety of transduction mechanisms, which represents the ultimate limit of mass sensitivity. Due to limitations imposed by mass transport and binding kinetics, however, achieving high concentration sensitivity additionally requires the massive parallelization of these single-molecule methods. This leads to a new sort of 'digital' assay based on large numbers of parallel, time-resolved measurements aimed at detecting, identifying and counting discrete macromolecular events instead of reading out an average response. In this chapter we first discuss the challenges inherent to trace-level detection and the motivations for developing digital assays. We then focus on the potential of recently developed single-entity impact electrochemistry methods for use in digital sensors. These have the inherent advantage of relying on purely electrical signals. They can thus in principle be implemented using integrated circuits to provide the parallelization, readout and analysis capabilities required for digital sensors.

The contents of this chapter are published as: Moazzenzade, T.; Huskens, J.; Lemay, S. G. Stochastic Electrochemistry at Ultralow Concentrations: the Case for Digital Sensors. *Analyst.* **2020**, *145*, 750-758.

2.1 Introduction

Healthcare is developing toward solutions attuned to the needs of patients based on real-time, precise and reliable data.[1] Important enablers are sensing devices to monitor, treat and coach patients. Particularly interesting in analyzing the molecular landscape of diseases such as cancer are so-called liquid biopsies, which probe circulating factors in biofluids including cell-free DNA (cfDNA) and RNA (cfRNA), proteins, extracellular vesicles, and circulating tumor cells (CTCs).[2] Among these biomarkers, oligonucleotides constitute the most important class for such applications.[2,3] To name but two examples, tumor DNA has been found to circulate freely in bodily fluids such as blood and urine,[4,5] and it has been proposed that drugs can be targeted against aberrant transcription pathways in cancer patients by monitoring messenger RNA expression levels.[6,7] As the natural concentrations of such biomarkers in liquid biopsies can be extremely low (pM or lower), analytical devices with ultrahigh sensitivities are required.

Surface-based "solid-phase" biosensors are an important class of analytical methods for biomolecular detection. In a typical surface-based biosensor, the sensing element surface is functionalized with receptors, and specific interaction of the biomarkers with these recognition elements transduce to a measurable signal. The quantity of analyte bound to the surface of the transducer is inferred through a variety of means that includes optical,[8] mechanical,[9,10] electrochemical,[11] and magnetic responses,[12] from which the concentration in the original sample can be deduced. Different strategies have been implemented for boosting the sensitivity of surface-based sensors *via* ameliorating the efficiency of the recognition elements,[13] transducers,[9] and electronic components of the biosensors. Nevertheless, designing reliable analytical approaches for the detection of analytes at low concentrations within a practical time scale remains demanding.

The affinity and kinetics of a particular biomarker-receptor pair are largely predetermined. However, targeted recognition elements have been engineered for increasing the binding affinity. For instance, substituting DNA with PNA improves the affinity *via* diminishing the electrostatic repulsion between the target DNA and the probe.[13] Similarly, introducing electrostatic interaction in the binding site residues of antibodies *via* mutagenesis can boost the affinity of antibodies against their antigens.[14] However, the mutations can destabilize the engineered antibodies thermodynamically and make them more vulnerable in further sensing procedures such as immobilization.[14,15] Besides, engineering the recognition elements for improving the affinity may undermine their selectivity. Hence, improving the performance of the recognition elements of the biosensors represents a major challenge. Boosting the response of the detection element (or, alternatively, suppressing aspecific background signals) is therefore an appealing alternative.

Many electrochemical methods have been developed to monitor the binding of biomolecules to surface-immobilized probes and thus provide specific recognition of targets. A broad array of chemical schemes further exists to assist binding of the target or boost sensitivity, often in combination with a DNA pre-amplification step in the case of nucleic acids.[16-21] These

platforms require minimum amounts of captured analyte to transduce the event to a measurable signal. As a rule these schemes employ 'macroscopic' electrochemical methods even when the readout electrodes are miniaturized, and efforts to downscale electrodes in the hope of higher sensitivity do not automatically translate into higher overall performance.
Here we first discuss the challenges of sensing at low concentrations (pM, fM) *via* ensemble sensing systems. We summarize the fundamental physical impediments and outline the key parameters in surface-based sensing: mass transport and kinetics. Here we use the detection of short oligonucleotides as a prototypical example application. We argue that there exists an opportunity for new sensor concepts based on massively parallelized single-entity measurements. Early attempts have focused mostly on optical methods.[22-24] Purely electrical transducers are however highly desirable since they can be implemented using integrated circuits to provide massive parallelization at low cost. In the second part of the chapter, we therefore review electrochemical sensory systems with the capability to sense analytes and particles with a digital on/off mode.

2.2 The challenges

Miniaturization can increase the sensitivity of a sensing element and improve its signal-to-noise ratio.[25,26] Moreover, it allows analysis of small-volume samples as encountered in single-cell analysis. However, in a sensor where the rate of analyte transport is limited by diffusion, shrinking the size of transducers decreases the probability of interaction between analytes and sensing elements. Hence, although scaled-down transducers can detect ultra-low amounts of analyte due to their superior electrostatic, photonic, electrochemical or magnetic performance, transport of analyte to the sensing element can quickly become the limiting factor for sensing over a practical time scale. This is illustrated in Figure 2. 1a, which shows that the expected collision rate between an analyte and a sensor quickly becomes impractical for nanoscale sensors at fM level concentrations.[27,28] For example, if we consider that the transducer is sensitive enough to convert the adsorption of one target molecule into a measurable signal, the time scale of sensing for transducers with a size of 1 μm to 10 nm ranges from ∼1 hour to ∼1 day for 1 fM samples. In addition, most sensors are unable to convert a single molecule interaction event and require more analyte molecules for a detectable signal. Hence, the time scale of the sensing becomes impractical and stability of the transducer, bioreceptor, and analytes become an issue.[27]

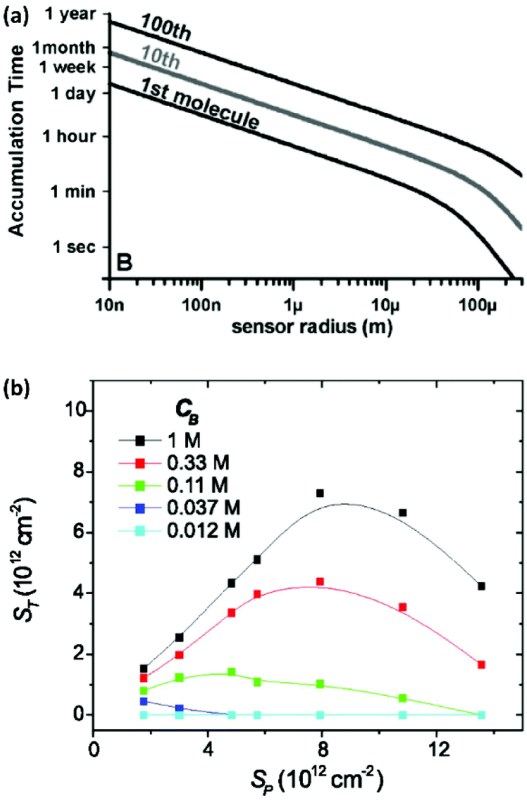

Figure 2.1. (a) Time required for the diffusive flux of 20 bp DNA molecules with a diffusion coefficient of 150 μm^2 s^{-1} to a hemispherical sensing element for an analyte concentration of 1 fM. Reprinted from ref. 27. (P. E. Sheehan and L. J. Whitman, *Nano Lett.*, 2005, **5**, 803–807). (b) Plot of hybridization of target oligonucleotide (S_T) as a function of probe density (S_p) and the buffer concentration C_B (here defined as moles per litre of phosphate in the pH 7.4 potassium phosphate buffer). Reprinted from ref. 33. (P. Gong and R. Levicky, *Proc. Natl. Acad. Sci. U. S. A.*, 2008, **105**, 5301–5306. Copyright 2008 National Academy of Sciences).

It is possible to decrease the time scale of collision between analytes and a sensing element *via* imposing fluid flow. This is not as effective as might be assumed, however. At high convective flow rates the collision rate between analyte and a sensor surface scales only as the 1/3 power of the flow velocity (in other words, increasing the pressure by a gigantic factor of 1000 results in a mere 10-fold gain in the collision rate).[29] In principle, this problem can be alleviated by implementing simultaneous fluid flow and nanoscale confinement to guide analyte toward the sensing elements.[30]

Returning to the diffusion-limited regime, the calculation in Figure 2.1a was performed with an optimistic assumption of instant and irreversible binding of analyte molecules to the sensing element. In practice, however, analytes do not necessarily adsorb to the sensor as

soon as they encounter its surface. Binding and dissociation of biomolecules, for example to a sensor surface, is a dynamic process.[31,32] This complicates sensor design because, besides the intrinsic kinetic properties of the recognition elements, their density is also an important factor (especially for highly charged capture probes such as DNA).[33,34] Hence, in addition to diffusional mass transport, the recognition event can also become the rate-limiting step.

To appreciate this point more fully, it is interesting to perform some numerical estimates. Consider a simple capture reaction described by Langmuir kinetics. The number of analytes bound to the surface, N_{bound}, after an incubation time, t, obeys

$$N_{\mathrm{bound}} = \frac{C^T}{K^{-1}+C^T}\left(1 - e^{-t/\tau}\right)N_{\mathrm{receptors}} \qquad (1)$$

Here $N_{\mathrm{receptors}}$ is the total number of receptors on the surface, C^{T} is the target concentration in solution, K is the binding constant and τ is the time constant for reaching equilibrium. For illustration purposes, we focus on short oligonucleotides (20 base pairs) under favourable binding conditions (probe density of 5×10^{12} molecules per cm^2). For this system, typical values are $K^{-1} \approx 1$ nM and $\tau \approx 10^5$ s.[35] For a trace target concentration of 1 pM, this means that only about 0.1% of the receptors are occupied at equilibrium ($t \to \infty$). For a measurement time of order 100 s, a desirable value for point-of-care applications, the occupancy $N_{\mathrm{bound}}/N_{\mathrm{receptors}}$ drops another factor 1000 such that only one receptor in a million is occupied. If one desires a statistically meaningful measurement, it is further necessary to count a significant number of targets. For *ca.* 10% statistical error, for example, this corresponds to $N_{\mathrm{bound}} \approx 100$ and, correspondingly, $N_{\mathrm{receptors}} \approx 10^8$. Importantly, these receptors occupy a significant surface area of order (100 μm)^2 and do not physically fit on a typical miniaturized sensor.[35] Increasing the density of probe DNA does not solve this problem since electrostatic repulsion hampers hybridization at high densities, as illustrated in Figure 2.1b. On the other hand, lowering the density below 1×10^{12} molecules per cm^2 is kinetically favorable and can overcome the electrostatic barrier.[33] However, in this regime the number of capture probes per surface area is low (1 molecule/100 nm^2), limiting sensitivity.[27]

The above back-of-the-envelope calculation represents an order-of-magnitude estimate for one specific system but highlights the difficulties inherent in pM-level detection. Measuring the average response of a mm-scale sensor to *ca.* 100 macromolecules represents a formidable challenge. Even if more favourable conditions are assumed, such as extending the incubation time, one is still left with a situation in which a small integer number of targets must generate a signal large enough to be detected. Achieving the absolute sensitivity to detect such a signal by optical, mechanical or electrical means is not the only challenge, however. The relatively long incubation times also mean that high stability is required to detect the signal against a background that includes slow fluctuations due to temperature stability as well as low-frequency (so-called 1/*f*) noise in the readout electronics. These sources of drift can easily mask a small signal.

2.3 Digital sensors

Driven by the nanotechnology explosion of the last decades, most fields of science have witnessed the development of methods for detecting and studying single entities ranging from artificial (nano)particles and living cells to individual (bio/macro)molecules. The detected signals differ from those commonly encountered in macroscopic measurements in that they are inherently stochastic. Instead of a smooth, average response, one observes sharp spikes, steps or other discrete features that reflect single-entity-scale events such as binding, conformational changes, bond breaking, *etc*. Detection of single analytes corresponds to the ultimate level of mass sensitivity. However, this does not automatically translate into a high sensitivity in terms of concentration. This is because, in order to achieve this absolute level of mass sensitivity, it is usually necessary for single-entity transducers to have dimensions that are not too much larger than those of the entity being detected. This limits their capabilities for trace-level analysis since, as we argued above, these applications require very large numbers of receptors that in turn require a large detection area. Therefore, in order to adapt single-entity techniques to ultra-low concentration measurements, it becomes necessary to employ large numbers of transducers in parallel. Each individual sensor is capable of detecting discrete microscopic events, but only in the aggregate do they provide the ability to detect ultra-low concentrations. This concept is illustrated schematically in Figure 2.2.

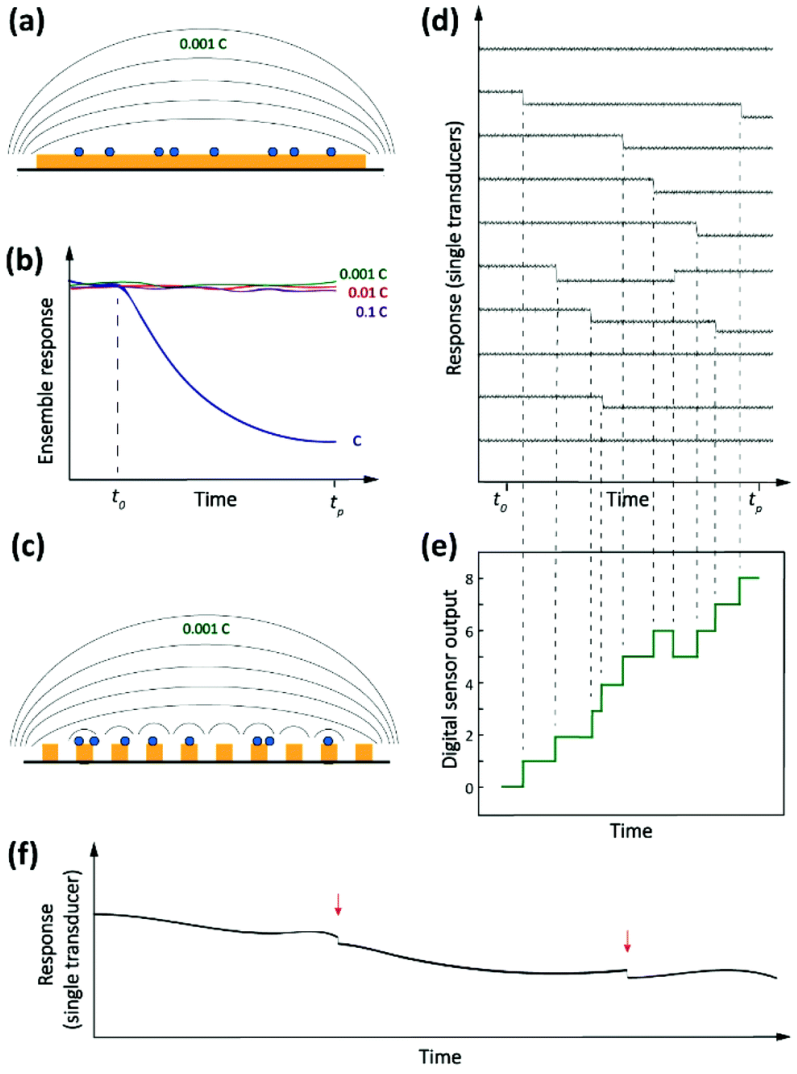

Figure 2.2. Conventional *versus* digital sensors. (a) Illustration of a conventional affinity sensor. Analytes are transported to the surface of the sensor where they are captured by recognition elements. (b) Response (electrical, optical, *etc*.) to an analyte introduced at time t_0. (c) Digital sensor consisting of a large number of separately addressable single-entity sensor elements. (d) Response of the individual elements. (e) Overall response of the digital sensor which mimics the conventional sensor. (f) An advantage of single-entity measurements is that it is possible to recognize sudden, discrete events (here the steps marked by arrows) in the presence of significant low-frequency background noise.

How would a digital[36] sensor work for measuring concentration? Returning to our example of Langmuir kinetics for short DNA oligos, note that at short times ($t \ll \tau$) eqn (1) simplifies to

$$N_{\text{bound}} = N_{\text{receptors}} k_{\text{on}} C^{\text{T}} t \qquad (2)$$

where $k_{\text{on}} \approx 10^4\ \text{M}^{-1}\ \text{s}^{-1}$ is a typical binding on-rate for this system.[35] Eqn (2) indicates that the bulk concentration is simply proportional to the ratio N_{bound}/t, which can be monitored by the digital sensor by counting the N_{bound} events.

There is an additional subtle advantage to using single-entity transducers. We already mentioned that real-world detection techniques suffer from background drift. If a single-entity signal is measured in real time, however, drift and offsets become much less of an issue. It is much easier to detect sharp, sudden events in the presence of slow drift than it is to detect a small change in response after a long time interval. This is illustrated in Figure 2.2f.

We refer to the combination of discrete, time-resolved signals and high degree of parallelization as digital sensors, in analogy to the discrete and parallelized nature of digital integrated circuits.

Electrochemical methods are in principle well-suited to the implementation of digital sensors. This is because parallelization can be achieved relatively straightforwardly and in a cost-effective manner if implemented in the form of integrated circuits. This renders single-entity electrochemical methods an interesting candidate for attempting to build new sensors based on the principle of digital detection.

2.4 The Coulter counter, a classic stochastic electrochemical assay

A classic example of a stochastic electrochemical sensing system for single-entity detection and characterization is the resistive pulse sensing (RPS). This system is the advanced exemplar of the classic Coulter counter approach, originally introduced in 1953.[37] In Coulter counters, particles passing through a nano/micro pore cause discrete transients in the ionic current flowing through the pore. The sensing system consists of two electrolyte-filled reservoirs separated by an insulating membrane and possessing a single micro-nanoscale pore. The two reservoirs contain electrodes that are used for applying a transmembrane potential difference across the nanopore, such that ions flow through the pore and an ionic current (i_{c}) is established. Particles driven through the pore temporarily block the ionic current by displacing the conductive electrolyte (Figure 2.3a). The resulting transient increase in the electrical resistance leads to a detectable step-like decrease in the current-time response. However, the decreased current pulse is ephemeral and the current is restored to its baseline value immediately after the particle has passed entirely through the pore (Figure 2.3b). The magnitude, duration and frequency of the current-time resistive pulse provide information about the size, shape, surface charge, and concentration of the

particles.[38] Initially applied to micron-scale analytes such as cells, this approach developed further following progress in micro- and nanofabrication techniques[39,40] and was extended to characterize the size, geometry, surface charge, and mass transport kinetics of nanoscale objects and macromolecules.

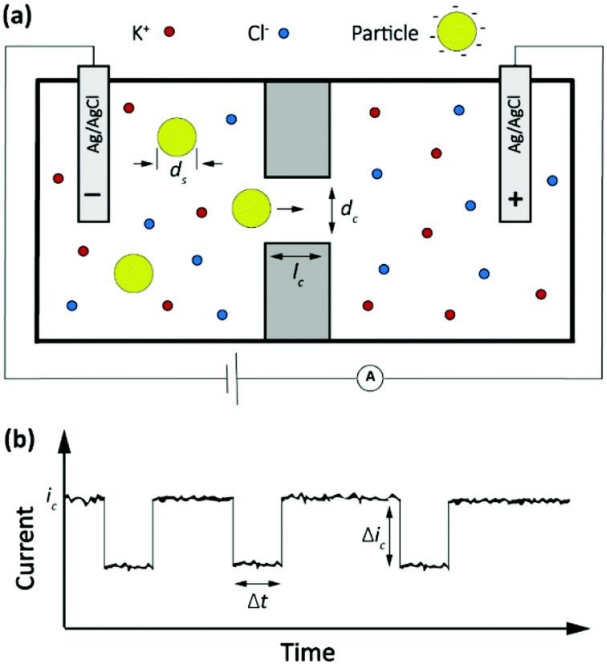

Figure 2.3. (a) Schematic representation of a resistive pulse sensing system. (b) The current transient properties upon particles passing through the pore.

The amplitude of pulses upon blocking the ionic current, Δi_c, depends on the geometries of the pore and of the particle as given by the equation

$$\frac{\Delta i_c}{i_c} = S(d_c, d_s)\frac{d_s^3}{l_{c'} d_c^2} \qquad (3)$$

Here i_c is the baseline current, d_s is the diameter of particle, d_c is the pore size, $l_{c'}$ is the channel length considering the "end effect" ($l_{c'} = l_c + 0.8\, d_c$), and $S(d_c,d_s)$ is a numerical correction factor.[39,41,42]

The frequency of the pulses is directly proportional to the particle concentration.[43] In a channel with well-defined geometric shape and known chemical properties, the pulse duration, Δt, and characteristic signature have been associated with the charge density of nano objects,[44] the shape and structure of macromolecules[45] and the translocation dynamics of asymmetric nanoparticles.[46] For instance, in a biological nanopore (α-hemolysin protein channel) the blockade lifetime is related to the length of translocating polynucleotides.[43] In

addition, the pulse duration and characteristic signature can provide information about the molecular configuration and folding.[45] More recently this approach has been extended to a broad palette of analytes, culminating in the sequencing of nucleic acids.[47]

2.5 Impact stochastic electrochemistry

Another, more recent approach to detect single entities in micro- or nanoscale regions is impact stochastic electrochemistry. This is also an amperometric sensing approach in which the collision of particles with an electrode surface leads to discrete changes in the current-time response. Depending on the electrical or catalytic properties of the colliding particles, different types of signals can be detected in the form of characteristic step- or spike-like transients that appear in the current curve. Different types of information such as size, electroactivity, shape, and surface charge can be extracted from these current transients. While still in its infancy, exploiting these methods for macromolecular detection has been demonstrated in specific cases.[36,48-50] Three main classes of approaches based on the impact principle are current blockade, current amplification and capacitive impact, as summarized in Figure 2.4.

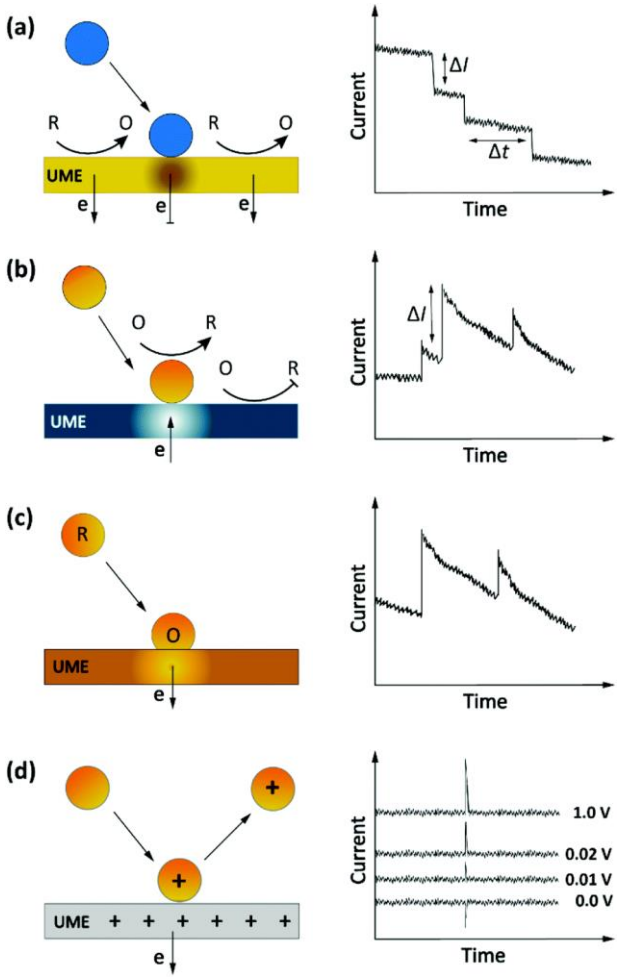

Figure 2.4. Schematic representation of impact stochastic electrochemical sensors. (a) Current blockade impact:[51] step-like decreases in the current–time transients upon collision of the insulator particles. (b) Mediated faradaic impact: staircase-shaped increases in the current–time transient due to a redox reaction catalyzed by the nanoparticles. The catalytic nanoparticles play the role of working electrodes to carry out a heterogenous electron-transfer reaction while the inert electrode works solely to establish electrical contact to the nanoparticles.[52] (c) Direct faradaic impact: electron transfer takes place by electro-dissolution of particles reaching the electrode. The measured current change upon the collision is proportional to the number of atoms in the cluster.[53] (d) Capacitive impact: current transients upon particle collision result from either charging of the particle or obstruction of the electrical double layer of the electrode. In both cases the polarity of the spikes can invert upon changing the applied potential.

2.5.1 Current blockade impact

In blocking-based measurements, binding of individual non-electroactive particles to the electrode surface hampers the mass transfer of a redox mediator present in the solution. Under potentiostatic control, mass-transport-limited oxidation or reduction of this mediator at the surface of a miniaturized electrode leads to a steady-state current. In an electrolyte solution containing micro/nanoparticles, proximity of the particles to the electrode surface blocks the steady-state mass transport of redox molecules. Hence, stochastic interaction of particles with the electrode surface can be sensed as discrete, step-like decreases in the current-time response (Figure 2.4a).[51] The average step magnitude, ΔI, is approximately proportional to the projected area of the particle on the electrode, inversely proportional to the diameter of the electrode and proportional to the concentration of the redox mediator.

As a complication, due to the nonuniformity in diffusive flux of the redox molecules, particles adsorbing on the edges of the disk electrode block a higher current density and therefore lead to larger step heights.[49,51] Furthermore, due to the difference in current density between the edge and center of the disk electrode, the dynamic displacement of adsorbed particles from the center to the edge of the electrode may lead to unwanted steps in the current response that are not representatives of adsorption events.[54]

It is interesting to note that the current blockade mechanism is conceptually related to that of the Coulter counter, as sketched in Figure 2.5. In the Coulter counter, the migration of ions is obstructed by the analyte particle, whereas it is the diffusion of the redox mediator that is obstructed in current blockade. Because both the electrostatic potential and the mediator concentration profile are governed by the Laplace equation, however, the distortion of the migrational or diffusional fluxes around the particles are very similar in the two cases.

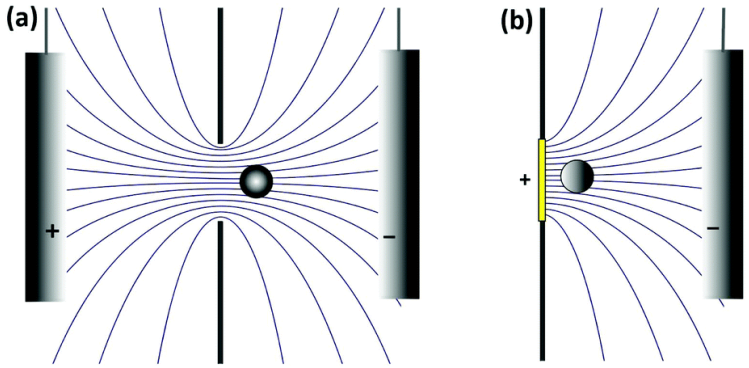

Figure 2.5. Schematic representation of the analogy between the Coulter counter and current blockade. (a) Electric field lines are distorted by the presence of a particle in the Coulter counter, leading to a change in migrational current. (b) The diffusive flux of the redox mediator is distorted in a similar manner during current blockade.

2.5.2 Current amplification impact

The impact detection approach has also been applied to studies of the electrocatalytic activity of metal nanoparticles at the single particle level. Here the sensing mechanism is faradaic reactions involving the (usually conductive) nanoparticles.[55] These sensing systems can be separated into two distinct classes: mediated impact and direct impact.[53]

Mediated faradaic impact In this approach, electrocatalytic nanoparticles are detected upon collision *via* a redox reaction that is catalyzed by the particles (Figure 2.4b). Due to kinetic limitations of the electrode at the applied potential, faradaic reactions can only take place at the surface of adsorbed particles that are in contact with the electrode. In this scenario, the electrode acts only as electrical contact to the nanoparticles. Time traces of signal amplification impact events appear as discrete staircase-shaped increases or spikes in the steady-state current.[52] Signal amplification occurs in the sense that a single collision leads to many electrocatalytic events.

The current step magnitude upon diffusion-controlled electrocatalysis of the redox species on the adsorbed particle on planar electrode can be expressed by the following equation:

$$\Delta I = 4\pi(\ln 2)nFDCr \qquad (4)$$

where F is the Faraday constant, D is the diffusion coefficient of redox species at concentration C, and r is the radius of the metal nanoparticle.[56] The spike size and shape can provide information about the size, residence time of binding, and interaction nature of the particles. In particular, the amplitude of the current transients is related to the particle size. Moreover, the capping agent and the geometry of the nanoparticle also affect the step size.[52] The time scale of the current decay in the spikes may be affected by reaction kinetics and also with the nature of the particle–surface interaction.[56]

Direct faradaic impact Direct reduction or oxidation of metal nanoparticles at UMEs has also been applied for studying the size distribution of these particles.[57] Since oxidation or reduction of the nanoparticles occurs in a defined potential window, collision events can be employed for characterizing these nanoclusters by measuring the transferred charge (Figure 2.4c). The area under the observed spikes in the current-time response upon oxidation or reduction of the nanoparticles is equal to the number of transferred electrons between the electrode and the collided nanocluster, which is in turn proportional to the absolute number of atoms.[57,58] For example, the following equation represents the charged passed per current spike upon complete oxidation of spherical Ag nanoparticles on the electrode surface.

$$Q_{\max} = \frac{4F\pi\rho_p r_{np}^3}{3A_r} \qquad (5)$$

In this equation, Q_{max} is the maximum transferred charge, ρ_p is the mass density of the nanoparticle, r_{np} is the particle radius, and A_r is the relative atomic mass.[57] This approach has

been extended to sensing of non-metallic nanomaterials and electrochemical size monitoring of organic nanoparticles has been studied.[59]

2.5.3 Capacitive impact

Particle collisions can have additional consequences beyond faradaic charge transfer and current blockade. Collisions can also remove charge from the electrode surface or disrupt its electrical double layer, a process known as capacitive impact. Both conductive and insulating particles can exhibit this phenomenon in different manners.[53] For example, this sensing system has been implemented for characterizing the capacitive properties of graphene nanoplatelets (GNPs). In this approach, the stochastic collision of GNPs with an electrode modify the charge at the electrode–electrolyte interface. Depending on the applied potential, electrons can leave or enter the electrode to compensate this charge redistribution.[60] These events can be observed as transients in the current-time response (Figure 2.4d). Moreover, the polarity of the spikes will be inverted by using an applied potential that is either higher or lower than the potential of zero charge (PZC) of either the electrode or the particle, as shown in Figure 2.4d.[61] Determining the PZC of colliding particles can also help to elucidate the nature of the electric double layer of electrodes.[60]

2.6 Analyte transport in impact electrochemistry

Before they can be detected by impact electrochemistry, analyte particles must make their way to the surface of the electrode. In general this mass transport includes contributions from diffusion, migration and convection:

$$\mathbf{J} = \mathbf{J_{diff}} + \mathbf{J_{mig}} + \mathbf{J_{conv}} = -D\nabla C + \mu C\mathbf{E} + C\mathbf{v} \qquad (6)$$

Here **J**, C, D and μ are the local flux, the concentration, the diffusion coefficient and the electrophoretic mobility of the particles, respectively, **E** is the electric field and **v** the electrolyte flow velocity. Impact electrochemistry measurements usually do not involve convection so we take **v** = 0 and ignore this contribution here.

In a well-designed electrochemical experiment, the electric field is usually negligible through the use of a supporting electrolyte. Migration may however play a larger role in impact experiments. This is because the electrophoretic mobility of colloidal particles is of the same order of magnitude as that of small ions and largely independent of particle size, whereas the diffusion coefficient scales as the inverse of the particle size. Thus, the larger the particle, the more important the electric field becomes. This counterintuitive observation can be used to selectively influence the rate of mass transport, for example in current blockade impact experiments.[51]

It is thus useful to estimate the conditions under which migration dominates over diffusion. For a hemispherical electrode of radius r_0, the electric field has radial symmetry with magnitude

$$E_r = \frac{r_0 V_{\mathrm{ohm}}}{r^2} \qquad (7)$$

Here r is the radial distance from the center of the electrode and V_{ohm} is the potential difference between the electrode and bulk solution (*i.e.* the ohmic drop). Assuming that particles that reach the electrode are immobilized or consumed, the corresponding total collision rate from migration, Γ_{mig}, is

$$\Gamma_{\mathrm{mig}} = 2\pi\mu C_0 r_0 V_{\mathrm{ohm}} \qquad (8)$$

Here C_0 is the bulk particle concentration (this simplification ignores the depletion near the electrode caused by diffusion but this is sufficient to estimate the crossover between diffusion and migration). The corresponding collision rate from diffusion is

$$\Gamma_{\mathrm{diff}} = 2\pi D C_0 r_0 \qquad (9)$$

This calculation indicates that the Γ_{mig} becomes larger than Γ_{diff} when

$$V_{\mathrm{ohm}} > \frac{D}{\mu} \qquad (10)$$

which depends only on the properties of the particle and is independent of the electrode size. For small monovalent ions, this result simplifies *via* the Einstein relation to $V_{\mathrm{ohm}} > k_B T/e$, where k_B is the Boltzmann constant, T is the absolute temperature and e is the electron charge. At room temperature this corresponds to ≈27 mV. This simple relation no longer holds for larger particles, however. For a spherical colloidal particle $D = k_B T/6\pi\eta r_p$, where η is the dynamic viscosity of water and r_p is the particle radius. The electrophoretic mobility is instead given by the Smoluchowski equation, $\mu = \varepsilon\zeta/\eta$, where ε is the permeability of water and ζ is the zeta potential of the particle. Importantly, this indicates that μ is independent of r_p. Combining these results yields for the case of spherical particles

$$V_{\mathrm{ohm}} > \frac{k_B T}{6\pi\epsilon r_p \zeta} \qquad (11)$$

The critical value of V_{ohm} above which migration dominates thus decreases with increasing r_p. Numerical substitution indicates that the critical potential is ≈10 μV for a particle with r_p = 1 μm and ζ = −27 mV. It is thus possible for migration to be negligible for the transport of a small redox mediator while it dominates the motion of larger particles.

How large is V_{ohm}? This of course depends on the nature of the experiment. We first consider the Coulter counter. Here V_{ohm} originates from the potential applied between the two reservoirs, V_{app}. This potential can be divided between the resistance of the pore itself, R_{pore}, and the resistance of the solution on either side of the pore (the so-called access resistance), R_{acc}. The ohmic drop is then $V_{\mathrm{ohm}} = V_{\mathrm{app}} R_{\mathrm{acc}}/(R_{\mathrm{pore}} + 2R_{\mathrm{acc}})$. For a pore that is much shorter than its diameter, $R_{\mathrm{pore}} \ll R_{\mathrm{acc}}$ and thus $V_{\mathrm{ohm}} \approx V_{\mathrm{app}}/2$. It is thus rather straightforward to apply sufficient potential to ensure that transport to the pore is driven by electrophoresis rather than diffusion, as is commonly done in Coulter counters.

We now turn to current blockade electrochemistry. Here an ohmic drop develops because salt ions must move to compensate the charge injected by oxidation or reduction of the redox mediator. The ohmic drop is then $R_{acc}I$, where I is the faradaic current. The access resistance for a disk electrode is given by $R_{acc} = \rho/4r_0$, where ρ is the resistivity of the electrolyte, while the diffusion-limited mediator current is $I = 4nFC_mD_mr_0$, where n is the number of electrons transferred, C_m is the mediator concentration and D_m is the mediator diffusion coefficient. This yields

$$V_{\mathrm{ohm}} = n\rho F C_m D_m \qquad (12)$$

Interestingly, this result is independent of the electrode radius. For 1 mM ferrocene dimethanol in aqueous 0.3 M KCl solution ($n = 1$, $D \approx 5 \times 10^{-10}$ m^2 s^{-1}, $\rho \approx 0.2$ Ωm) eqn (12) gives $V_{ohm} \approx 10$ μV. Comparing this value with eqn (11) indicates that transport of particles with $r_0 > 1$ μm will be dominated by migration under these conditions. Increasing the mediator concentration or decreasing the supporting electrolyte concentration (thus increasing ρ) will cause smaller particles to become controlled by migration. Also note that the direction of the migrational flux depends on the polarity of V_{ohm}. For negatively charged particles ($\zeta < 0$) an oxidation reaction for the mediator attracts the particles toward the electrode while a reduction reaction repels them, preventing access to the electrode at sufficiently high reduction currents.

Other forms of impact electrochemistry besides current blockade do not require a mediator and are thus in principle free of migrational effects. In practice, however, unwanted background reactions take place to some degree, leading to a finite faradaic current. The magnitude of the ohmic drop can again be estimated as $V_{ohm} = R_{acc}I = \rho I/4r_0$, where in this case I is the experimentally measured background current.

2.7 Summary and outlook

In this chapter we have discussed some of the main challenges inherent in detecting trace amounts of macromolecular species with high degrees of specificity using electrochemical methods. We have argued that, while recently developed nanoscale assays allow detecting single entities ranging from nanoparticles to bio/macromolecules, these cannot be directly employed for analytical applications at ultra-low concentrations. Doing so will further require massive parallelization in the form of large numbers of individually addressable electrodes and readout systems, thus creating a ‘digital’ assay based on the counting of single discrete events. Electrochemical methods are well suited for this purpose as they can be integrated with microfabricated circuitry to implement this parallelization. We then focused on impact electrochemistry, a set of methods for detecting and characterizing single micro- and nanoscale entities. While this has not yet been achieved experimentally, these methods provide a route for the realization of an electrochemical digital sensor. An important question has not yet been addressed by the impact electrochemistry community, however: how does one best translate a biomolecular recognition event into an impact electrochemistry signal?

2.8 References

(1) Christensen, C. M.; Grossman, J. H.; Hwang, J. Introduction. In *The Innovator's Prescription: A Disruptive Solution for Health Care*, McGraw-Hill Education, 2018.
(2) Siravegna, G.; Marsoni, S.; Siena, S.; Bardelli, A. Integrating Liquid Biopsies Into The Management Of Cancer. *Nat Rev Clin Oncol* **2017**, *14*, 531-548.
(3) Sassolas, A.; Leca-Bouvier, B. D.; Blum, L. J. DNA Biosensors and Microarrays. *Chem. Rev.* **2008**, *108*, 109-139.
(4) Bellassai, N.; Spoto, G. Biosensors For Liquid Biopsy: Circulating Nucleic Acids To Diagnose And Treat Cancer. *Anal Bioanal Chem.* **2016**, *408*, 7255-7264.
(5) Das, J.; Ivanov, I.; Montermini, L.; Rak, J.; Sargent, E. H.; Kelley, S. O. An Electrochemical Clamp Assay For Direct, Rapid Analysis Of Circulating Nucleic Acids In Serum. *Nature Chemistry* **2015**, *7*, 569-575.
(6) Verhaegh, W.; van Ooijen, H.; Inda, M. A.; Hatzis, P.; Versteeg, R.; Smid, M.; Martens, J.; Foekens, J.; van de Wiel, P.; Clevers, H.; et al. Selection of Personalized Patient Therapy through the Use of Knowledge-Based Computational Models That Identify Tumor-Driving Signal Transduction Pathways. *Cancer Res* **2014**, *74*, 2936-2945.
(7) Verhaegh, W.; Van de Stolpe, A. Knowledge-Based Computational Models. *Oncotarget* **2014**, *5*, 5196-5197.
(8) Liedberg, B.; Nylander, C.; Lunström, I. Surface Plasmon Resonance For Gas Detection And Biosensing. *Sens. Actuators* **1983**, *4*, 299-304.
(9) Fritz, J.; Baller, M. K.; Lang, H. P.; Rothuizen, H.; Vettiger, P.; Meyer, E.; -J. Güntherodt, H.; Gerber, C.; Gimzewski, J. K. Translating Biomolecular Recognition into Nanomechanics. *Science* **2000**, *288*, 316-318.
(10) Mukhopadhyay, R.; Lorentzen, M.; Kjems, J.; Besenbacher, F. Nanomechanical Sensing of DNA Sequences Using Piezoresistive Cantilevers. *Langmuir* **2005**, *21*, 8400-8408.
(11) Idili, A.; Amodio, A.; Vidonis, M.; Feinberg-Somerson, J.; Castronovo, M.; Ricci, F. Folding-Upon-Binding and Signal-On Electrochemical DNA Sensor with High Affinity and Specificity. *Anal. Chem.* **2014**, *86*, 9013-9019.
(12) Hien, L. T.; Quynh, L. K.; Huyen, V. T.; Tu, B. D.; Hien, N. T.; Phuong, D. M.; Nhung, P. H.; Giang, D. T. H.; Duc, N. H. DNA-Magnetic Bead Detection Using Disposable Cards And The Anisotropic Magnetoresistive Sensor. **2016**, *7*, 045006.
(13) Briones, C.; Mateo-Marti, E.; Gómez-Navarro, C.; Parro, V.; Román, E.; Martín-Gago, J. A. Ordered Self-Assembled Monolayers of Peptide Nucleic Acids with DNA Recognition Capability. *Phys. Rev. Lett.* **2004**, *93*, 208103.
(14) Fukunaga, A.; Tsumoto, K. Improving The Affinity Of An Antibody For Its Antigen Via Long-Range Electrostatic Interactions. *Protein Eng., Des. Sel.* **2013**, *26*, 773-780.
(15) Fukunaga, A.; Maeta, S.; Reema, B.; Nakakido, M.; Tsumoto, K. Improvement of antibody affinity by introduction of basic amino acid residues into the framework region. *Biochem Biophys Rep* **2018**, *15*, 81-85.
(16) Hansen, J. A.; Mukhopadhyay, R.; Hansen, J. Ø.; Gothelf, K. V. Femtomolar Electrochemical Detection of DNA Targets Using Metal Sulfide Nanoparticles. *J. Am. Chem. Soc.* **2006**, *128*, 3860-3861.
(17) Miao, P.; Tang, Y.; Yin, J. Microrna Detection Based On Analyte Triggered Nanoparticle Localization On A Tetrahedral DNA Modified Electrode Followed By Hybridization Chain Reaction Dual Amplification. *Chem. Commun.* **2015**, *51*, 15629-15632.

(18) Hill, H. D.; Mirkin, C. A. The Bio-Barcode Assay For The Detection Of Protein And Nucleic Acid Targets Using Dtt-Induced Ligand Exchange. *Nat. Protoc.* **2006**, *1*, 324-336.
(19) Liu, G.; Wan, Y.; Gau, V.; Zhang, J.; Wang, L.; Song, S.; Fan, C. An Enzyme-Based E-DNA Sensor for Sequence-Specific Detection of Femtomolar DNA Targets. *J. Am. Chem. Soc.* **2008**, *130*, 6820-6825.
(20) Zhang, J.; Song, S.; Zhang, L.; Wang, L.; Wu, H.; Pan, D.; Fan, C. Sequence-Specific Detection of Femtomolar DNA via a Chronocoulometric DNA Sensor (CDS): Effects of Nanoparticle-Mediated Amplification and Nanoscale Control of DNA Assembly at Electrodes. *J. Am. Chem. Soc.* **2006**, *128*, 8575-8580.
(21) Xiao, Y.; Lubin, A. A.; Baker, B. R.; Plaxco, K. W.; Heeger, A. J. Single-step electronic detection of femtomolar DNA by target-induced strand displacement in an electrode-bound duplex. *Proc. Natl. Acad. Sci. U. S. A.* **2006**, *103*, 16677-16680.
(22) Johnson-Buck, A.; Su, X.; Giraldez, M. D.; Zhao, M.; Tewari, M.; Walter, N. G. Kinetic Fingerprinting To Identify And Count Single Nucleic Acids. *Nat. Biotechnol.* **2015**, *33*, 730-732.
(23) Visser, E. W. A.; Yan, J.; van Ijzendoorn, L. J.; Prins, M. W. J. Continuous Biomarker Monitoring By Particle Mobility Sensing With Single Molecule Resolution. *Nat. Commun.* **2018**, *9*, 2541.
(24) Jing, W.; Wang, Y.; Yang, Y.; Wang, Y.; Ma, G.; Wang, S.; Tao, N. Time-Resolved Digital Immunoassay for Rapid and Sensitive Quantitation of Procalcitonin with Plasmonic Imaging. *ACS Nano* **2019**, *13*, 8609-8617.
(25) Zhang, Y.; Zhang, B.; White, H. S. Electrochemistry of Nanopore Electrodes in Low Ionic Strength Solutions. *J. Phys. Chem. B* **2006**, *110*, 1768-1774.
(26) Viani, M. B.; Schäffer, T. E.; Chand, A.; Rief, M.; Gaub, H. E.; Hansma, P. K. Small Cantilevers For Force Spectroscopy Of Single Molecules. *J. Appl. Phys.* **1999**, *86*, 2258-2262.
(27) Sheehan, P. E.; Whitman, L. J. Detection Limits for Nanoscale Biosensors. *Nano Lett.* **2005**, *5*, 803-807.
(28) Nair, P. R.; Alam, M. A. Performance Limits Of Nanobiosensors. *Appl. Phys. Lett.* **2006**, *88* (23).
(29) Squires, T. M.; Messinger, R. J.; Manalis, S. R. Making It Stick: Convection, Reaction And Diffusion In Surface-Based Biosensors. *Nat. Biotechnol.* **2008**, *26* (4), 417-426.
(30) Fritzsche, J.; Albinsson, D.; Fritzsche, M.; Antosiewicz, T. J.; Westerlund, F.; Langhammer, C. Single Particle Nanoplasmonic Sensing in Individual Nanofluidic Channels. *Nano Lett.* **2016**, *16*, 7857-7864.
(31) Goh, C.-S.; Milburn, D.; Gerstein, M. Conformational Changes Associated With Protein–Protein Interactions. *Curr. Opin. Struct. Biol.* **2004**, *14*, 104-109.
(32) Ouldridge, T. E.; Šulc, P.; Romano, F.; Doye, J. P. K.; Louis, A. A. DNA Hybridization Kinetics: Zippering, Internal Displacement And Sequence Dependence. *Nucleic Acids Res.* **2013**, *41*, 8886-8895.
(33) Gong, P.; Levicky, R. DNA Surface Hybridization Regimes. *Proc. Natl. Acad. Sci. U.S.A.* **2008**, *105*, 5301-5306.
(34) Simon, L.; Gyurcsányi, R. E. Multiplexed Assessment Of The Surface Density Of DNA Probes On DNA Microarrays By Surface Plasmon Resonance Imaging. *Anal. Chim. Acta* **2019**, *1047*, 131-138.

(35) Tymoczko, J.; Schuhmann, W.; Gebala, M. Electrical Potential-Assisted DNA Hybridization. How to Mitigate Electrostatics for Surface DNA Hybridization. *ACS Appl. Mater. Interfaces* **2014**, *6*, 21851-21858.
(36) Dick, J. E.; Hilterbrand, A. T.; Strawsine, L. M.; Upton, J. W.; Bard, A. J. Enzymatically Enhanced Collisions On Ultramicroelectrodes For Specific And Rapid Detection Of Individual Viruses. *Proc. Natl. Acad. Sci. U. S. A.* **2016**, *113*, 6403-6408.
(37) Coulter, W. H. Means for counting particles suspended in a fluid. USA 1953.
(38) Don, M. The Coulter Principle: Foundation of an Industry. *JALA* **2003**, *8*, 72-81.
(39) DeBlois, R. W.; Bean, C. P. Counting and Sizing of Submicron Particles by the Resistive Pulse Technique. *Rev. Sci. Instrum.* **2003**, *41*, 909-916.
(40) Li, J.; Stein, D.; McMullan, C.; Branton, D.; Aziz, M. J.; Golovchenko, J. A. Ion-Beam Sculpting At Nanometre Length Scales. *Nature* **2001**, *412*, 166-169.
(41) Henriquez, R. R.; Ito, T.; Sun, L.; Crooks, R. M. The Resurgence Of Coulter Counting For Analyzing Nanoscale Objects. *Analyst* **2004**, *129*, 478-482.
(42) Sun, L.; Crooks, R. M. Single Carbon Nanotube Membranes: A Well-Defined Model for Studying Mass Transport through Nanoporous Materials. *J. Am. Chem. Soc.* **2000**, *122*, 12340-12345.
(43) Kasianowicz, J. J.; Brandin, E.; Branton, D.; Deamer, D. W. Characterization Of Individual Polynucleotide Molecules Using A Membrane Channel. *Proc. Natl. Acad. Sci. U. S. A.* **1996**, *93*, 13770-13773.
(44) Kozak, D.; Anderson, W.; Vogel, R.; Chen, S.; Antaw, F.; Trau, M. Simultaneous Size and ζ-Potential Measurements of Individual Nanoparticles in Dispersion Using Size-Tunable Pore Sensors. *ACS Nano* **2012**, *6*, 6990-6997.
(45) Plesa, C.; Verschueren, D.; Pud, S.; van der Torre, J.; Ruitenberg, J. W.; Witteveen, M. J.; Jonsson, M. P.; Grosberg, A. Y.; Rabin, Y.; Dekker, C. Direct Observation Of DNA Knots Using A Solid-State Nanopore. *Nat. Nanotechnol.* **2016**, *11*, 1093-1097.
(46) Wu, H.; Chen, Y.; Zhou, Q.; Wang, R.; Xia, B.; Ma, D.; Luo, K.; Liu, Q. Translocation of Rigid Rod-Shaped Virus through Various Solid-State Nanopores. *Anal. Chem.* **2016**, *88*, 2502-2510.
(47) Branton, D.; Deamer, D. W.; Marziali, A.; Bayley, H.; Benner, S. A.; Butler, T.; Di Ventra, M.; Garaj, S.; Hibbs, A.; Huang, X.; et al. The Potential And Challenges Of Nanopore Sequencing. *Nat. Biotechnol.* **2008**, *26*, 1146-1153.
(48) Kwon, S. J.; Bard, A. J. DNA Analysis by Application of Pt Nanoparticle Electrochemical Amplification with Single Label Response. *J. Am. Chem. Soc.* **2012**, *134*, 10777-10779.
(49) Dick, J. E.; Renault, C.; Bard, A. J. Observation of Single-Protein and DNA Macromolecule Collisions on Ultramicroelectrodes. *J. Am. Chem. Soc.* **2015**, *137*, 8376-8379.
(50) Castañeda, A. D.; Brenes, N. J.; Kondajji, A.; Crooks, R. M. Detection of microRNA by Electrocatalytic Amplification: A General Approach for Single-Particle Biosensing. *J. Am. Chem. Soc.* **2017**, *139*, 7657-7664.
(51) Quinn, B. M.; van't Hof, P. G.; Lemay, S. G. Time-Resolved Electrochemical Detection Of Discrete Adsorption Events. *J. Am. Chem. Soc.* **2004**, *126*, 8360-8361.
(52) Xiao, X.; Bard, A. J. Observing Single Nanoparticle Collisions at an Ultramicroelectrode by Electrocatalytic Amplification. *J. Am. Chem. Soc.* **2007**, *129*, 9610-9612.
(53) Sokolov, S. V.; Eloul, S.; Kätelhön, E.; Batchelor-McAuley, C.; Compton, R. G. Electrode–Particle Impacts: A Users Guide. *Phys. Chem. Chem. Phys.* **2017**, *19*, 28-43.

(54) Boika, A.; Thorgaard, S. N.; Bard, A. J. Monitoring the Electrophoretic Migration and Adsorption of Single Insulating Nanoparticles at Ultramicroelectrodes. *J. Phys. Chem. B* **2013**, *117*, 4371-4380.
(55) Rees, N. V.; Banks, C. E.; Compton, R. G. Ultrafast Chronoamperometry of Acoustically Agitated Solid Particulate Suspensions: Nonfaradaic and Faradaic Processes at a Polycrystalline Gold Electrode. *J. Phys. Chem. B* **2004**, *108*, 18391-18394.
(56) Xiao, X.; Fan, F.-R. F.; Zhou, J.; Bard, A. J. Current Transients in Single Nanoparticle Collision Events. *J. Am. Chem. Soc.* **2008**, *130*, 16669-16677.
(57) Zhou, Y.-G.; Rees, N. V.; Compton, R. G. The Electrochemical Detection and Characterization of Silver Nanoparticles in Aqueous Solution. *Angew. Chem., Int. Ed. Engl.* **2011**, *50*, 4219-4221.
(58) Stuart, E. J. E.; Tschulik, K.; Batchelor-McAuley, C.; Compton, R. G. Electrochemical Observation of Single Collision Events: Fullerene Nanoparticles. *ACS Nano* **2014**, *8* (8), 7648-7654.
(59) Cheng, W.; Zhou, X.-F.; Compton, R. G. Electrochemical Sizing of Organic Nanoparticles. *Angew. Chem., Int. Ed. Engl.* **2013**, *52*, 12980-12982.
(60) Poon, J.; Batchelor-McAuley, C.; Tschulik, K.; Compton, R. G. Single Graphene Nanoplatelets: Capacitance, Potential Of Zero Charge And Diffusion Coefficient. *Chem. Sci.* **2015**, *6*, 2869-2876.
(61) Banks, C. E.; Rees, N. V.; Compton, R. G. Sonoelectrochemistry Understood via Nanosecond Voltammetry: Sono-emulsions and the Measurement of the Potential of Zero Charge of a Solid Electrode. *J. Phys. Chem. B* **2002**, *106*, 5810-5813.

Self-induced convection at microelectrodes via electroosmosis and its influence on impact electrochemistry

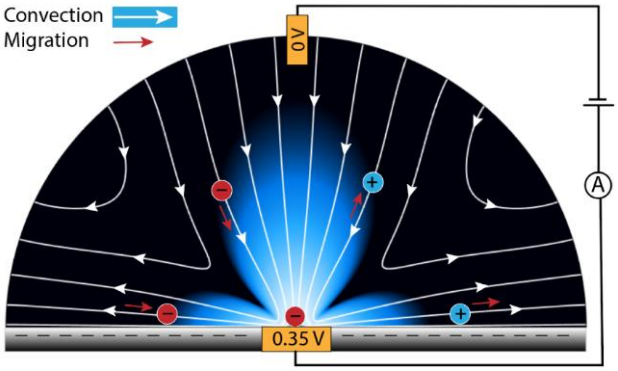

Faradaic reactions at low supporting electrolyte concentrations induce convection via electroosmotic flows. Here we combine finite-element simulations and electrochemical measurements on microparticles at ultramicroelectrodes to explore this effect. We show that convection becomes the dominant form of mass transport for experiments at low salt concentrations, violating the common assumption that convection can be neglected.

The contents of this chapter are published as: Moazzenzade, T.; Yang, X.; Walterbos, L.; Huskens, J.; Renault, C.; Lemay, S. G. Self-Induced Convection at Microelectrodes via Electroosmosis and Its Influence on Impact Electrochemistry. *J. Am. Chem. Soc.* **2020**, *142*, 17908-17912. The movies are freely available at: https://doi.org/10.1021/jacs.0c08450. Finite element simulations were performed by L. Walterbos.

Electrochemical processes and associated mass transport play a role in a plethora of physical phenomena and applications. While mass transport can often be understood in terms of diffusion alone,[1] migration and the corresponding ohmic potential drops also become increasingly relevant at low supporting electrolyte ratios.[2-7] Convection can also be imposed, for example in flow cells or at rotating disk electrodes. Moreover, natural convection has been shown to occur in temperature or concentration gradients and when caused by electrochemically generated bubbles.[8]

Far less recognized, however, is that electrochemical reactions can also induce convection through the generation of electroosmotic flows (EOFs). In this phenomenon, the electrochemically generated electric field drives the migration of mobile ions in the electrical double layer (EDL) of surfaces in contact with the solution, which in turn causes advection of the solvent. Electroosmosis has been intentionally employed in electrochemistry, for example for self-propulsion of microscale swimmers,[9] microscale pumping,[10,11] enhancing mass transport in nanoband electrodes[12] and directing the motion of bacteria.[13] The effect is however general and in principle occurs to some degree in most electrochemical processes. The insulating materials found in electrochemical cells consequently play an active role in determining the electrochemical response.

Here we illustrate this behavior experimentally by tracking the motion of microparticles in the vicinity of an ultramicroelectrode (UME) and relating these observations to amperometric signals caused by the oxidation of a redox mediator.[14] While it is well understood that the frequency of current blockade events increases with decreasing salt concentration,[14-16] EOFs cause the nature of the amperometric signals to change when the supporting electrolyte ratio (γ, defined as the monovalent salt concentration divided by the redox meditator concentration) becomes lower than unity. Convection in fact often dominates particle transport at low ionic strengths.

Miniaturized electrodes such as UMEs are particularly well suited to low-salt conditions because their solution resistance is largely determined by the region near the electrode.[3] When $\gamma < 1$, the ionic strength in this region increases, leading to decreased solution resistance.[3] However, UMEs are usually shrouded by an insulating surface such as glass which is normally charged in solution. This charge can interact with the induced electric field to cause EOFs and thus locally induce convection.

To gain quantitative understanding of this effect, we performed finite-element calculations of mass transport including self-generated electric fields and convection. In short, the species were a redox mediator in the reduced form (neutral, $z = 0$), its oxidized counterpart ($z = +1$), and a supporting electrolyte represented by a cation ($z = +1$) and an anion ($z = -1$). Transport was described by the Nernst-Planck equation. Charge neutrality was imposed and, consequently, surface charges and the corresponding EDLs were not explicitly included in the equations. It was assumed that the mediator was instantly converted to the oxidized form at the electrode (high overpotential conditions[2]). The solution was further described as an incompressible Newtonian fluid. To describe EOFs, the velocity of the fluid at the glass

surface, $u_{\|}$, was given by the Helmholtz–Smoluchowski equation, $u_{\|} = (\varepsilon\zeta_s/\mu)E_{\|}$.[17] Here ε and μ are the permitivity and the viscosity of the solution, respectively, ζ_s is the ζ-potential of the surface, and $E_{\|}$ is the tangential electric field. The microparticle trajectories were computed from force balance between electrophoretic and viscous drag forces (see Supporting Information for a complete description).

The self-consistent results are summarized in Figure 3.1. Oxidation of the mediator at the electrode causes local injection of positive charge into the solution and gives rise to an electric field (Figure 3.1a). An EOF is thus created that advects fluid along the negatively charged surface shrouding the electrode. To compensate this flow, fluid is drawn toward the electrode from above (Figure 3.1b). Negatively charged microparticles move both by migration and convection in this environment, resulting in trajectories that reflect both modes of transport (Figures 3.1c and 3.1d).

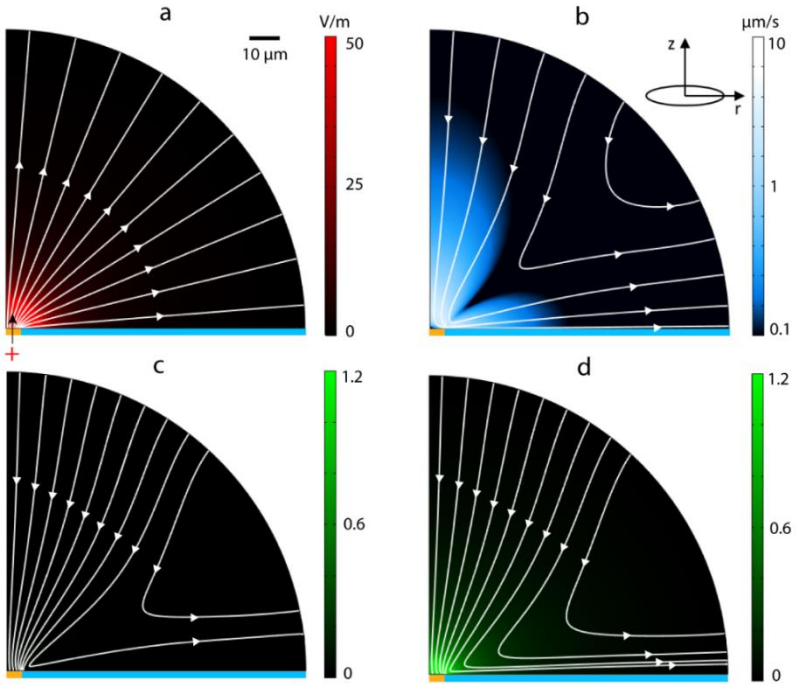

Figure 3.1. Calculated mass transport properties. (a) Electric field lines (white) and magnitude (color scale) upon oxidation at the electrode. This field causes a 1.6 mV ohmic potential drop at the electrode surface. (b) Fluid streamlines (white) and flow speed (color scale). (c) Particle trajectories (white lines) and excess anion concentration (color scale, expressed as a ratio of the bulk salt concentration). Panels (a-c) correspond to 0.67 mM mediator concentration and 5 mM salt concentration ($\gamma = 7.5$). (d) Same as (c) for 0.15 mM salt ($\gamma = 0.22$).

The role of convection is clearly visible in Figures 3.1c and 3.1d, which shows that trajectories approaching the edge of the electrode are deflected to the side. This occurs because the velocity of a particle near the surface, $u_{p,\parallel}$, is the sum of electrophoretic and convective components,

$$u_{p,\parallel} = \frac{\varepsilon E_\parallel}{\mu}(\zeta_p - \zeta_s) \qquad (1)$$

where ζ_p is the ζ-potential of the particle. When ζ_s is more negative than ζ_p, convection dominates and particles escape along the surface.

The trajectories depend sensitively on the salt concentration. When $\gamma \gg 1$, the shape of the pathways is essentially independent of the ionic strength. When $\gamma \ll 1$, on the other hand, the concentrations of oxidized mediator and its counterion exceeds the bulk salt concentration near the electrode (Figure 3.1d). This local enrichment diminishes the electrophoretic force acting on the colloidal particles compared to that which would be encountered otherwise. The EOF is also locally diminished, but this effect is less pronounced because the local fluid velocity also depends on the EOF far from the electrode due to fluid incompressibility. Convection thus dominates over migration at low γ and more particles evade the electrode.

To experimentally challenge these predictions, we first performed experiments using d = 1 µm diameter negatively charged polystyrene particles (ζ-potential = –30 mV) and positively charged amidine-coated latex beads (ζ-potential = +32 mV). A 10 µm diameter glass-encased Pt UME was inserted in a cell allowing optical access. The glass surrounding the UME had a negative ζ-potential (≈ –55 mV at pH 5).[18] As redox mediator and supporting electrolyte we employed 0.67 mM 1,1′-ferrocenedimethanol and various concentrations of KCl, respectively. In cases where we specify 'no added salt', the conductivity of the solution was 2 µS/cm, which corresponds to an ionic strength of ≈30 μM.[19] Unless indicated otherwise, a constant potential of +0.35 V was applied to the UME with respect to a Pt pseudo-reference electrode, corresponding to a highly oxidizing overpotential (cyclic voltammogram in Figure 3.S5). The current was monitored while simultaneously imaging the motion of the particles. Additional details on Materials and Methods are given in the Supporting Information.

Figure 3.2 shows typical amperometric responses (traces at other salt concentrations are shown in Figures 3.S2 and 3.S3). At high salt concentration (5 mM KCl, Figure 3.2a), we observed conventional current blockade: single particles were drawn by electrophoresis and adsorbed to the electrode surface, interfering with transport of the redox mediator and leading to discrete steps in the current (some steps also result from rearrangement of particles[15]). At a lower salt concentration (0.15 mM, Figure 3.2b), however, the response became more complex. A new type of dip-like event appeared in which the current temporarily decreased before returning to its initial value. This suggests that some particles approached the surface of the electrode but then, counter-intuitively, left again.[13,14,20,21] Finally, positively charged particles (Figure 3.2c) exhibited no steps but did show frequent dips. Steps would be

unexpected in this case since these particles migrate away from the electrode. The occurrence of dips indicates that the particles are transiently drawn to the electrode by a mechanism other than migration.

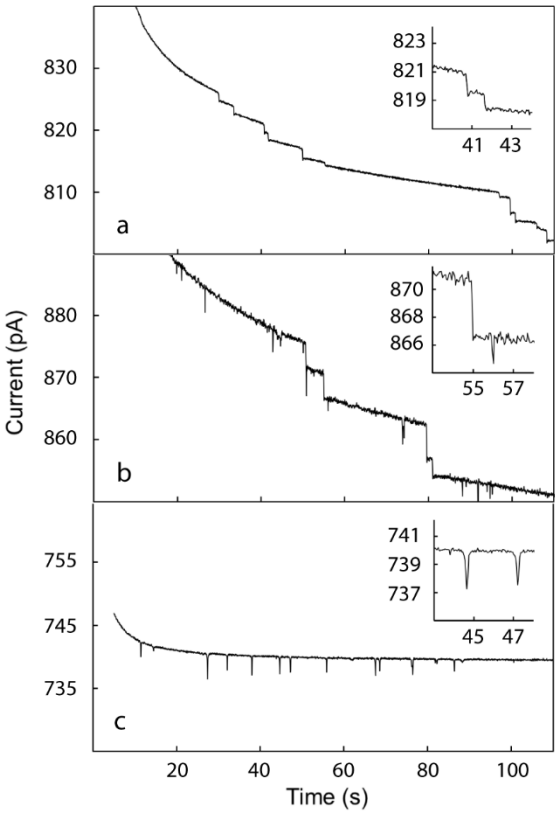

Figure 3.2. Current-time response for impact of negatively charged particles at high (5 mM, (a)) and low (0.15 mM, (b)) salt concentrations. While the response at high salt consists almost uniquely of step-wise decreases, dip-like features also occur at low salt. (c) Positively charged particles exhibit only dips ($\gamma = 2$).

The origin of this bimodal behavior is readily elucidated by optically monitoring the particles (Supporting Information). Figure 3.3 shows snapshots of the trajectories of two particles at low salt concentration. The first (blue arrow) adsorbed on the surface of the electrode, corresponding to a stepwise current decrease. The second particle (red arrow) instead approached the electrode from above before being deflected along the surface of the glass. This behavior caused a dip-like transient amperometric response when the particle passed near the surface of the electrode (see Supporting Movie 1 for complete sequence). Positively charged particles also exhibit similar trajectories (Movie 2). In each case, particles moving

away from the electrode stay close to the glass surface, matching the behavior shown in Figure 3.1d.

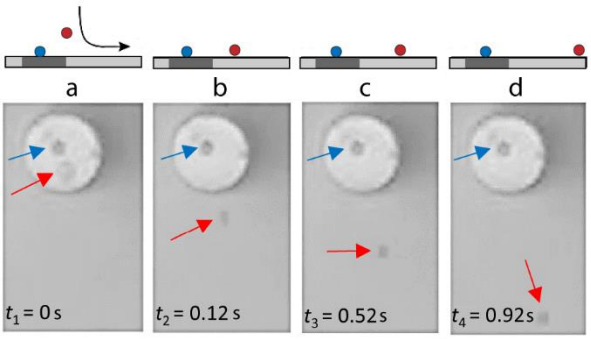

Figure 3.3. Trajectory for negatively charged particles. In (a), one microparticle is adsorbed to the electrode surface (blue arrow) while a second is out of focus in solution above the electrode (red arrow). The latter then approaches the surface and is deflected sideways (b-d). The diagrams above each image illustrate the different steps of this process. The UME diameter was 10 μm.

Figure 3.4 (orange curve) shows the radial distance from the center of the electrode versus time for a typical trajectory. The slope of this curves, which represents radial velocity, decreases as time progresses. This behavior is easily understood by noting that the magnitude of the electric field decreases as r^{-2}.[3,16] Combined with eq 1, this leads to the prediction that the position along the surface obeys the form $r(t) \propto t^{1/3}$ (Supporting Information). Fits to this expression (solid lines in Figure 3.4) agree with the experimental data very well, showing that the particles move with a velocity $u_{p,\parallel} \approx$ 50-100 μm/s in the vicinity of the electrode. This corresponds to a Peclet number Pe = $u_{p,\parallel} d/D \approx 10^3$, where D is the diffusion coefficient of the particles, indicating that migration and convection dominate over diffusion in mass transport.

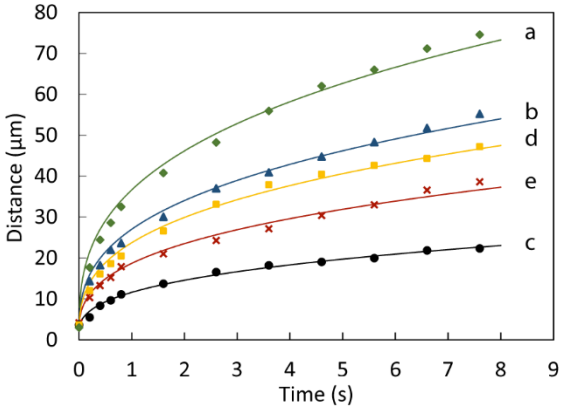

Figure 3.4. Distance-time curve for different particle charge, salt concentrations and applied potentials. (a)-(c): positively charged particles with no added salt, 0.15 mM, and 1.34 mM salt concentrations, respectively (applied potential: 0.35 V). (d) Negatively charged particle at 0.15 mM salt (0.35 V). (e) Positively charged particle with no added salt (0.05 V). The solid lines are fits to distance $\propto (t - t_0)^{1/3}$.

Eq 1 makes several testable predictions. First, positively charged particles ($\zeta_p > 0$) should move faster near the surface since migration and EOF work in concert. This is indeed observed experimentally (Figure 3.4, blue *vs* orange curve). Second, diminishing the strength of the electric field should lead to slower motion. The induced electric field is proportional to the magnitude of the faradaic current, which can be controlled via the applied electrode potential. We changed the electrode bias to +0.05 V and, as a result, the particles slowed down by a factor ~2 (Figure 3.4, red curve; Movie 3). We also changed the salt concentration, which resulted in higher particle velocities at lower salt (Figure 3.4, black, blue, and green curves; Movie 4 corresponds to the black curve). Third, making the surface potential ζ_s less negative or positive should diminish or even reverse the EOF.[22] Measurements with a UME coated with the cationic polymer Poly-L-lysine exhibited once again step-like responses and the particles trajectories reversed direction, suggesting EOF suppression or reversal ($\zeta_p - \zeta_s < 0$ in eq 1; Figure 3.S4, Movie 5).

Our results demonstrate that faradaic reactions induce convection in the fluid surrounding an electrode due to EOFs. This applies to both UMEs and electrodes imbedded in microsystems. It was previously inferred that convection influences measurements with UMEs at low salt concentrations.[23] Our measurements fully support this conclusion and identify the intrinsic mechanism responsible for convection. Transport of the redox mediator is also affected, although the effect is less dramatic due to the relative importance of diffusion for small molecules (Pe ≈ 1).[16] Cyclic voltammetry indeed shows an increase of order 10% of the mediator mass-transport-limited current at low salt concentration (Figures 3.S5 and 3.S6).

This is *a priori* surprising given that this molecule is electrically neutral and illustrates the generality of the EOF effect.

In addition, our results are relevant for the interpretation of impact electrochemistry measurements, which are often conducted under low salt conditions to increase the event frequency. EOFs generated by a mediator (for current blockade impact), electrocatalytic particles[24,25] (for catalytic impact measurements) or even parasitic background reactions (for all impact methods) affect the rate and shape of events under these conditions, which must be taken into account for quantitative applications in single-entity electrochemistry. For example, our observations explain the previously reported saturation of the collision rate for $\gamma < 1$.[26]

On the other hand, a drawback of most impact methods is that electrodes become saturated over the course of an experiment, complicating interpretation and limiting measurement times. Inverting the charge of the particles instead leads to current dips without adsorption to the electrode surface, enabling extended measurements. The same could be achieved with negatively charged particles by using a reduction reaction for the mediator instead of an oxidation, thus reversing the polarity of the induced electric field.

3.1 Supporting information

3.1.1 Derivation of the $t^{1/3}$ dependence

The electric field around a hemispherical electrode has the form[26]

$$E_{\parallel}(r) = -\frac{dV}{dr} = \frac{1}{fr}\left(1 + \frac{2D_{\mathrm{Ox}}c_{\mathrm{salt}}r}{D_{\mathrm{Red}}c^{0}_{\mathrm{Red}}a}\right)^{-1}$$

Far from the electrode this reduces to

$$E_{\parallel}(r) = \frac{D_{\mathrm{Red}}c^{0}_{\mathrm{Red}}a}{2fD_{\mathrm{Ox}}c_{\mathrm{salt}}r^{2}}$$

While our electrode is disc-shaped rather than hemispherical, far from the electrode we expect this expression to hold to a good approximation (apart from a numerical pre-factor of order unity). Combining this result with eq 1 from the main text yields a differential equation for the radial position of a particle traveling along the surface, r, as a function of time:

$$\frac{dr}{dt} = u_{p,\parallel} = \left[\frac{\varepsilon D_{\mathrm{Red}}c^{0}_{\mathrm{Red}}a}{2f\mu D_{\mathrm{Ox}}c_{\mathrm{salt}}}(\zeta_p - \zeta_s)\right]\frac{1}{r^{2}}$$

Taking $r(0) = 0$ as initial value yields the solution

$$r(t) = \left[\frac{3\varepsilon D_{\mathrm{Red}} c^0_{\mathrm{Red}} a}{2f\mu D_{\mathrm{Ox}} c_{\mathrm{salt}}}(\zeta_p - \zeta_s)\right]^{1/3} t^{1/3}$$

The numerical pre-factor has a value of ≈38 μm/s$^{1/3}$ for the 5 mM salt case, in semiquantitative agreement with typical trajectories.

For the purpose of plotting the data of Figure 3.4, $t = 0$ was defined as the moment where the particle reached the edge of the electrode on its outward trajectory. This introduced a small time shift t_0 compared to the definition in the calculation above. The data of Figure 3.4 were therefore fitted to the form
$r(t) \propto (t - t_0)^{1/3}$.

3.1.2 Materials and methods

All the measurements were performed using 1 μm diameter particles. For the negatively charged analyte, polystyrene particles (micromod Partikeltechnologie GmbH, custom streptavidin-coated polystyrene) with ζ-potential = –30 mV and a density of 4.7 × 10^{10} particles/ml were used. As received, the stock solution contained PBS buffer (pH = 7.4). The particle solution was diluted 1000 times in 0.67 mM ferrocenedimethanol (prepared in MilliQ water) as the working solution for the measurements. For positively charged particles, 1 μm diameter amidine latex beads (Invitrogen™ , A37322, medium: de-ionized water, ζ-potential = +32 mV, density 8.5 × 10^{10} particles/ml, 1000 times diluted) were used. PBS was added to the working solution of positively charged particles to match the negatively charged particle electrolyte composition in the 'no added salt' case. In cases where we specify 'no added salt', the conductivity of the solution was 2 μS/cm, which corresponds to an ionic strength of ≈30 μM.[19] As redox mediator we employed 0.67 mM 1,1′-ferrocenedimethanol (Sigma-Aldrich, 372625). We employed KCl (Sigma-Aldrich, P9333) as supporting electrolyte with concentrations as indicated in the text.

Poly-L-lysine hydrobromide (Sigma-Aldrich, P7980) was used for surface functionalization. The UME was polished mechanically with alumina particles and then treated with oxygen plasma (Diener electronic) for 15 min. The cleaned UME was incubated in PLL solution (0.1-1μg/ml in PBS buffer) on a magnet stirrer for 10 min. PLL adheres to both the glass and the Pt of the UME. To insure that PLL did not significantly hinder the oxidation of the redox mediator, the incubation time was optimized to recover typical mass-transport-limited currents at the PLL-functionalized UME (Figure 3.S4).

The experimental geometry is illustrated in Figure 3.S1. A 10 μm diameter glass-encased Pt UME (BASi/MF-2005) was inserted in a polydimethylsiloxane (PDMS) cylinder which was then capped with a glass coverslip, allowing optical access. The thickness of the liquid layer under the coverslip was 100-200 μm. A Pt wire loop surrounding the tip of the UME (wire

diameter 0.20 mm, ≈ 11 mm length exposed to solution) served as counter and pseudo-reference electrode. This circular electrode was used to provide cylindrical symmetry. Placing the reference electrode on only one side of the working electrode instead led to the majority of particles arriving from that direction. Unless indicated otherwise, a constant potential of +0.35 V was applied to the UME with respect to the pseudo-reference electrode, corresponding to a highly oxidizing overpotential (cyclic voltammogram in Figure 3.S5), and the current was monitored using a transimpedance amplifier (Femto, DDPCA-300). A microscope (Zeiss/Axio Scope Vario) with a LD EC "Epiplan-Neofluar" 50x/0.55 DIC M27 objective (parfocal lengh = 45 mm, free working distance = 9.1 mm) was used for optical microscopy, recording the motion of the particles in two dimensions simultaneously with the amperometric measurement. Three-dimensional tracking has also been demonstrated, but this was not attempted here due to our broad illumination spectrum.[27-31]

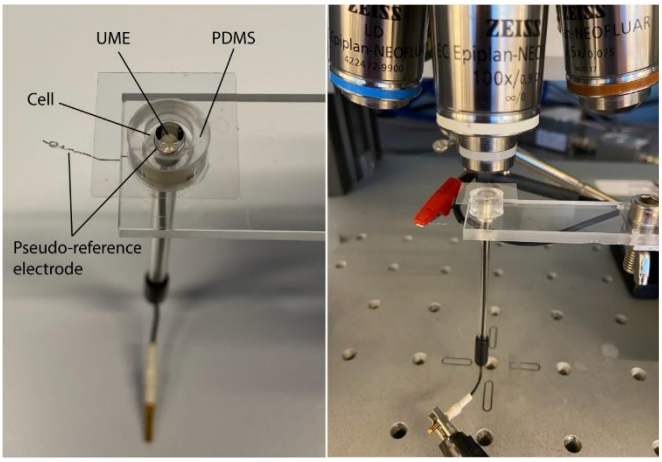

Figure 3.S1. Measurement setup. Left: assembled two-electrode cell. Right: Cell positioned under the microscope for simultaneous optical imaging.

3.1.3 Additional amperometric data

Figures 3.S2 and 3.S3 show typical amperometric traces for positively and negatively charged particles, respectively, for different supporting electrolyte ratios.

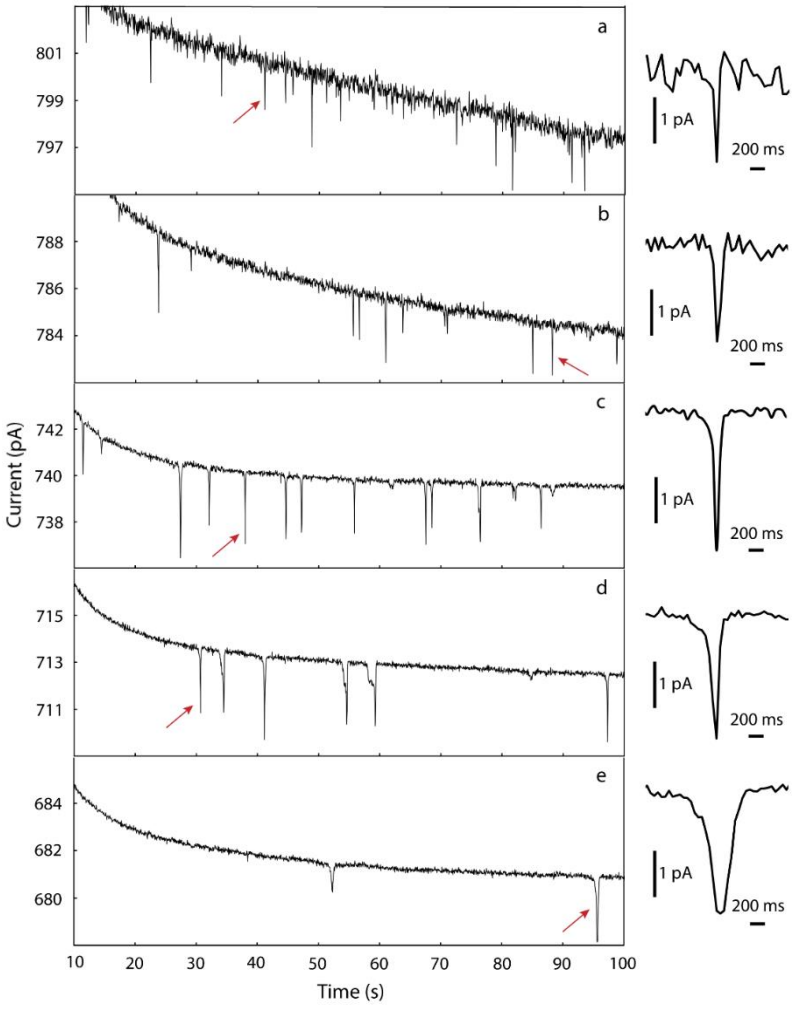

Figure 3.S2. Current time responses for impact of positively charged particles at different salt concentrations. a: $\gamma \ll 1$, b: $\gamma = 1$, c: $\gamma = 2$, d: $\gamma = 4$, and e: $\gamma = 8$. The pulse duration increases with increasing salt concentration, reflecting the decreased convection and migration speeds at higher γ values.

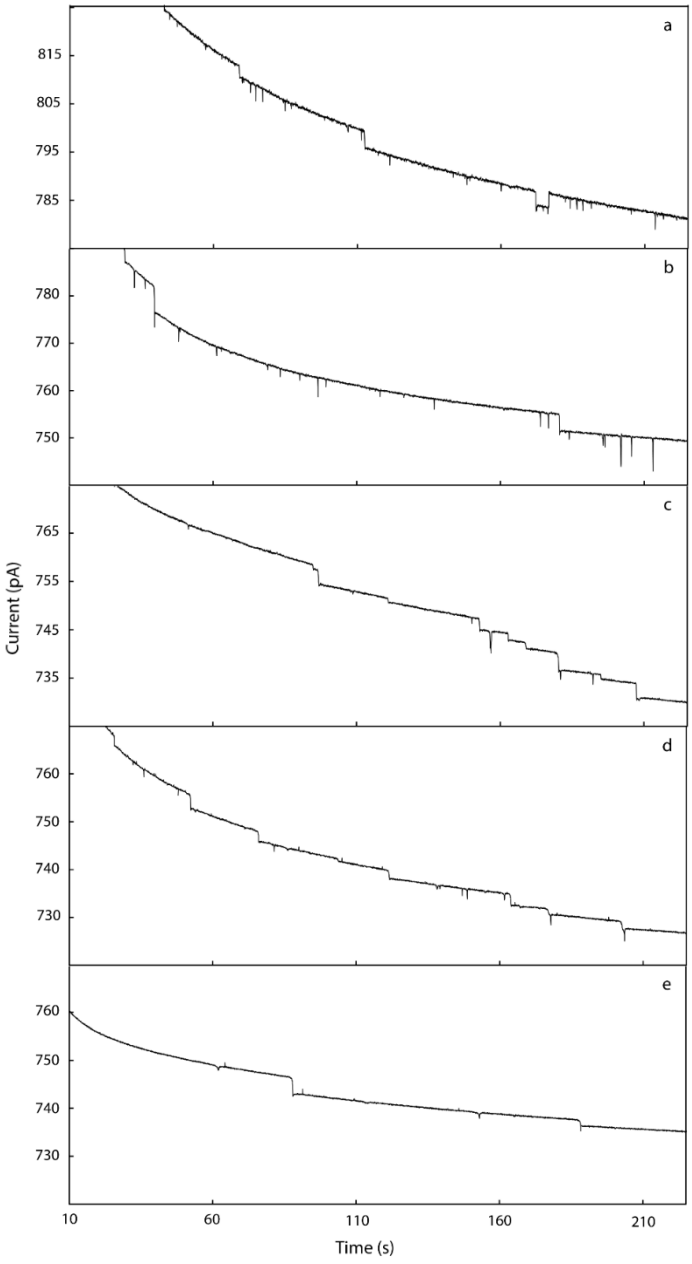

Figure 3.S3. Current time responses for impact of negatively charged particles at different salt concentrations. a: $\gamma \ll 1$ (no added salt), b: $\gamma = 1$, c: $\gamma = 2$, d: $\gamma = 4$, and e: $\gamma = 8$.

3.1.4 Amperometric response and distance-time curve for PLL-coated UME

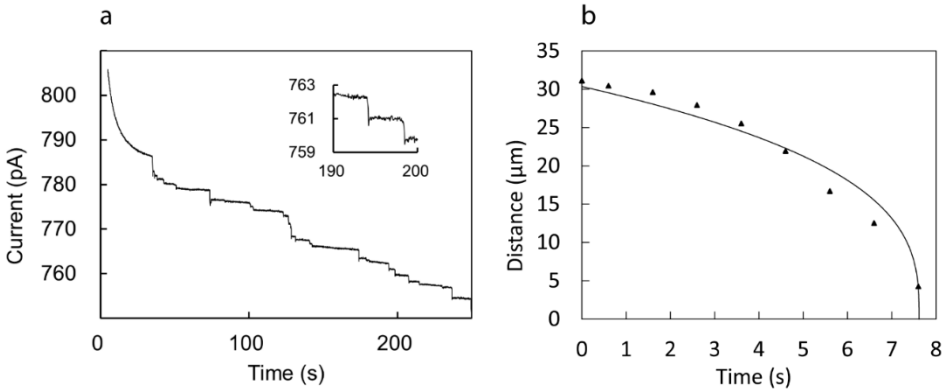

Figure 3.S4. (a) Current-time response and (b) distance-time curve for impact of 1 µm diameter negatively charged polystyrene particles at a PLL-coated UME and 0.15 mM KCl (Movie 5).

3.1.5 Mass-transport-limited current versus supporting electrolyte ratio

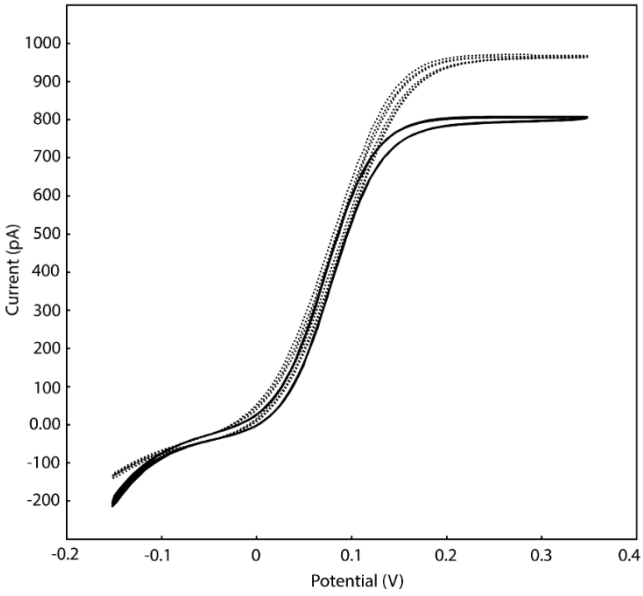

Figure 3.S5. Cyclic voltammograms of 0.67 mM Fc-dimethanol at high and low salt concentrations using 10 µm diameter UME and Pt pseudo-reference electrode. The continuous and dotted curves correspond to $\gamma = 8$ and $\gamma = 0.0625$, respectively.

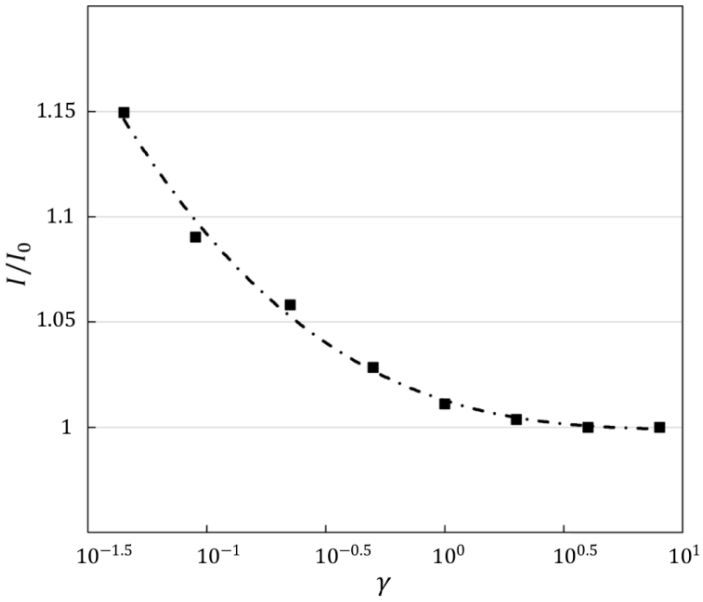

Figure 3.S6. Mass-transport-limited current *vs* supporting electrolyte ratio γ. The values were extracted from cyclic voltammograms under the same conditions as Figure 3.S5 and were normalized to the limiting current observed at high γ. The enhancement of the current at low supporting electrolyte ratio is caused solely by convection (as opposed to migration, since the redox species is electrically neutral).

3.2 References

(1) Bard, A. J.; Faulkner, L. R. *Electrochemical Methods: Fundamentals and Applications, 2nd ed*; John Wiley & Sons: New York, 2000; 137-157.
(2) Amatore, C.; Deakin, M. R.; Wightman, R. M. Electrochemical Kinetics At Microelectrodes: Part Iv. Electrochemistry In Media Of Low Ionic Strength. *J. electroanal. chem. interfacial electrochem.* **1987**, *225*, 49-63.
(3) Oldham, K. B. Theory Of Microelectrode Voltammetry With Little Electrolyte. *J. Electroanal. Chem. Interfacial Electrochem.* **1988**, *250*, 1-21.
(4) Drew, S. M.; Wightman, R. M.; Amatore, C. A. Voltammetry Of Ferrocene In Low Electrolyte Solutions. *J. Electroanal. Chem. Interfacial Electrochem.* **1991**, *317*, 117-124.
(5) Bond, A. M.; Lay, P. A. Cyclic Voltammetry At Microelectrodes In The Absence Of Added Electrolyte Using A Platinum Quasi-Reference Electrode. *J. Electroanal. Chem. Interfacial Electrochem.* **1986**, *199*, 285-295.
(6) Howell, J. O.; Wightman, R. M. Ultrafast Voltammetry And Voltammetry In Highly Resistive Solutions With Microvoltammetric Electrodes. *Anal. Chem.* **1984**, *56*, 524-529.
(7) Amatore, C.; Knobloch, K.; Thouin, L. First Direct Experimental Evidence Of Migration Contributions Through Monitoring Of Concentration Profiles At Low Supporting Electrolyte Concentration. *Electrochem. Commun.* **2004**, *6*, 887-891.

(8) Novev, J. K.; Compton, R. G. Natural Convection Effects In Electrochemical Systems. *Curr. Opin. Electrochem.* **2018**, *7*, 118-129.
(9) Paxton, W. F.; Kistler, K. C.; Olmeda, C. C.; Sen, A.; St. Angelo, S. K.; Cao, Y.; Mallouk, T. E.; Lammert, P. E.; Crespi, V. H. Catalytic Nanomotors: Autonomous Movement of Striped Nanorods. *J. Am. Chem. Soc.* **2004**, *126*, 13424-13431.
(10) Kline, T. R.; Paxton, W. F.; Wang, Y.; Velegol, D.; Mallouk, T. E.; Sen, A. Catalytic Micropumps: Microscopic Convective Fluid Flow and Pattern Formation. *J. Am. Chem. Soc.* **2005**, *127*, 17150-17151.
(11) Kostiuchenko, Z. A.; Glazer, P. J.; Mendes, E.; Lemay, S. G. Chemical Physics Of Electroactive Materials – The Oft-Overlooked Faces Of Electrochemistry. *Faraday Discuss.* **2017**, *199*, 9-28.
(12) Branagan, S. P.; Contento, N. M.; Bohn, P. W. Enhanced Mass Transport of Electroactive Species to Annular Nanoband Electrodes Embedded in Nanocapillary Array Membranes. *J. Am. Chem. Soc.* **2012**, *134*, 8617-8624.
(13) Thorgaard, S. N.; Jenkins, S.; Tarach, A. R. Influence of Electroosmotic Flow on Stochastic Collisions at Ultramicroelectrodes. *Anal. Chem.* **2020**, *92*, 12663-12669.
(14) Quinn, B. M.; van't Hof, P. G.; Lemay, S. G. Time-Resolved Electrochemical Detection Of Discrete Adsorption Events. *J. Am. Chem. Soc.* **2004**, *126*, 8360-8361.
(15) Boika, A.; Thorgaard, S. N.; Bard, A. J. Monitoring the Electrophoretic Migration and Adsorption of Single Insulating Nanoparticles at Ultramicroelectrodes. *J. Phys. Chem. B* **2013**, *117*, 4371-4380.
(16) Moazzenzade, T.; Huskens, J.; Lemay, S. G. Stochastic Electrochemistry at Ultralow Concentrations: the Case for Digital Sensors *Analyst* **2020**, *145*, 750-758.
(17) Probstein, R. F. In *Physicochemical Hydrodynamics: An Introduction*, 2nd ed.; John Wiley & Sons, 1994; pp 165-210.
(18) Gu, Y.; Li, D. The ζ-Potential of Glass Surface in Contact with Aqueous Solutions. *J. Colloid Interface Sci.* **2000**, *226*, 328-339.
(19) Marion, G. M.; Babcock, K. L. Predicting Specific Conductance and Salt Concentration in Dilute Aqueous Solutions. *Soil Sci.* **1976**, *122*, 181-187.
(20) Ronspees, A. T.; Thorgaard, S. N. Blocking Electrochemical Collisions Of Single E. coli And B. subtilis Bacteria At Ultramicroelectrodes Elucidated Using Simultaneous Fluorescence Microscopy. *Electrochim. Acta.* **2018**, *278*, 412-420.
(21) Yoo, J. J.; Anderson, M. J.; Alligrant, T. M.; Crooks, R. M. Electrochemical Detection of Insulating Beads at Subattomolar Concentration via Magnetic Enrichment in a Microfluidic Device. *Anal. Chem.* **2014**, *86*, 4302-4307.
(22) Subramanian, S.; Catchmark, J. M. Control of Catalytically Generated Electroosmotic Fluid Flow through Surface Zeta Potential Engineering. *J. Phys. Chem. C* **2007**, *111*, 11959-11964.
(23) Bento, M. F.; Thouin, L.; Amatore, C. Potential Measurements in Steady State Voltammetry at Low Electrolyte/Analyte Concentration Ratios. Role of Convection on Ohmic Drop: A Simplified Model. *J. Electroanal. Chem.* **1998**, *446*, 91-105.
(24) Xiao, X.; Bard, A. J. Observing Single Nanoparticle Collisions at an Ultramicroelectrode by Electrocatalytic Amplification. *J. Am. Chem. Soc.* **2007**, *129*, 9610-9612.
(25) Xiao, X.; Fan, F.-R. F.; Zhou, J.; Bard, A. J. Current Transients in Single Nanoparticle Collision Events. *J. Am. Chem. Soc.* **2008**, *130*, 16669-16677.
(26) Renault, C.; Lemay, S. G. Electrochemical Collisions of Individual Graphene Oxide Sheets: An Analytical and Fundamental Study. *ChemElectroChem* **2020**, *7*, 69-73.

(27) Batchelor-McAuley, C.; Martinez-Marrades, A.; Tschulik, K.; Patel, A. N.; Combellas, C.; Kanoufi, F.; Tessier, G.; Compton, R. G. Simultaneous Electrochemical and 3d Optical Imaging of Silver Nanoparticle Oxidation. *Chem. Phys. Lett.* **2014**, *597*, 20-25.
(28) Patel, A. N.; Martinez-Marrades, A.; Brasiliense, V.; Koshelev, D.; Besbes, M.; Kuszelewicz, R.; Combellas, C.; Tessier, G.; Kanoufi, F. Deciphering the Elementary Steps of Transport-Reaction Processes at Individual Ag Nanoparticles by 3D Superlocalization Microscopy. *Nano Lett.* **2015**, *15*, 6454-6463.
(29) Yu, Y.; Sundaresan, V.; Bandyopadhyay, S.; Zhang, Y.; Edwards, M. A.; McKelvey, K.; White, H. S.; Willets, K. A. Three-Dimensional Super-resolution Imaging of Single Nanoparticles Delivered by Pipettes. *ACS Nano* **2017**, *11*, 10529-10538.
(30) Sundaresan, V.; Marchuk, K.; Yu, Y.; Titus, E. J.; Wilson, A. J.; Armstrong, C. M.; Zhang, B.; Willets, K. A. Visualizing and Calculating Tip–Substrate Distance in Nanoscale Scanning Electrochemical Microscopy Using 3-Dimensional Super-Resolution Optical Imaging. *Anal. Chem.* **2017**, *89*, 922-928.
(31) Joshi, P. B.; Anthony, T. P.; Wilson, A. J.; Willets, K. A. Imaging Out-of-Plane Polarized Emission Patterns on Gap Mode Sers Substrates: from High Molecular Coverage to the Single Molecule Regime. *Faraday Discuss.* **2017**, *205*, 245-259.

Ring ultramicroelectrodes for current-blockade particle-impact electrochemistry

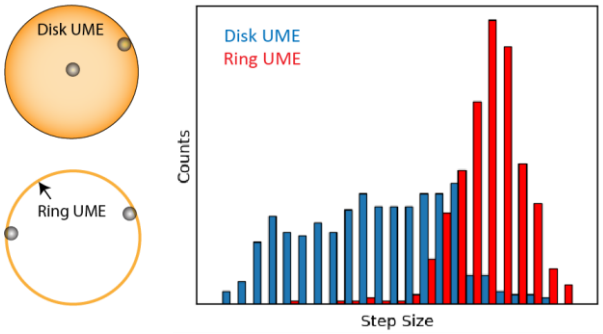

In current-blockade impact electrochemistry, insulating particles are detected amperometrically as they impinge upon a micro- or nanoelectrode via a decrease in the faradaic current caused by a redox mediator. A limit of the method is that analytes of a given size yield a broad distribution of response amplitudes due to the inhomogeneities of the mediator flux at the electrode surface. Here we overcome this limitation by introducing microfabricated ring-shaped electrodes with a width that is significantly smaller than the size of the target particles. We show that the relative step size is somewhat larger and exhibits a narrower distribution than at a conventional ultramicroelectrode of equal diameter.

The contents of this chapter are published as: Moazzenzade, T.; Walstra, T.; Yang, X.; Huskens, J.; Lemay, S. G. Ring Ultramicroelectrodes for Current-Blockade Particle-Impact Electrochemistry. *Anal. Chem.* **2022**, *94*, 10168-10174.

4.1 Introduction

Particle-impact electrochemistry is a set of techniques in which individual micro- and nanoscale entities are detected in real time as they impinge upon a miniaturized electrode. Depending on the electroactivity of the particles and of the electrode, particle collisions lead to various types of stochastic, discrete signatures in amperometric measurements. Information on the particles such as surface properties, catalytic activity, size and even shape can be inferred from these measurements,[1-12] also in optically opaque solutions.[13] Impact methods have also been used for detecting individual biomolecules[14-18] and have been suggested as candidate single-entity electrochemical transducers for digital biosensing.[19]

An early variant of particle impact electrochemistry is current blockade. Here insulating particles are detected as a decrease in an otherwise steady-state amperometric signal as they interfere with the mass transport of a redox mediator to the electrode.[20] In addition to inert synthetic particles, this method has been employed to detect bacteria,[21] vesicles,[22] viruses,[17] and biomolecules.[15] It has further been employed as a tool for characterizing the size of biomacromolecules[15] and graphene oxide sheets.[23] A limitation of the method however arises because the size of the steps in the measured current depends on the location of the particle on the electrode.[24,25] This occurs because the mediator flux is not uniform over the surface of a planar electrode, as illustrated in Figure 4.1a. For a disk ultramicroelectrode (UME), for example, the current density is highest near the rim of the electrode and smallest at its center.[26] This inhomogeneity causes two main problems in particle blockade measurements with disk-shaped UMEs: (1) false-positive events introduce error in particle-counting experiments[24,25] and (2) biases are introduced in particle-sizing experiments that are based on the amplitude of the current blockade steps.[24,25]

False-positive detection events are the first consequence of the inhomogeneous flux of redox mediators on disk UMEs. In most blockade impact experiments, migration is the dominant mode of transport for charged particles while the flux of the inert redox mediator remains diffusion-limited.[1] The disk edge exhibits a higher flux density and, consequently, a stronger residual electric field. Hence, charged particles tend to migrate toward the edge of the UME. Furthermore, as a result of this electrophoretic edge effect, particles that are adsorbed near the center of the electrode subsequently migrate toward the edge. This dynamic rearrangement of particles leads to unwanted steps that result in overestimates during particle counting measurements.[24,25]

The second issue is the uneven signal that is due to the mediator edge effect. Due to the non-uniform mediator flux, the location where particles land on the surface can cause uneven current step sizes, with particle collisions near the edge of the disk leading to bigger steps than near the center. This occurs independently of whether particles are transported primarily by migration or diffusion. This issue complicates signal analysis in blockade impact measurements, and in particular renders particle size measurements difficult. In blockade

impact, particle size (radius, $r_{\Delta i}$) can be estimated from the current step magnitude using $r_{\Delta i} = \alpha a \sqrt{\Delta i_{ss}/i_{ss}}$, where i_{ss} is the steady-state current, Δi_{ss} is the current step magnitude, a is the radius of the UME, and α is a numerical factor that depends on the electrode geometry.[15] This expression however neglects the variability in step size introduced by the mediator edge effect.[25] Uneven current steps can also indirectly affect particle counting measurements if collisions near the disk center lead to steps that are smaller than the background noise, while collisions at the edge cause measurable steps. This limits the usable electrode-to-particle size ratio.[27] Finally, a variable step size is particularly problematic if a particular step size Δi_{ss} is used as the signature of a specific event such as in biorecognition.[28]

Because the discrepancies in signal size and frequency both stem from the inhomogeneous flux of redox mediator, solving this issue can significantly improve the accuracy of blockade impact measurements. Recently, Renault et al. demonstrated a way to circumvent non-uniform flux by using a hemispherical electrode, for which the current density is uniform over the surface of the electrode.[29] This uniformity stems from the spherical symmetry of this geometry, at least under conditions where surface conduction and electrokinetic effects caused by the insulating shroud surrounding the electrode can be neglected. In this work the electrodes were realized using liquid Hg. While an important proof of concept, this system remains somewhat impractical for routine measurements due to the additional fluid handling and safety considerations attached to Hg.

Here we introduce an alternative electrode geometry to overcome the non-uniform flux of redox mediators in blockade impact electrochemistry. The electrodes, which are fabricated using optical lithography, consist of a ring that is thinner than the particles to be detected. The structure is analogous to ring electrodes in some ring-disk electrode pairs used for redox cycling and generator-collector experiments.[30,31] This approach avoids the problems caused by an inhomogeneous current density. Particles colliding at any position along the circumference of the ring encounter a similar environment. Furthermore, while the mediator flux does vary across the width of the ring, the larger size of the particles insures that the measured signal includes contributions from the entire distribution of fluxes (Figure 4.1b), largely eliminating positional effects. In a migration-limited regime, particles remain confined to the contour of the ring through the electric field and block a similar amount of redox molecules. Furthermore, this geometry is fully compatible with planar microfabrication methods, unlike a hemispherical geometry, while also allowing impact measurements at current densities higher than those encountered at disk UMEs of the same diameter. We show experimentally that ring electrodes exhibit a narrower distribution of step sizes and a higher relative size sensitivity when compared to data for disk electrodes of the same diameter.

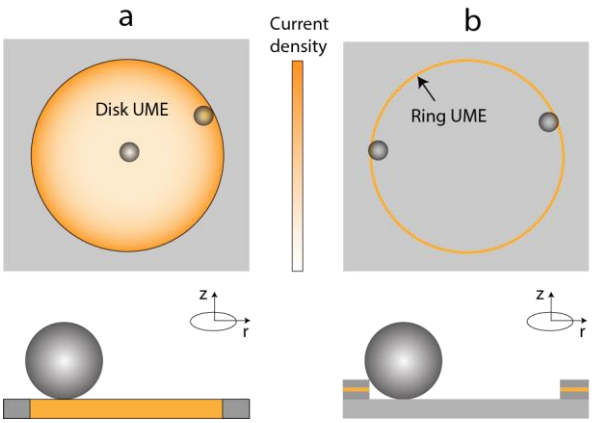

Figure 4.1. Schematic representation of disk and ring UMEs. (a) For the disk UME, the region near the rim of the disk has the highest mediator flux and correspondingly the highest current density. The current density (given by eq 3) is minimal at the center of the electrode, but with a large region surrounding the center where it is nearly constant. Because of the variations in current density, particles landing near the center or the edge of the disk lead to different signal sizes. (b) For the ring UME, the mediator flux and the current density are uniform along the circumference. Variations across the thickness of the ring do occur, but on such a small length scale that they are averaged over in a particle impact experiment. This leads to consistent current steps. Because migration usually dominates transport of the particles in impact experiments, the particles are attracted to the ring and remain confined in the cavity.

4.2 Experimental section

Chemicals and Instrumentation. In this study we employed 1,1′-ferrocenedimethanol (Sigma-Aldrich, 372625) as redox mediator and KCl (Sigma-Aldrich, P9333) as supporting electrolyte. All the measurements were performed using 1 μm diameter (standard deviation = 0.03 μm) polystyrene beads (Polysciences, 07310). The zeta potential of the polystyrene beads was measured in working solution (0.67 mM ferrocenedimethanol and 7.5 mM KCl) using a Zetasizer Nano ZS (Malvern Panalytical). The 10 μm disk platinum UME was purchased from BASi (BASi/MF-2005). The Pt disk was polished with alumina slurry (1, 0.3, and 0.05 μm, Buehler, Lake Bluff, U.S.A.). Milli-Q water with 18.2 MΩ·cm^{-1} resistivity (Milli-Q® Advantage A10) was used for preparing all the solutions.

Device Fabrication. Ring and disk UMEs with different diameter were fabricated on the same chips using a combination of thin-film deposition, optical lithography and etching procedures. Figure 4.2a represents the fabrication process flow schematically; the steps described below correspond to the numbered sub-panels in Figure 4.2a. The full process flow is also illustrated in Figure 4.S1.

A one-side polished (OSP) silicon wafer (<100>, boron-doped p-type) with thickness of 525 μm +/– 25 μm was used as substrate. Wet oxidation of silicon was performed to grow a 500 nm SiO_2 layer (step 1). A 100 nm silicon nitride (SiN) layer was then deposited via PECVD (step 2). In step 3, 5 nm titanium (Ti) as the adhesion layer and 50 nm platinum (Pt) were sputtered using an ion-beam system (home-built T'COathy system, MESA+ NanoLab, the Netherlands). Standard optical lithography was then performed to define the geometry of the metal electrodes as well as connecting wires and pads for external connections (step 4). After developing the resist, in step 5, the 50/5 nm Pt/Ti layers were etched via ion beam etching (IBE, Oxfordi300Plus) and the photoresist was stripped with O_2 plasma (TePla300, PAV TePla AG, Germany). In step 6, the second layer of SiN (100 nm) was deposited on the surface via PECVD. In step 7, standard lithography was again performed to expose disk electrodes and mm-scale connections to the device. Then, the exposed SiN layer was etched via reactive ion etching (RIE) with CHF_3/O_2 plasma (home-built TEtske system, MESA+ NanoLab, the Netherlands), and the photoresist was stripped with TePla300 (step 8). In order to create the ring electrodes, standard lithography was again performed as per the above (step 9). The exposed circular areas with diameter of 2.5, 5, and 10 μm were etched using a combination of RIE/IBE/RIE to etch the SiN/Pt/SiN layers, respectively (step 10) and the photoresist was stripped with O_2 plasma. Due to the slow etch rate of the RIE for Pt, IBE was used for etching this layer. Complete etching of the bottom layer of SiN was monitored using optical microscopy; exposure of SiO_2 in the 10 μm diameter wells led to a color change. The wafer was coated with photoresist before dicing to prevent contamination during dicing.

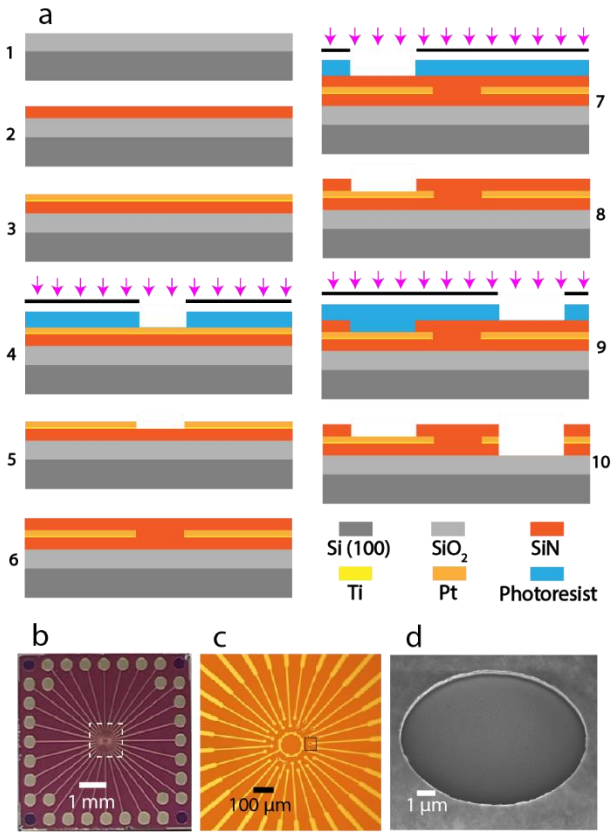

Figure 4.2. (a) Schematic representation of cross-section at different steps of the process flow for the fabrication of disk and ring UMEs: 1- Wet oxidation, 2- SiN deposition by PECVD, 3- Sputtering of Ti and Pt via T'COathy, 4- Lithography (alignment and exposure) and development of the photoresist, 5- Etching Pt and Ti layers via IBE and stripping of the photoresist, 6- SiN deposition via PECVD, 7- Lithography and development of the photoresist, 8- Etching SiN layer via RIE (exposing the disk UMEs and external connections) and stripping of the photoresist, 9- Lithography and development of the photoresist, 10- Etching SiN/Pt-Ti/SiN layers using a combination of RIE/IBE/RIE methods (exposing the ring UMEs) and stripping of the photoresist. (b) Optical microscopy image (top view, scale bar 1 mm) of the fabricated device. (c) Optical microscopy image (top view, scale bar 100 µm) of the fabricated device showing interconnects and electrodes of different sizes at the center. (d) Scanning electron microscopy (SEM) image of a ring UME with diameter of 10 µm and thickness of 50 nm from a 45° viewing angle (scale bar 1 µm). The Pt appears as a bright ring.

Electrochemical Measurements. The measurements were performed using a two-electrode configuration in a custom Faraday cage. No auxiliary electrode was required as the current levels remained on the order of ~1 nA or smaller. A constant potential of +0.35 V was applied

to a microfabricated Pt ring or commercial Pt disk (BASi/MF-2005) working electrode with respect to the Pt pseudo-reference electrode wire (0.20 mm diameter, ~4 mm length exposed to solution), corresponding to an oxidizing overpotential. Data for the commercial UME are shown here to facilitate comparison to other works, but the on-chip disk UMEs yielded equivalent results. A transimpedance amplifier (Femto, DDPCA-300, GmbH, Berlin, Germany) and a homemade Labview (v2013) program were used to monitor the current. The measurements were performed using 1 μm diameter polystyrene particles with a density of 4.55×10^{10} particles/ml (stock solution). The particle solution was diluted 500 times in 0.67 mM ferrocenedimethanol as redox mediator (prepared in MilliQ water) as the working solution for the measurements. We further employed KCl as supporting electrolyte with a concentration of 7.5 mM in all the measurements. The UME was polished mechanically in a figure-eight motion with alumina particles with sizes of 1.0, 0.3 and 0.05 μm polish, rinsing the electrode between the different polishing steps. For the microfabricated devices, individual diced chips were successively cleaned with acetone, MilliQ water and isopropyl alcohol and sonication for 5 min for each step so as to remove a protective photoresist protective layer introduced for dicing. The chips were placed in a homemade stage including a custom socket for making connections (36-pin Land Grid Array (LGA) package, 0.70 mm pitch, Interconnect Devices (IDI)). A polydimethylsiloxane (PDMS) cylinder was used as cell and the pseudo-reference electrode was inserted through the top opening. The experimental geometry is illustrated in Figure 4.S2.

Numerical Simulations. In order to obtain a more quantitative assessment of the current density on disk UMEs, finite-element calculations of the diffusive mass transport of the redox mediator to three-dimensional models of the electrode were performed. These finite-element numerical simulations were performed with COMSOL Multiphysics 5.3a (Supporting Information). The step size was calculated by subtraction of the steady-state current with and without the particle on the surface.

Analysis of experimental current steps. Due to the dependency of the step size on the baseline current, the current step sizes (Δi_{ss}) were normalized to the steady-state current (i_{ss}) immediately before each step, and the $\Delta i_{ss}/i_{ss}$ ratio was used to compare the step sizes in the two geometries. Several measurements were performed to generate sufficient numbers of steps for the statistical analysis. The total numbers of steps were 476 for both the ring and disk UMEs. In order to limit the influence of previously landed particles on the step size, a limited number of collisions (at most 15 collisions from each measurement) was used in the analysis. Using fewer collisions per experiment did not modify the shape of the histograms apart from introducing more statistical noise (Supporting Information). Due to the decrease in the steady-state current, which is particularly pronounced in the first seconds of the measurements, the steps were counted from the second step to step number 16. The step size analysis was performed using a custom script. First, the amperometric measurements were filtered using a Savitzky-Golay filter to remove the high-frequency noise. Each smoothed

curve was then differentiated, and the location of the steps was identified as sharp spikes in the resulting curve (see Supporting Information for details).

4.3 Results and discussion

Our strategy for obtaining consistent signals in current blockade measurements is to create a ring electrode that is smaller in width than the target particles to be detected so that each particle impact event is geometrically equivalent regardless of where it occurs along the circumference of the electrode. For micron-sized particles or smaller, this implies nanoscale ring widths. While electron-beam lithography is a good approach for the fabrication of planar electrodes with such dimensions, it is not widely available and does not lend itself well to large-scale production. In this chapter, we instead focus on standard, widely available optical lithography techniques. To control the width, we rely on the ability to control the deposition of thin films very accurately. As a consequence of this, the ring electrode is embedded in the wall of a shallow cavity rather than being fully planar. The thickness of the ring is determined by the amount of metal deposited. Although the fabricated device in this report could be used for analyzing smaller particles, 1 μm particles were employed to be comparable with the results of a conventional 10 μm disk UME experiment. As illustrated schematically in Figure 4.1b, the particles are bigger than the height of the SiN/Pt/SiN well. As a consequence, there is no direct contact between the particle and the electrode surface, and the landed particles are confined in the corner of the ring by the electric field.

We first present measurements on disk electrodes and analyze the step size distribution in order to provide a baseline against which the ring electrodes can be compared.

Disk UME measurements. The diffusion-limited current to a shrouded disk electrode is given by [26]

$$I_{lim,disk\ UME} = 4nFDCa \qquad (1)$$

Here n is the number of electrons, F is the Faraday constant, D is the diffusion coefficient of the redox species at concentration C, and a is the radius of the disk. A diffusion-limited steady-state current of ≈ 850 pA was obtained experimentally (Figure 4.3a), which is in good agreement with the calculated value using eq 1 ($I_{\mathrm{theoretical}} = 860$ pA, D = 6.7×10^{-10} $m^2 \cdot s^{-1}$).

For the negatively charged 1 μm particles the supporting electrolyte concentration employed here results in migration-limited transport. This is in contrast to transport of the redox mediator, which is diffusion-limited. This regime of transport was chosen to ensure multiple discrete events per measurement over a practical time scale. However, the supporting electrolyte ratio was sufficiently high (> 10) to suppress electroosmotic flows (EOF). This avoided the possibility that EOF could repel the colliding particles from the electrode along the surface, which would lead to current spikes instead of well-defined steps and would

complicate interpretation.[32,33] This regime enables measurement of particles at ultra-low concentrations, decreasing the probability of particle adsorption on UME surfaces before starting the measurements and the probability of particles co-collision during the measurements.

As can be seen in the raw data of Figure 4.3a, the current-time response of blockade impact of 1 μm particles on a 10 μm disk UME exhibits steps with uneven sizes with a range from approximately 1 to 4 pA. A histogram of the normalized magnitude of the steps is shown in Figure 4.3b, illustrating the broad distribution of step sizes in measurements with disk UMEs. This has previously been explained as resulting from the inhomogeneous current distribution at the surface (mediator edge effect).[20,24,25,29] This reasoning can be further formalized as follows. We define the area of the electrode with a radius between r and $r + dr$, where dr is an infinitesimal increment, as $g_r(r)dr = 2\pi r\, dr$. We similarly define the distribution of current step sizes, $g_{\Delta i}(\Delta i)d(\Delta i)$, as the relative number of sites on the electrode where the step size falls in the range Δi to $\Delta i + d(\Delta i)$. Δi is a function of r because of the non-uniform mediator flux density. Equating $g_r(r)dr = g_{\Delta i}(\Delta i)d(\Delta i)$ yields

$$g_{\Delta i}(\Delta i) = \frac{2\pi r}{d(\Delta i(r))/dr} \qquad (2)$$

The probability that a particular step has an amplitude Δi is proportional to $g_{\Delta i}(\Delta i)$, since this dictates the number of sites that yield this value of Δi, times the particle flux to that region. Noting that the mediator current density $j(r)$ at a disk electrode as a function of radial position r has the form[34]

$$j(r) = j_0/\sqrt{1-(r/a)^2} \qquad (3)$$

and that that the migrational transport of particles resulting from the residual ohmic electric field approximates the same form, we have for the expected probability density of step sizes

$$P(\Delta i) = \frac{B}{\sqrt{1-(r/a)^2}}\frac{2\pi r}{d(\Delta i(r))/dr} \quad (r < a) \qquad (4)$$

Here B is a normalization factor independent of r. In this simple model $P(\Delta i) = 0$ for $r > a$ since there is no electric field driving the particles to the insulating shroud, however note that this simplification would need to be lifted for situations where diffusion contributes substantially to particle mass transport.

In order to evaluate eq 4 for $P(\Delta i)$, it is necessary to have an expression for the dependence of the step size $\Delta i(r)$ on r. We evaluated this function using finite-element methods, as detailed further in the Supporting Information. The final predicted distribution, which does not include any free parameter, is shown in Figure 4.3b. It exhibits two peaks. The peak at high step sizes corresponds to particles landing near the edge; although this corresponds to a small area, the collision density is high due to the stronger electric field caused by the higher diffusive flux of redox mediator in this region. The peak at low step sizes corresponds to

collisions in the central area of the disk with a larger area but a lower current density and electric field. While there is good agreement between the predicted and measured range of current step sizes, the sharp peaks in the distribution are not observed in the experiment. We attribute this additional broadening to elements missing in the model including residual EOFs and the influence of the finite particle size on migration in a non-uniform electric field.

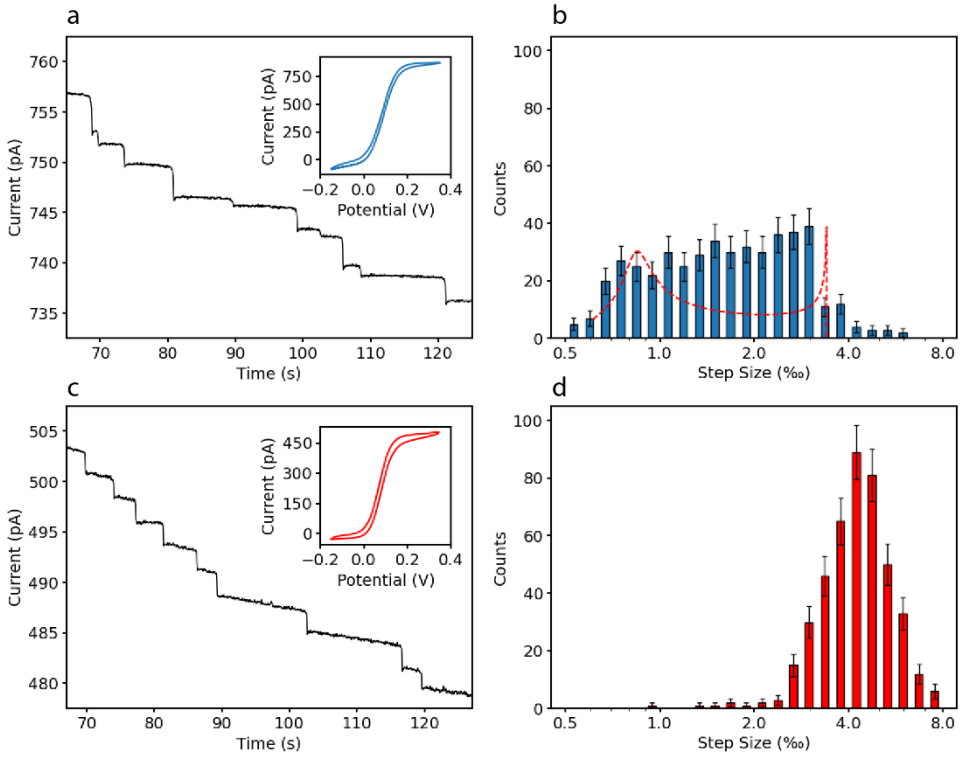

Figure 4.3. (a) The current-time response of blockade impact measurement with 10 μm disk UME and 1 μm negatively charged particles in 0.67 mM ferrocenedimethanol solution exhibits uneven current steps with a range from ≈1 to 4 pA. (b) Histogram of the step sizes for 476 current steps obtained in different measurements. The red dashed curve represents the distribution obtained from eq 4 with no fitting parameter. (c) Chronoamperograms and CV of the measurements with the fabricated recessed ring electrodes with 10 μm diameter and 50 nm thickness. (d) Histogram of the step sizes for the 10 μm ring. The x-axes in (b) and (d) show the step size per mille (‰) on a logarithmic scale (the data are also shown on a linear scale in the Supporting Information). The step size is normalized by the current immediately before each step. This facilitates comparison with previous reports with different geometries and measurements at different redox mediator concentrations.[29]

Ring UME measurements. The geometry of the microfabricated ring UMEs was shown in Figure 4.2. The ring electrodes were positioned in a shallow cylindrical cavity with the

electrode located on the side wall of the cavity. The current to a thin planar ring (in the limit where the width of the ring Δ is much smaller than the ring radius ρ, $\Delta \ll \rho$) is

$$I_{lim,ring} = nFDC \frac{2\pi^2 \rho}{\ln\left(\frac{32\rho}{\Delta}\right)} \quad (5)$$

While our geometry is more complex, this expression serves as a first approximation to estimate the current levels that can be expected. The ratio of this current and of that at a disk with the same radius ($a = \rho$) is $I_{lim,ring}/I_{lim,disk} \approx \pi^2/2 \ln(32\rho/\Delta)$. The slow inverse logarithmic dependence of this ratio on the ring width, Δ, insures that even a thin ring can exhibit total currents of the same order of magnitude as a disk UME of corresponding diameter. In particular, eq 5 predicts a ratio $I_{lim,ring}/I_{lim,disk} \approx 0.6$ for our 10-μm diameter devices, which is remarkable considering that the electrode area is a factor ≈ 50 times smaller for the ring.

The measurements with ring UMEs were performed under the same conditions as the disk measurements. The voltammogram of the fabricated 10-μm diameter and 50 nm thick ring UME exhibits the typical sigmoidal shape for diffusion-limited transport (inset, Figure 4.3c). A limiting current of ≈ 500 pA was obtained. This corresponds to $I_{lim,ring}/I_{lim,disk} = 0.59$, in good agreement with the theoretical estimate.

Figure 4.3c shows the amperometric response of a 10 μm diameter ring UMEs during a current blockade measurement. Qualitatively, the response exhibits relatively uniform step sizes. The frequency of collisions is comparable to that for the disk electrode, consistent with the similar magnitude of the current. Figure 4.3d shows the corresponding histogram of step sizes. The ring UME results in a single, relatively narrow, peak representing uniform current step sizes. This confirms the expectation of a more uniform current density along the perimeter of the ring, in such a way that collision of the particles anywhere on the ring block a similar amount of redox mediator.

More quantitatively, the standard deviations of the step size for the disk electrode (blue histogram) and ring electrode (red histogram) are 0.25 and 0.13, respectively. In addition to the uniformity of the signals, ring UMEs exhibit larger relative step sizes. These two observations translate into a higher relative step size sensitivity for rings under identical conditions.

The histogram in Figure 4.3d nevertheless exhibits a significant width. One might try to explain this broad histogram as resulting from particles landing close to each other after multiple collisions. If this were the case, analyzing a lower number of steps per measurement should result in a narrower distribution. However, the histogram shape and standard deviation of the step size remain nearly unchanged in the ring UME when analyzing the first 10, 7, or 5 steps of the same measurements (Figure 4.S5), ruling out this mechanism.

The breadth of the histograms could also be due to nonidealities in the experiment. One possibility is material redeposition in the inner wall of the cavity in the last etching steps leading to a nonuniform metal thickness. This non-uniformity can be improved in the future by implementing alternative approaches for etching the SiN/Pt/SiN stack. Material redeposition as well as an uneven etch depth inside the ring may also lead to different particle heights when adsorbing inside the ring. This can be mitigated in the future by etching deeper so that the particles adsorb onto the electrode ring itself without touching the bottom of the cavity. Another potential issue is adsorption of the particles at random locations since no particular measures were taken to protect against it. A final possibility is that the assumption that all particles get jammed at the inner edge of the cavity due to electrophoretic forces, as in Figure 4.1b, is oversimplified. Due to the nanoscopic height of the ring electrodes, the electric field gradients created are much larger than at conventional UMEs. This may lead to additional effects such as dielectric forces, or electroosmosis that can normally be ignored at the salt concentrations employed here. We envision that particles may get trapped on the surface surrounding the cylindrical cavity due to this complex balance of forces. Increasing the height of the top and bottom layers of SiN or employing smaller particles in a device with a thinner Pt layer can diminish this effect. Finally, a true planar ring geometry could be implemented, at the cost of requiring more sophisticated microfabrication equipment.

4.4 Conclusion and outlook

Here we explored the use of ring electrodes with a nanoscale width as an alternative tool for detecting insulating particles via current blockade impact electrochemistry. We argued that the broad distribution of step sizes for a disk can be explained semi-quantitatively by a simple model taking into account the nonuniform current distribution over the surface of the electrode together with the resulting nonuniform migrational flux of particles. In order to diminish the edge effect, we designed and fabricated a ring geometry based on a thin strip electrode sandwiched between insulating materials. The current blockade impact measurements using ring UMEs showed larger and more uniform relative step sizes compared to a disk with the same diameter. In particular, the distribution of step sizes for the ring UME is narrow enough to reliably identify the simultaneous collision of two particles as a double-sized step. Also, the occurrence of a single step size distribution should allow accurate particle size determination. This geometry further addresses the particle displacement problem that leads to false collision events. The step size uniformity can be further improved by fabricating devices with more optimized geometries. The use of these ring UMEs is not limited to current blockade: the fabrication process is relatively straightforward and can be applied to different materials, such that the advantages of ring UMEs can also be exploited in other impact electrochemistry methods.

4.5 Supporting information

4.5.1 Detailed fabrication process flow

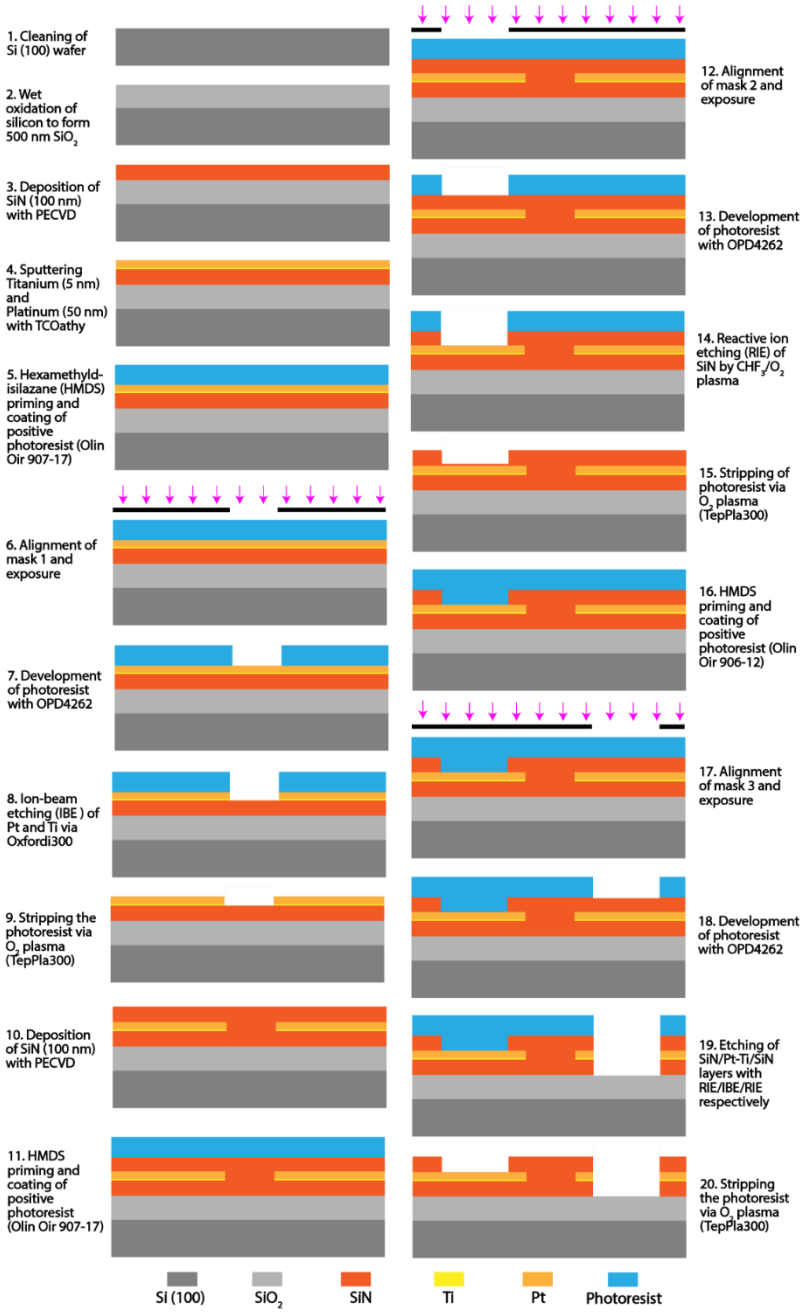

Figure 4.S1. Schematic representation of cross-sections at different steps of the process flow for the fabrication of the disk and ring UMEs; 1- Wafer cleaning, 2- Wet oxidation, 3- SiN deposition, 4- Sputtering of Ti and Pt, 5- Coating of the positive photoresist (Olin Oir 907-17), 6- Alignment and exposure, 7- Development of the photoresist with OPD4262, 8- Etching Pt and Ti layers via IBE, 9- Stripping of the photoresist with O2 plasma, 10- SiN deposition via PECVD, 11- Coating of the photoresist, 12- Alignment and exposure, 13- Development of the photoresist, 14- Etching SiN layer via RIE (exposing the disk UMEs and connections), 15- Stripping of the photoresist with O2 plasma, 16- Coating of the positive photoresist (Olin Oir 906-12), 17- Alignment and exposure, 18- Development of the photoresist, 19- Etching SiN/Pt-Ti/SiN layers using a combination of RIE/IBE/RIE methods (exposing the ring UMEs), 20- Stripping of the photoresist with O2 plasma.

4.5.2 Measurement setup

The chip is placed in a custom stage that includes spring-loaded pins to establish electrical contact to the electrodes. A PDMS cylinder is used as a cell. The pseudo-reference electrode is inserted through the top opening. The contact between the PDMS and the chip surfaces can be checked by optical microscopy to ensure that there is no leakage in the cell.

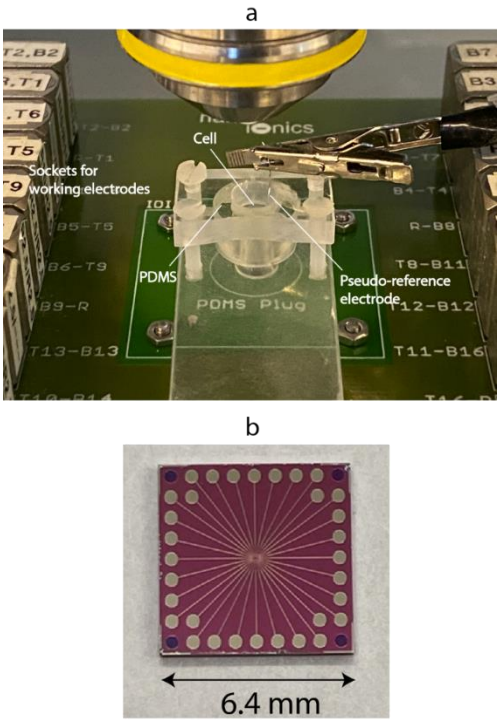

Figure 4.S2. (a) Assembled two-electrode cell. (b) The fabricated device.

4.5.3 Obtaining the step size distribution from eq 4

The calculated step size distribution for a disk electrode shown in Figure 4.3b was obtained from eq 4. Doing so requires knowledge of the quantity $d(\Delta i(r))/dr$, where $\Delta i(r)$ is the current step size for a particle landing at radial coordinate r. In order to determine $\Delta i(r)$, finite-element calculations were performed using COMSOL Multiphysics 5.3a. A report of a typical computation is provided separately. The resulting values are shown as solid symbols in Figure 4.S3. These results were then fitted to a fifth-order polynomial to generate a smooth curve that could be differentiated and input into eq 4. The fitted polynomial had values

$$\Delta i(r) = 0.00140r^5 + 0.00149r^4 - 0.0441r^3 + 0.121r^2 - 0.000896r + 0.614$$

where r has units of micrometers and Δi has units of nA.

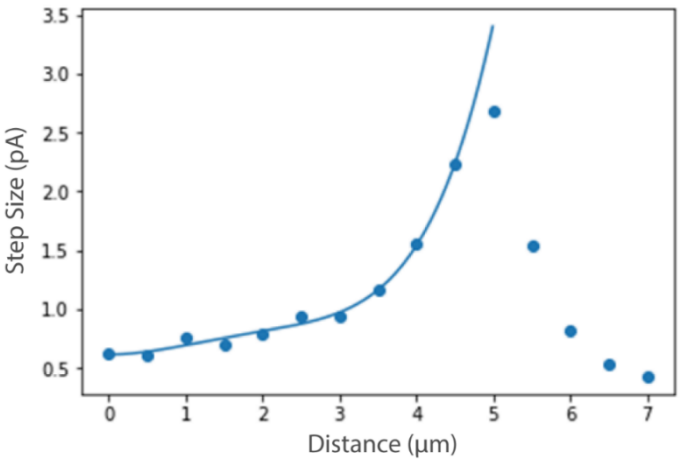

Figure 4.S3. Numerically calculated values of $\Delta i(r)$ and corresponding polynomial fit.

4.5.4 Current step analysis

The analysis of the chronoamperograms was performed with a self-produced Python program developed by T. Walstra. In short, the program uses a current-time response as input. It applies a filter to smooth out the noise, differentiates the signal, and identifies the peaks that exceed a certain threshold in the resulting curve. Peaks in this signal correspond to steps in the chronoamperogram.

In the first step, the current-time response is filtered using a Savitzky-Golay filter to remove high-frequency noises and unwanted spikes. The filter fits polynomials through groups of adjacent data points. The order of this polynomial and the window length can be given as parameters as well as the derivative order. In practice, the polynomial order, the window length, and the derivative order were 5, 31, and 1 respectively. Then, the resulting smoothed curves are differentiated and used for step finding (Figure 4.S4).

In the next step, the current step is isolated and an analytical function with a linear baseline is fitted through the data points. This directly gives, among other parameters, the height of the step. The step-like function used for steps analysis is

$$\frac{H}{1 + e^{-k(t-t_0)}} + m(t - t_0) + b$$

where t is the independent variable, H is the height of the step, k is the steepness of the step, t_0 is the time at which the step occurs, m is the slope of the baseline current before the step, and b is the baseline value directly after the step. The procedure for analyzing a full chronoamperogram is automated, but the user can also check for false positives caused by noise.

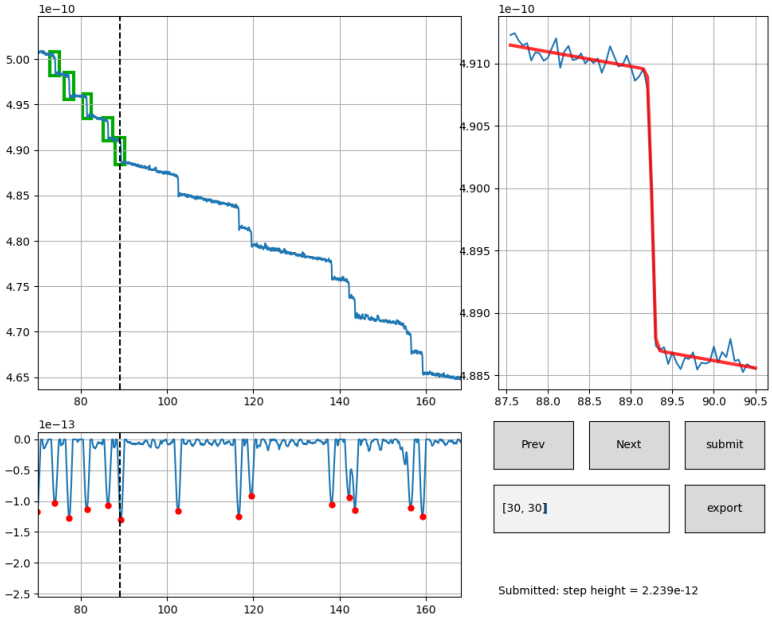

Figure 4.S4. Screenshot of the analysis tool. Top left: raw measurement data (the black dashed line indicates the particular step being analyzed, green boxes indicate previously analyzed steps). Bottom left: derivative of the filtered data (red dots indicate a peak corresponding to a step candidate). Top right: isolated step currently being analyzed (blue) together with its best fit (red). Buttons allow navigating through the complete trace.

4.5.5 Histograms

One possible concern is that the magnitude of the events can depend on previous history when multiple particles land in each other's vicinity. However, analyzing lower numbers of steps for each trace results in histograms with a similar shape, indicating that retaining 15 events per trace does not significantly influence the distribution.

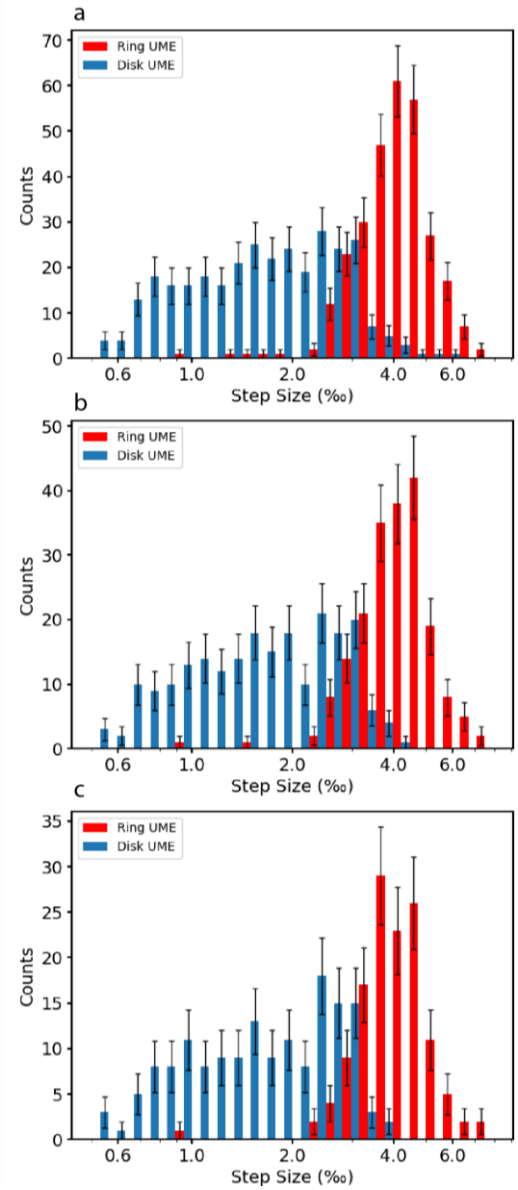

Figure 4.S5. Analysis with a lower number of steps in the measurements of disk and ring UMEs. The histograms shape remains nearly unchanged in both disk and ring UMEs for the first 10 (a), 7 (b), and 5 (c) steps. The x-axis shows the step size per mille (‰) relative to the baseline current just before the step on a logarithmic scale. The standard deviations of the step size for the first 10, 7, and 5 steps in disk and ring UMEs are (0.24, 0.12), (0.23, 0.12), and (0.23, 0.11), respectively. The smallest steps in the ring measurements can be due to the collision of particles near previously landed particles.

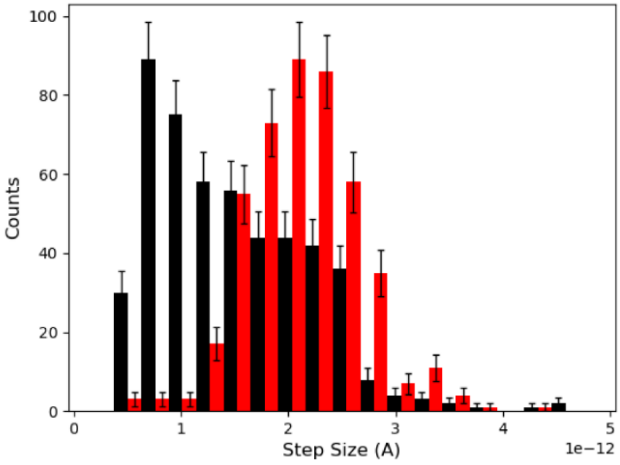

Figure 4.S6. Histograms of the step sizes for ring and disk UMEs plotted on a linear axis (same data as Figure 4.3). Note that while the variance in the absolute step size is comparable for both situations, the disk electrode exhibits a broad distribution that varies over a factor of ~5 while the ring electrode exhibits a peaked distribution around 2 pA.

4.6 References

(1) Moazzenzade, T.; Huskens, J.; Lemay, S. G. Stochastic electrochemistry at ultralow concentrations: the case for digital sensors. *Analyst* **2020**, *145*, 750−758.
(2) Sokolov, S. V.; Eloul, S.; Kätelhön, E.; Batchelor-McAuley, C.; Compton, R. G. Electrode–particle impacts: a users guide. *Phys. Chem. Chem. Phys.* **2017**, *19*, 28-43.
(3) Xiao, X.; Fan, F.-R. F.; Zhou, J.; Bard, A. J. Current transients in single nanoparticle collision events. *J. Am. Chem. Soc.* **2008**, *130*, 16669-16677.
(4) Dasari, R.; Robinson, D. A.; Stevenson, K. J. Ultrasensitive Electroanalytical Tool for Detecting, Sizing, and Evaluating the Catalytic Activity of Platinum Nanoparticles. *J. Am. Chem. Soc.* **2013**, *135*, 570-573.
(5) Kleijn, S. E. F.; Lai, S. C. S.; Miller, T. S.; Yanson, A. I.; Koper, M. T. M.; Unwin, P. R. Landing and Catalytic Characterization of Individual Nanoparticles on Electrode Surfaces. *J. Am. Chem. Soc.* **2012**, *134*, 18558-18561.
(6) Bentley, C. L.; Kang, M.; Unwin, P. R. Time-Resolved Detection of Surface Oxide Formation at Individual Gold Nanoparticles: Role in Electrocatalysis and New Approach for Sizing by Electrochemical Impacts. *J. Am. Chem. Soc.* **2016**, *138*, 12755-12758.
(7) Kwon, S. J.; Zhou, H.; Fan, F.-R. F.; Vorobyev, V.; Zhang, B.; Bard, A. J. Stochastic electrochemistry with electrocatalytic nanoparticles at inert ultramicroelectrodes—theory and experiments. *Phys. Chem. Chem. Phys.* **2011**, *13*, 5394-5402.
(8) Park, J. H.; Thorgaard, S. N.; Zhang, B.; Bard, A. J. Single Particle Detection by Area Amplification: Single Wall Carbon Nanotube Attachment to a Nanoelectrode. *J. Am. Chem. Soc.* **2013**, *135*, 5258-5261.

(9) Sardesai, N. P.; Andreescu, D.; Andreescu, S. Electroanalytical Evaluation of Antioxidant Activity of Cerium Oxide Nanoparticles by Nanoparticle Collisions at Microelectrodes. *J. Am. Chem. Soc.* **2013**, *135*, 16770-16773.
(10) Robinson, D. A.; Kondajji, A. M.; Castañeda, A. D.; Dasari, R.; Crooks, R. M.; Stevenson, K. J. Addressing Colloidal Stability for Unambiguous Electroanalysis of Single Nanoparticle Impacts. *J. Phys. Chem. Lett.* **2016**, *7*, 2512-2517.
(11) Dasari, R.; Robinson, D. A.; Stevenson, K. J. *J. Am. Chem. Soc.* **2012**, *135*, 570.
(12) Fernando, A.; Parajuli, S.; Alpuche-Aviles, M. A. Observation of Individual Semiconducting Nanoparticle Collisions by Stochastic Photoelectrochemical Currents. *J. Am. Chem. Soc.* **2013**, *135*, 10894-10897.
(13) Toh, H. S.; Compton, R. G. 'Nano-impacts': An Electrochemical Technique for Nanoparticle Sizing in Optically Opaque Solutions. *ChemistryOpen* **2015**, *4*, 261-263.
(14) Castañeda, A. D.; Brenes, N. J.; Kondajji, A.; Crooks, R. M. Detection of microRNA by electrocatalytic amplification: a general approach for single-particle biosensing. *J. Am. Chem. Soc.* **2017**, *139*, 7657-7664.
(15) Dick, J. E.; Renault, C.; Bard, A. J. Observation of single-protein and DNA macromolecule collisions on ultramicroelectrodes. *J. Am. Chem. Soc.* **2015**, *137*, 8376-8379.
(16) Kwon, S. J.; Bard, A. J. DNA analysis by application of Pt nanoparticle electrochemical amplification with single label response. *J. Am. Chem. Soc.* **2012**, *134*, 10777-10779.
(17) Dick, J. E.; Hilterbrand, A. T.; Strawsine, L. M.; Upton, J. W.; Bard, A. J. Enzymatically enhanced collisions on ultramicroelectrodes for specific and rapid detection of individual viruses. *Proc. Natl. Acad. Sci. U. S. A.* **2016**, *113*, 6403-6408.
(18) Castañeda, A. D.; Robinson, D. A.; Stevenson, K. J.; Crooks, R. M. Electrocatalytic amplification of DNA-modified nanoparticle collisions via enzymatic digestion. *Chem. Sci.* **2016**, *7*, 6450-6457.
(19) Lemay, S. G.; Moazzenzade, T. Single-Entity Electrochemistry for Digital Biosensing at Ultralow Concentrations. *Anal. Chem.* **2021**, *93*, 9023-9031.
(20) Quinn, B. M.; van't Hof, P. G.; Lemay, S. G. Time-resolved Electrochemical Detection of Discrete Adsorption Events. *J. Am. Chem. Soc.* **2004**, *126*, 8360-8361.
(21) Ronspees, A. T.; Thorgaard, S. N. Blocking Electrochemical Collisions Of Single E. coli And B. subtilis Bacteria At Ultramicroelectrodes Elucidated Using Simultaneous Fluorescence Microscopy. *Electrochim. Acta.* **2018**, *278*, 412-420.
(22) Lebègue, E.; Anderson, C. M.; Dick, J. E.; Webb, L. J.; Bard, A. J. Electrochemical Detection of Single Phospholipid Vesicle Collisions at a Pt Ultramicroelectrode. *Langmuir* **2015**, *31*, 11734-11739.
(23) Renault, C.; Lemay, S. G. Electrochemical Collisions of Individual Graphene Oxide Sheets: An Analytical and Fundamental Study. *ChemElectroChem.* **2020**, *7*, 69-73.
(24) Boika, A.; Thorgaard, S. N.; Bard, A. J. Monitoring the Electrophoretic Migration and Adsorption of Single Insulating Nanoparticles at Ultramicroelectrodes. *J. Phys. Chem. B.* **2012**, *117*, 4371-4380.
(25) Fosdick, S. E.; Anderson, M. J.; Nettleton, E. G.; Crooks, R. M. Correlated Electrochemical and Optical Tracking of Discrete Collision Events. *J. Am. Chem. Soc.* **2013**, *135*, 5994-5997.
(26) Bard, A. j.; Faulkner, L. R. *Electrochemical Methods: Fundamentals and Applications*; John Wiley & Sons, 2001.

(27) Bonezzi, J.; Boika, A. Deciphering the Magnitude of Current Steps in Electrochemical Blocking Collision Experiments and Its Implications. *Electrochim. Acta* **2017**, *236*, 252-259.
(28) Dick, J. E.; Hilterbrand, A. T.; Boika, A.; Upton, J. W.; Bard, A. J. Electrochemical detection of a single cytomegalovirus at an ultramicroelectrode and its antibody anchoring. *Proc. Natl. Acad. Sci. U. S. A.* **2015**, *112*, 5303-5308.
(29) Deng, Z.; Elattar, R.; Maroun, F.; Renault, C. In Situ Measurement of the Size Distribution and Concentration of Insulating Particles by Electrochemical Collision on Hemispherical Ultramicroelectrodes. *Anal. Chem.* **2018**, *90*, 12923-12929.
(30) Ma, C.; Contento, N. M.; Gibson, L. R.; Bohn, P. W. Redox Cycling in Nanoscale-Recessed Ring-Disk Electrode Arrays for Enhanced Electrochemical Sensitivity. *ACS Nano* **2013**, *7*, 5483-5490.
(31) Fu, K.; Han, D.; Ma, C.; Bohn, P. W. Electrochemistry at single molecule occupancy in nanopore-confined recessed ring-disk electrode arrays. *Faraday Discuss.* **2016**, *193*, 51-64.
(32) Moazzenzade, T.; Yang, X.; Walterbos, L.; Huskens, J.; Renault, C.; Lemay, S. G. Self-Induced Convection at Microelectrodes via Electroosmosis and Its Influence on Impact Electrochemistry. *J. Am. Chem. Soc.* **2020**, *142*, 17908-17912.
(33) Thorgaard, S. N.; Jenkins, S.; Tarach, A. R. Influence of Electroosmotic Flow on Stochastic Collisions at Ultramicroelectrodes. *Anal. Chem.* **2020**, *92*, 12663-12669.
(34) Saito, Y. A Theoretical Study on the Diffusion Current at the Stationary Electrodes of Circular and Narrow Band Types. *Rev. Polarogr.* **1968**, *15*, 177-187.

Utilizing the oxygen reduction reaction in particle impact electrochemistry: a step toward mediator-free digital electrochemical sensors

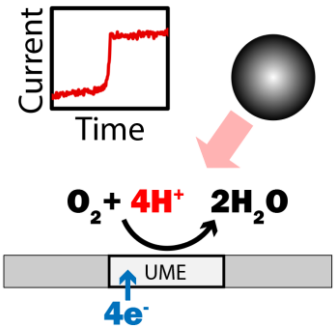

The current blockade particle impact method opens a route towards highly parallelized single-entity electrochemical assays. An important limitation is however that a redox mediator must be present in the sample, which can detrimentally interfere with molecular recognition processes. Dissolved O_2 that is naturally present in aqueous solutions under ambient conditions can in principle serve as a suitable mediator via the oxygen reduction reaction (ORR). Here we demonstrate the validity of this concept by performing current blockade experiments to capture and detect individual microparticles at Pt microelectrodes using solely the ORR. The readout modality is independent of the absolute O_2 concentration, allowing operation under varying conditions. We further determine how the trajectories of individual microparticles are influenced by the combination of electrophoresis and electroosmotic flows, and how these can be utilized to provide continuous detection of cationic particles in water for environmental monitoring.

The contents of this chapter are published as: Moazzenzade, T.; Huskens, J.; Lemay, S. G. Utilizing the oxygen reduction reaction in particle impact electrochemistry: a step toward mediator-free digital electrochemical sensors. *ACS Omega*. Publication date: August 15, **2023.** The movies are freely available at: https://doi.org/10.1021/acsomega.3c03576.

Oxygen is the most common oxidant for fuel cell cathodes in sustainable energy technology.[1] While the oxygen reduction reaction (ORR) is omnipresent in energy harvesting technology, it is not as frequently used in electrochemical (bio)sensing. This is despite the fact that the ORR was the key reaction in the first reported biosensor, the glucose sensor,[2,3] in which oxygen consumption by glucose oxidase was monitored to infer glucose concentration.[3] However, due to the stoichiometric limitation of dissolved oxygen (the so-called "oxygen deficit"), oxygen was replaced with synthetic electron acceptors in the next generation of glucose biosensors.[2] Redox mediators such as ferrocene derivatives, ferricyanide, and quinone compounds were employed instead of oxygen as electron acceptor partners.[4] Due to the insensitivity of these mediators to pH, their lower redox potential, and their electrochemically reversible nature, these mediators with outer-sphere electron transfer mechanisms became the conventional species in heterogeneous electron transfer reactions in nearly all amperometric biosensors.[5] ORR has also been used recently as the catalytic reaction in electrochemical immunosensors, where nanostructures that are electroactive for the ORR have been employed as labels for signal amplification,[6-16] and for indirect signal generation in surface (bio)sensors.[17-19]

Single-entity electrochemical sensors, like their macroscopic antecedents, often rely on redox species for electron transfer and signal generation.[20,21] Particle impact electrochemistry methods, in particular, employ redox mediators for detecting analytes as discrete events in the current-time response.[21-24] In blockade impact electrochemistry, in particular, the current generated by the flux of mediator to an ultramicroelectrode (UME) is partially blocked by the collision of non-electroactive particles, leading to step-like decreases in the amperometric response.[22] In contrast, in mediated faradaic impact methods, redox mediators undergo oxidation or reduction on the surface of electroactive particles that collide with an otherwise inert UME, leading to amplified current spikes in the current-time response.[23] Redox mediators such as ferrocene derivatives, potassium ferrocyanide, hydrazine, $NaBH_4$, *etc*., have been employed in impact measurements for biosensing applications[25-28] and for analysing electrocatalysts.[29,30] Faradaic impact electrochemistry has been employed to study the ORR at catalysts such as Pt nanoparticles[31-34] and multiwalled carbon nanotubes.[35] Resolving heterogeneity in catalytic activity within nanoparticle populations can be addressed in this manner[31] under different conditions including alkaline[35] and acidic[33] solutions as well as high pressures.[31]

Here, we employ the ORR in blockade impact electrochemistry for detecting microparticles under physiological salt conditions. Our motivation for employing the ORR is to enable single-entity electrochemical (bio)sensors while sidestepping the undesirable consequences of introducing artificial mediators, which include interference with biochemical processes as well as electrode fouling. We show that the concentration of dissolved oxygen in a physiological buffer (PBS) under ambient conditions is sufficient for signal generation *in-vitro* when using a Pt microelectrode. The ORR in fact leads to large mediator currents due

to its being a 4-electron reaction and to oxygen's large diffusion coefficient compared to conventional redox mediators. The electric field that is generated by the ORR leads to the migration and collision of positively charged particles on the UME surface that can be observed as discrete blockade signals. As simple prototypical application, we show here that ultralow concentrations of positively charged microparticles can be detected via ORR-driven blockade impact electrochemistry. This approach is distinct from and complementary to an earlier study of detection based on oxygen-carrying microparticles.[36] Plastic particles are of increasing concern as health issues: they have been detected in drinking water,[37] and their accumulation and toxicity have been studied in plants,[38] plankton,[39] algae,[40] bacteria,[41] and even in human blood.[42] Among these particles, positively charged microplastics have shown higher cellular uptake, accumulation, and cytotoxicity in comparison to similar negative particles.[43] We further show that by tuning the UME surface, particles can be detected in a dynamic "kiss-and-run" interaction mode rather than permanent adsorption. Through surface functionalization, this approach can be used as a continuous monitoring system for the digital detection of plastic particles in aqueous solutions such as drinking water. For comparison, we also employ the ORR for detecting Pt nanoparticles via mediated faradaic impact electrochemistry (Supporting Information).

5.1 Experimental section

All measurements were performed using 1 µm diameter positively charged amidine-coated latex particles (Invitrogen™ number A37322, with de-ionized water as medium, ζ-potential = +32 mV). A 10 µm diameter glass-encased Pt UME (BASi/MF-2005) was used for all measurements. Phosphate buffered saline (PBS) (composition: 0.01 M phosphate buffer, 0.0027 M potassium chloride and 0.137 M sodium chloride, pH 7.4, at 25 °C) was used as the buffer in the measurements (Sigma, P4417). For blockade impact measurements, a constant potential of −0.7 V was applied to the Pt UME with respect to the Pt wire pseudo-reference electrode (wire diameter 0.20 mm, ≈10 mm length exposed to solution), corresponding to a highly reducing overpotential. The current was monitored using a transimpedance amplifier (Femto, DDPCA-300). A microscope (Zeiss/Axio Scope Vario) with a LD EC "Epiplan-Neofluar" 50x/0.55 DIC M27 objective (parfocal length = 45 mm, free working distance = 9.1 mm) was used for optical microscopy, recording the motion of the particles in two dimensions simultaneously with the amperometric measurement. Poly-L-lysine hydrobromide (Sigma-Aldrich, P7980) was used for surface functionalization (0.1 mg/ml in PBS buffer on a magnet stirrer for 10 min). For mediated faradaic impact measurements (Supporting Information), a 11 µm diameter carbon UME (BASi) and 50 nm Pt particles (locally synthesized) were used for the measurements.

5.2 Results and discussion

5.2.1 Cyclic voltammetry

Cyclic voltammetry was performed to evaluate the steady-state limiting current of the ORR on a 10-µm Pt disk UME in PBS buffer (pH 7.4). Depending on the pH of the solution, a direct 4-electron reaction or indirect peroxide pathway dominates.[44] Figure 5.1 (black curve) shows the voltammograms for a sweep potential between -0.7 and -0.1 V vs a Pt pseudo-reference electrode.

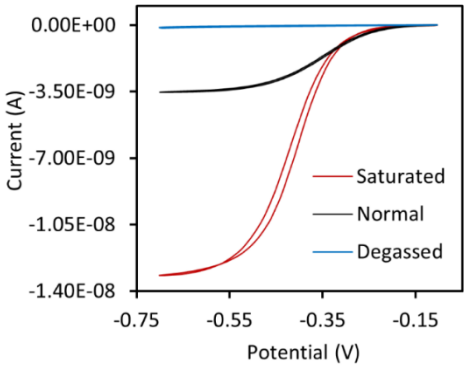

Figure 5.1. Cyclic voltammograms measured at a Pt disk UME vs Pt wire at a scan rate of 0.05 V/s in PBS (black curve), PBS degassed with N_2 (blue curve), and PBS saturated with pure O_2 (red curve). The potential is applied with respect to a Pt pseudo-reference electrode in a two-electrode configuration.

The sigmoidal shape of the curve is typical for diffusion-limited transport at a microelectrode, where the limiting current to the UME is given by $I_{lim} = 4nFDCa$. Here n is the number of transferred electrons, F is the Faraday constant, D is the diffusion coefficient of the reactant at concentration C, and a is the radius of the shrouded disk electrode. The expected limiting ORR current for a diffusion coefficient of O_2 of 2.1×10^{-5} cm^2 s^{-1},[45] $n = 4$, and a concentration of 0.21 mM for water in equilibrium with atmospheric conditions,[31] is $I_{lim} \approx 3.4$ nA. This compares favorably with the limiting current of ≈ 3.5 nA obtained from the CV, confirming that the 4-electron reaction ($O_2 + 4H^+ + 4e^- \rightarrow 2H_2O$) is favored in comparison to the indirect two-electron pathway.[31,46] A slight shift in the half-wave potential is also observed, which has been attributed to insufficient buffer capacity when the O_2 concentration becomes too high.[31]

In order to confirm the voltammogram shape and the dependency of the limiting-current level on oxygen concentration, the PBS solution was fed with pure O_2 and degassed with N_2. The red and blue curves in Figure 5.1 show the increased and decreased limiting current levels upon oxygen saturation and depletion, respectively. In both measurements, the limiting

current levels returned to their initial values with time in the following cycles through exposure to air as equilibrium was re-established (Supporting Information Figure 5.S1).

5.2.2 Blockade impact measurements

Blockade impact measurements were performed using a Pt UME biased at negative potentials corresponding to the limiting current. Positively charged 1-µm diameter particles (amidine-modified latex beads, ζ-potential = +32 mV) were used for this measurement. The PBS solution was diluted 25 times to decrease the ionic strength. This ensured that the flux of charged particles was dominated by migration instead of diffusion and yielded a high event rate.[21] Reduction of oxygen at the Pt UME generates an electric field with a polarity such as to cause migration of positively charged particles toward the UME. The arrival of these charged particles at the UME interfered with the mass transport of O_2. Figure 5.2 presents a typical current-time response for the blockade of the ORR by positively charged microparticles at a potential of -0.7 V vs the Pt pseudo-reference electrode. Each positive step (decrease in current magnitude) corresponds to a single particle arriving at the electrode.

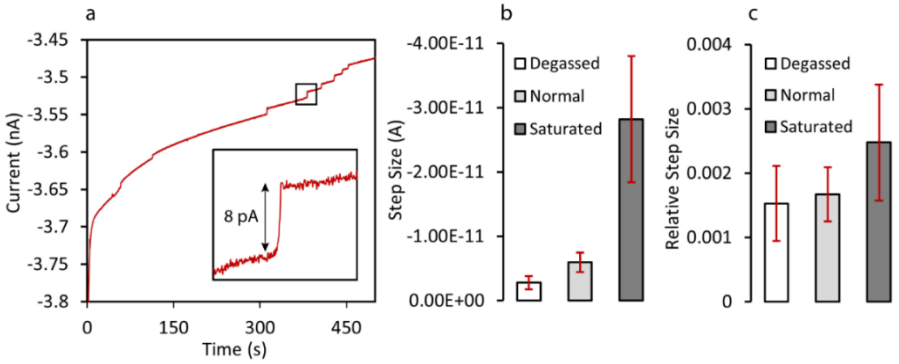

Figure 5.2. (a) Discrete current steps of blockade of ORR by colliding positively charged particles on a Pt UME when biased at negative potentials in diluted PBS solution (25X). (b) absolute and (c) relative step sizes at different oxygen concentrations (white: partially degassed solution, gray: normal solution, dark gray: oxygen-saturated solution). The error bars represent standard deviation (10 samples) which originates largely from the inhomogeneous current distribution on the electrode surface.[47,48]

Due to the independence of the relative step size to the limiting current level,[22,49,50] ORR-driven blockade impact is self-calibrating for measurements at different O_2 concentrations. To show the effect of oxygen concentration on the signal-to-noise ratio, impact measurements were performed with oxygen saturated and partially degassed PBS solutions. As can be seen in Figure 5.2b and c, $\Delta I/I$ remained essentially unchanged when detecting similar particles in different oxygen concentrations. The independence of the relative signal size on the O_2 concentration means that ORR-driven blockade impact can also be employed under circumstances where the O_2 concentration is poorly known or varies with time.[51]

5.2.3 Particle trajectories

Optical microscopy was performed to analyze the trajectories of the particles. Supplementary Movie 1 and 2 show the motion of positively charged particles during blockade impact measurements. Charged particles can be seen to move along the surface of the glass shroud and enter the UME area (see also Figure 5.3a). These trajectories[52] are in the opposite direction from the trajectories for an oxidation reaction (e.g., using a ferrocene-based mediator) in which particles typically approach the electrode from above (Figure 5.3b).[53,54] This is attributed to electroosmotic flows (EOF), in which the generation of charged species at the UME induces a tangential electric field that causes electroosmosis in the vicinity of the charged insulating material (glass).[53,54] The fields induced by the oxidation reaction have the opposite polarity from the reduction case, leading to the reversal of both electrophoretic and EOF-induced forces on the particles. At high salt concentration (Movie 1), positively charged particles move along the surface and adsorb onto the edge of the UME. This leads to step-like decreases in the current-time response. A consequence of this sort of trajectory is that particles prefer to adsorb near the rim of the disk, where the current density is highest. Hence collided particles do not rearrange on the UME surface as they do in oxidative systems.[49,55] Employing reductive reactions like ORR may thus decrease error in particle-counting measurements by suppressing false events caused by particle rearrangement. We also note that EOF-induced forces could contribute to the rearrangement mechanism for oxidative reactions, but this has not been investigated to date.

At lower concentrations of salt, the EOF becomes more dominant and further affects the particle trajectories. As can be seen in Movie 2 and schematically in Figure 5.3a, in this case particles move vertically away from the surface before even reaching the UME area. This behavior causes dip-like transient amperometric responses which are much smaller than the typical step-like decreases (Figure 5.3c). In addition to the effect of EOF on the signal size, it can also decrease the frequency of signals when particles are repelled from the surface to such an extent that they become invisibile in the current-time response. Hence, EOF may have both an ameliorative effect on particle transport by causing convection and a negative effect by causing some events to be undetectable (Figure 5.3a). Care must therefore be exerted in this case in particle concentration analysis.

A common limitation of blockade impact methods is that particle adsorption eventually saturates the UME surface and the UME as a transducing element cannot be used for a long-term measurements or continuous monitoring. Under no-salt conditions the particles do not land on the electrode (Figure 5.3c), but the resulting small fingerprints in the current-time response are not easily recognizable. This issue can be solved by functionalizing the metal and glass surfaces. Here, we employ a positively charged polyelectrolyte, poly-l-lysin (PLL), to optimize this approach for detecting cationic particles under different salt conditions. PLL can adsorb non-specifically on both metal and glass surfaces, neutralizing the glass and,

consequently, diminishing the EOF.[53,54] On the other hand, positively charged particles are electrostatically repelled from the PLL-coated UME when they come in close proximity to the electrode surface. These “kiss-and-run” events can cause blockade spikes in the current-time responses: as can be seen in Figure 5.3d, amidine-coated microparticles can be kept from remaining on the surface following collisions, leading to blockade spikes with an amplitude that is *ca*. 4 times that of the ambiguous spike-like events observed in the uncoated case. This simple electrode functionalization can increase the measurement time and introduce a method for detecting particles (for example plastic particles in drinking water) in a long-term measurement system with minimized electrode saturation by the target particles.

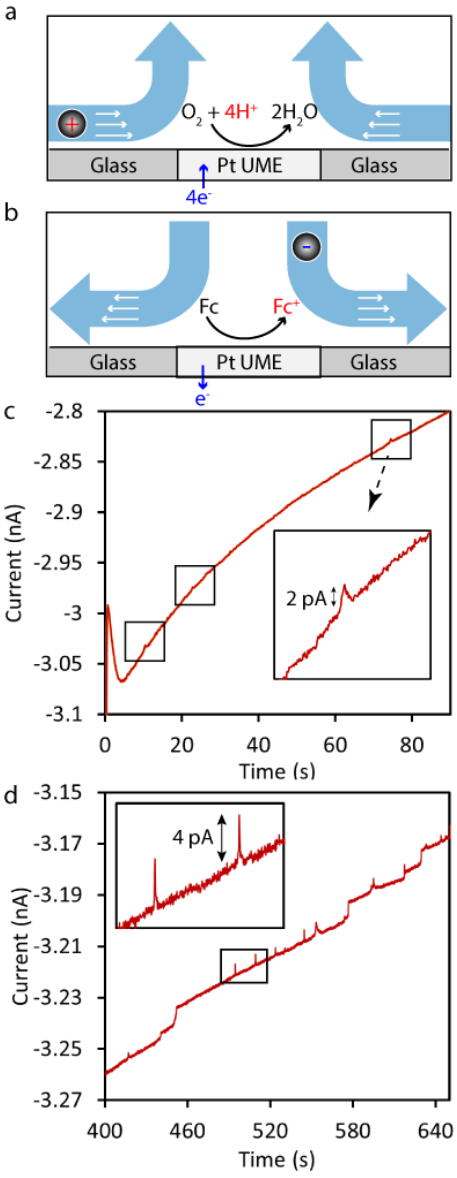

Figure 5.3. (a, b) Direction of self-induced convection and particle trajectories in reduction (a) and oxidation (b) reactions. (c) Transient amperometric responses upon collision of positively charged particles on a Pt UME surface when biased at negative potentials in 500x diluted PBS solution. (d) Detection of positively charged particles on a PLL-coated UME via ORR-driven blockade impact under no salt conditions.

5.3 Conclusions

In summary, our results demonstrate that dissolved oxygen in physiological solutions can serve as an efficient mediator in single-entity electrochemistry. The faster diffusion coefficient of O_2 in comparison to synthetic redox mediators, and the transfer of 4 electrons, yield limiting currents in the same range as most outer sphere mediators. In addition, due to the insensitivity of $\Delta I/I$ to the oxygen concentration, ORR-driven blockade impact can be used as a self-calibrating system for particle detection at different oxygen concentrations. We showed that this additive-free method can be employed for detecting cationic particles in water, and infer that it can be used for single-entity measurements in solutions such as cell culture media where addition of synthetic mediators is undesirable. As a disadvantage of this method, at low salt measurements the consumption of H^+ on the surface increases the local pH at the electrode interface, which is mitigated in a buffer. We anticipate that this method can also be used in the future for detecting particles inside the cell[56] as an *in-vivo* single-entity sensor.

5.4 Supporting information

5.4.1 Additional voltammograms

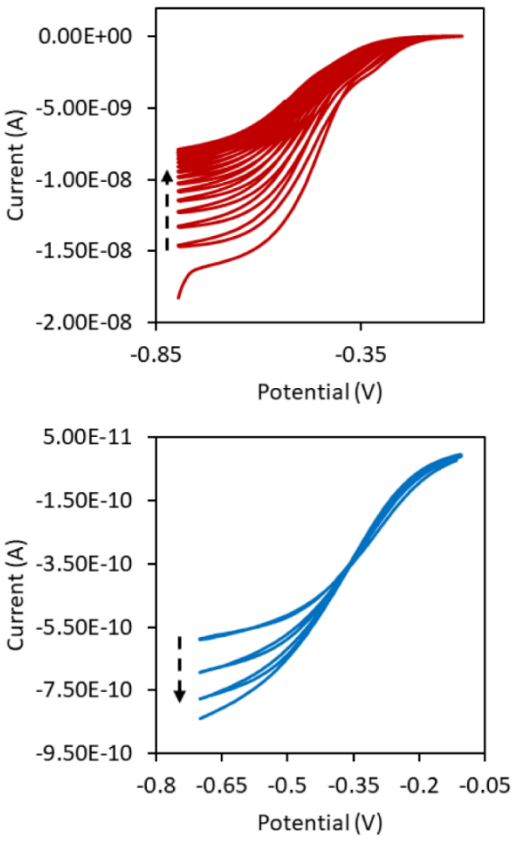

Figure 5.S1. Gradual recovery for the measurements in the open cells. Top panel: cyclic voltammogram measured at Pt disk UME vs Pt wire in a potential window from –0.7 to –0.1 and scan rate of 0.05 V/s O_2-saturated PBS. Starting from a saturated solution, a decrease in the limiting current level of the ORR with time can be observed when the electrochemical cell is exposed to air. The second wave in O_2-saturated PBS may be due to a shortage of H^+ at the electrode due to limited buffer capacity.[31] Bottom panel: measurements in a solution partially purged from oxygen by N_2 bubbling. An increase in the limiting current level of the ORR with time can be observed upon exposure to air (the initial increase from near-zero current was too rapid and is not resolved here).

5.4.2 Employing ORR in mediated faradaic impact in physiological solutions

To facilitate comparison with previously reported work,[31] here we show an example of detecting 50-nm Pt particles (locally synthesized[57]) on a carbon UME in an oxygen-saturated PBS solution. The measurement was performed using a carbon UME which is not an electroactive material for the ORR (Figure 5.S2). Figure 5.S3a schematically shows the mediated faradaic impact method. In mediated faradaic impact, collision of electroactive particles on an inert microelectrode biased at proper potential for the reaction leads to current amplification signals (spikes/steps). The steady-state current at an individual spherical nanoparticle on a planar electrode surface is given by $I = 4\pi(\ln 2)nFDCr$, where r is the radius of the nanoparticle.[29] Here, the signal size is proportional to the particle radius and concentration of the mediator in the solution. Hence, in comparison to the blockade impact, this method can lead to larger current signals in a comparable particle-to-electrode ratio and is favorable for detecting single nanoparticles using a UME.

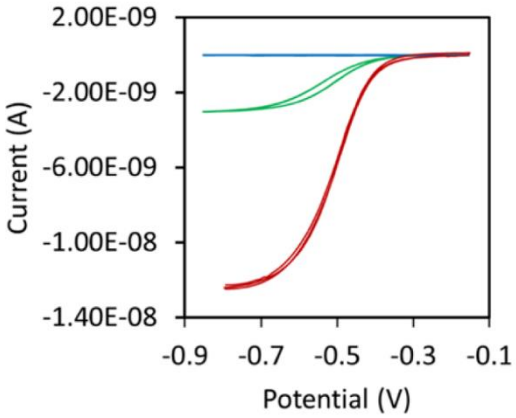

Figure 5.S2. Voltammogram of PBS solution on carbon UME (blue), Pt UME (green), and Pt UME after saturating the solution with O_2 (red), measured vs Pt wire at a scan rate of 0.05 V/s in.

Oxygen-saturated solutions were used for detecting 50-nm platinum particles. Figure 5.4b shows the current-time response of individual Pt nanoparticles impacting on the carbon UME surface biased at a potential of –0.7 V vs Pt wire pseudo-reference electrode in PBS buffer. The amplified signals show the ORR on Pt particles when particles collide on the carbon UME surface; different modes of transients can be observed.[31]

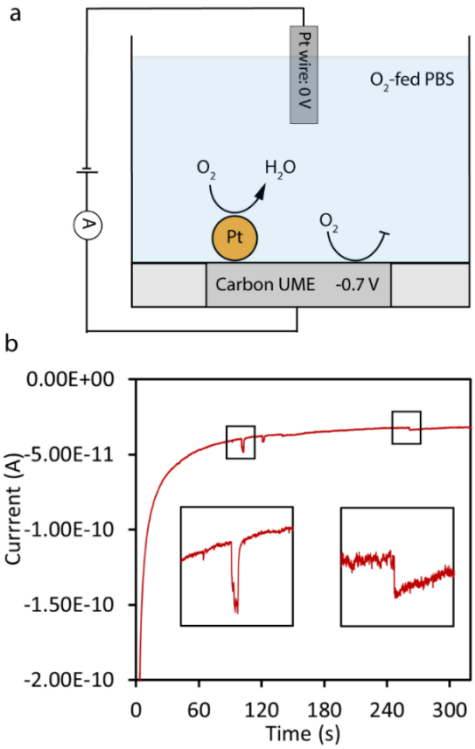

Figure 5.3. (a) Schematic representation of mediated faradaic impact electrochemical method. (b) Different modes of catalytic amplification signals upon transient and permanent collisions of 50-nm Pt nanoparticles on a carbon UME biased at -0.7 V vs pseudo reference Pt wire in oxygen-fed PBS solution.

5.5 References

(1) Shao, M.; Chang, Q.; Dodelet, J.-P.; Chenitz, R. Recent Advances in Electrocatalysts for Oxygen Reduction Reaction. *Chem. Rev.* **2016**, *116*, 3594-3657.
(2) Wang, J. Electrochemical Glucose Biosensors. *Chem. Rev.* **2008**, *108*, 814-825.
(3) Yoo, E.-H.; Lee, S.-Y. Glucose Biosensors: An Overview of Use in Clinical Practice. *Sensors* **2010**, *10*, 4558-4576.
(4) Cass, A. E. G.; Davis, G.; Francis, G. D.; Hill, H. A. O.; Aston, W. J.; Higgins, I. J.; Plotkin, E. V.; Scott, L. D. L.; Turner, A. P. F. Ferrocene-mediated enzyme electrode for amperometric determination of glucose. *Anal. Chem.* **1984**, *56*, 667-671.
(5) Frew, J. E.; Hill, H. A. O. Electrochemical Biosensors. *Anal. Chem.* **1987**, *59*, 933A-944A.
(6) Zhang, K.; Dong, H.; Dai, W.; Meng, X.; Lu, H.; Wu, T.; Zhang, X. Fabricating Pt/Sn–In2O3 Nanoflower with Advanced Oxygen Reduction Reaction Performance for High-Sensitivity MicroRNA Electrochemical Detection. *Anal. Chem.* **2017**, *89*, 648-655.

(7) Ge, X.-Y.; Feng, Y.-G.; Cen, S.-Y.; Wang, A.-J.; Mei, L.-P.; Luo, X.; Feng, J.-J. A label-free electrochemical immnunosensor based on signal magnification of oxygen reduction reaction catalyzed by uniform PtCo nanodendrites for highly sensitive detection of carbohydrate antigen 15-3. *Anal. Chim. Acta* **2021**, *1176*, 338750.
(8) Li, L.; Liu, X.; Yang, L.; Zhang, S.; Zheng, H.; Tang, Y.; Wong, D. K. Y. Amplified oxygen reduction signal at a Pt-Sn-modified TiO2 nanocomposite on an electrochemical aptasensor. *Biosens. Bioelectron.* **2019**, *142*, 111525.
(9) Fan, G.-C.; Gu, S.; Zhang, D.; Hu, Z.; Luo, X. Platinum-based nanocomposite as oxygen reduction catalyst for efficient signal amplification: Toward building of high-performance photocathodic immunoassay. *Biosens. Bioelectron.* **2020**, *168*, 112563.
(10) Wang, R.; Feng, J.-J.; Liu, W.-D.; Jiang, L.-Y.; Wang, A.-J. A novel label-free electrochemical immunosensor based on the enhanced catalytic currents of oxygen reduction by AuAg hollow nanocrystals for detecting carbohydrate antigen 199. *Biosens. Bioelectron.* **2017**, *96*, 152-158.
(11) Toyos-Rodríguez, C.; Adawy, A.; García-Alonso, F. J.; de la Escosura-Muñiz, A. Enhancing the electrocatalytic activity of palladium nanocluster tags by selective introduction of gold atoms: Application for a wound infection biomarker detection. *Biosens. Bioelectron.* **2022**, *200*, 113926.
(12) Wang, R.; Wang, A.-J.; Liu, W.-D.; Yuan, P.-X.; Xue, Y.; Luo, X.; Feng, J.-J. A novel label-free electrochemical immunosensor for ultra-sensitively detecting prostate specific antigen based on the enhanced catalytic currents of oxygen reduction catalyzed by core-shell Au@Pt nanocrystals. *Biosens. Bioelectron.* **2018**, *102*, 276-281.
(13) Zhang, J.; Xu, X.; Qiang, Y. Ultrasensitive electrochemical aptasensor for ochratoxin A detection using AgPt bimetallic nanoparticles decorated iron-porphyrinic metal-organic framework for signal amplification. *Sens. Actuators B Chem.* **2020**, *312*, 127964.
(14) Xia, N.; Liu, G.; Zhang, S.; Shang, Z.; Yang, Y.; Li, Y.; Liu, L. Oxidase-mimicking peptide-copper complexes and their applications in sandwich affinity biosensors. *Anal. Chim. Acta* **2022**, *1214*, 339965.
(15) Wang, A.-J.; Zhu, X.-Y.; Chen, Y.; Yuan, P.-X.; Luo, X.; Feng, J.-J. A label-free electrochemical immunosensor based on rhombic dodecahedral Cu3Pt nanoframes with advanced oxygen reduction performance for highly sensitive alpha-fetoprotein detection. *Sens. Actuators B Chem.* **2019**, *288*, 721-727.
(16) Malecka, K.; Ferapontova, E. E. Femtomolar Detection of Thrombin in Serum and Cerebrospinal Fluid via Direct Electrocatalysis of Oxygen Reduction by the Covalent G4-Hemin-Aptamer Complex. *ACS Appl. Mater. Interfaces* **2021**, *13*, 37979-37988.
(17) Zhou, Y.; Chai, Y.; Yuan, R. Highly Efficient Dual-Polar Electrochemiluminescence from Au25 Nanoclusters: The Next Generation of Multibiomarker Detection in a Single Step. *Anal. Chem.* **2019**, *91*, 14618-14623.
(18) Liao, H.; Jin, C.; Zhou, Y.; Chai, Y.; Yuan, R. Novel ABEI/Dissolved O2/Ag3BiO3 Nanocrystals ECL Ternary System with High Luminous Efficiency for Ultrasensitive Determination of MicroRNA. *Anal. Chem.* **2019**, *91*, 11447-11454.
(19) Zong, L.-P.; Li, J.; Shu, G.; Liu, X.; Marks, R. S.; Zhang, X.-J.; Cosnier, S.; Shan, D. Rational Design of a Highly Dispersed Fe–N–C Nanosheet with 1,10-Phenanthroline-2,9-Dicarboxylic Acid as a Preorganized Ligand: Boosted Electrochemiluminescence Detection of Tetracycline. *Anal. Chem.* **2022**, *94*, 1325-1332.
(20) Baker, L. A. Perspective and Prospectus on Single-Entity Electrochemistry. *J. Am. Chem. Soc.* **2018**, *140*, 15549-15559.

(21) Moazzenzade, T.; Huskens, J.; Lemay, S. G. Stochastic Electrochemistry at Ultralow Concentrations: the Case for Digital Sensors *Analyst* **2020**, *145*, 750-758.
(22) Quinn, B. M.; van 'tHof, P.; Lemay, S. G. Time-resolved electrochemical detection of discrete adsorption events. *J. Am. Chem. Soc.* **2004**, *126*, 8360.
(23) Xiao, X.; Bard, A. J. Observing single nanoparticle collisions at an ultramicroelectrode by electrocatalytic amplification. *J. Am. Chem. Soc.* **2007**, *129*, 9610-9612.
(24) Sokolov, S. V.; Eloul, S.; Kätelhön, E.; Batchelor-McAuley, C.; Compton, R. G. Electrode–particle impacts: a users guide. *Phys. Chem. Chem. Phys.* **2017**, *19*, 28-43.
(25) Dick, J. E.; Renault, C.; Bard, A. J. Observation of single-protein and DNA macromolecule collisions on ultramicroelectrodes. *J. Am. Chem. Soc.* **2015**, *137*, 8376-8379.
(26) Dick, J. E.; Hilterbrand, A. T.; Boika, A.; Upton, J. W.; Bard, A. J. Electrochemical detection of a single cytomegalovirus at an ultramicroelectrode and its antibody anchoring. *Proc. Natl. Acad. Sci. U. S. A.* **2015**, *112*, 5303-5308.
(27) Dick, J. E.; Hilterbrand, A. T.; Strawsine, L. M.; Upton, J. W.; Bard, A. J. Enzymatically enhanced collisions on ultramicroelectrodes for specific and rapid detection of individual viruses. *Proc. Natl. Acad. Sci. U. S. A.* **2016**, *113*, 6403-6408.
(28) Kwon, S. J.; Bard, A. J. DNA analysis by application of Pt nanoparticle electrochemical amplification with single label response. *J. Am. Chem. Soc.* **2012**, *134*, 10777-10779.
(29) Xiao, X.; Fan, F.-R. F.; Zhou, J.; Bard, A. J. Current Transients in Single Nanoparticle Collision Events. *J. Am. Chem. Soc.* **2008**, *130*, 16669-16677.
(30) Zhou, H.; Fan, F.-R. F.; Bard, A. J. Observation of Discrete Au Nanoparticle Collisions by Electrocatalytic Amplification Using Pt Ultramicroelectrode Surface Modification. *J. Phys. Chem. Lett.* **2010**, *1*, 2671-2674.
(31) Zhang, Y.; Robinson, D. A.; McKelvey, K.; Ren, H.; White, H. S.; Edwards, M. A. A High-Pressure System for Studying Oxygen Reduction During Pt Nanoparticle Collisions. *J. Electrochem. Soc.* **2020**, *167*, 166507.
(32) Li, P.; He, Q.; Liu, H.-X.; Liu, Y.; Su, J.-J.; Tian, N.; Zhan, D. Collision Incidents of Single Tetrahexahedral Platinum Nanocrystals Recorded by a Carbon Nanoelectrode. *ChemElectroChem* **2018**, *5*, 3068-3072.
(33) Xiang, Z.-P.; Tan, A.-D.; Fu, Z.-Y.; Piao, J.-H.; Liang, Z.-X. Oxygen reduction reaction on single Pt nanoparticle. *J. Energy Chem.* **2020**, *49*, 323-326.
(34) Stockmann, T. J.; Angelé, L.; Brasiliense, V.; Combellas, C.; Kanoufi, F. Platinum Nanoparticle Impacts at a Liquid|Liquid Interface. *Angew. Chem., Int. Ed. Engl.* **2017**, *56*, 13493-13497.
(35) Lu, Y.; Li, X.; Compton, R. G. Oxygen Reduction Reaction at Single Entity Multiwalled Carbon Nanotubes. *J. Phys. Chem. Lett.* **2022**, *13*, 3748-3753.
(36) Shimizu, K.; Sokolov, S. V.; Kätelhön, E.; Holter, J.; Young, N. P.; Compton, R. G. In situ Detection of Microplastics: Single Microparticle-electrode Impacts. *Electroanalysis* **2017**, *29*, 2200-2207.
(37) Eerkes-Medrano, D.; Leslie, H. A.; Quinn, B. Microplastics in drinking water: A review and assessment. *Curr Opin Environ Sci Health* **2019**, *7*, 69-75.
(38) Sun, X.-D.; Yuan, X.-Z.; Jia, Y.; Feng, L.-J.; Zhu, F.-P.; Dong, S.-S.; Liu, J.; Kong, X.; Tian, H.; Duan, J.-L.; et al. Differentially charged nanoplastics demonstrate distinct accumulation in Arabidopsis thaliana. *Nat. Nanotechnol.* **2020**, *15*, 755-760.
(39) Cole, M.; Coppock, R.; Lindeque, P. K.; Altin, D.; Reed, S.; Pond, D. W.; Sørensen, L.; Galloway, T. S.; Booth, A. M. Effects of Nylon Microplastic on Feeding, Lipid

Accumulation, and Moulting in a Coldwater Copepod. *Environ. Sci. Technol.* **2019**, *53*, 7075-7082.
(40) Zheng, X.; Liu, X.; Zhang, L.; Wang, Z.; Yuan, Y.; Li, J.; Li, Y.; Huang, H.; Cao, X.; Fan, Z. Toxicity mechanism of Nylon microplastics on Microcystis aeruginosa through three pathways: Photosynthesis, oxidative stress and energy metabolism. *J. Hazard. Mater.* **2022**, *426*, 128094.
(41) Feng, L.-J.; Li, J.-W.; Xu, E. G.; Sun, X.-D.; Zhu, F.-P.; Ding, Z.; Tian, H.; Dong, S.-S.; Xia, P.-F.; Yuan, X.-Z. Short-term exposure to positively charged polystyrene nanoparticles causes oxidative stress and membrane destruction in cyanobacteria. *Environ. Sci.: Nano* **2019**, *6*, 3072-3079.
(42) Leslie, H. A.; van Velzen, M. J. M.; Brandsma, S. H.; Vethaak, A. D.; Garcia-Vallejo, J. J.; Lamoree, M. H. Discovery and quantification of plastic particle pollution in human blood. *Environ. Int.* **2022**, *163*, 107199.
(43) Roshanzadeh, A.; Park, S.; Ganjbakhsh, S. E.; Park, J.; Lee, D.-H.; Lee, S.; Kim, E.-S. Surface Charge-Dependent Cytotoxicity of Plastic Nanoparticles in Alveolar Cells under Cyclic Stretches. *Nano Lett.* **2020**, *20*, 7168-7176.
(44) Yeager, E. Electrocatalysts for O2 reduction. *Electrochim. Acta* **1984**, *29*, 1527-1537.
(45) Cussler, E. L. *Diffusion: Mass Transfer in Fluid Systems*; Cambridge University Press, 1997.
(46) Kulkarni, A.; Siahrostami, S.; Patel, A.; Nørskov, J. K. Understanding Catalytic Activity Trends in the Oxygen Reduction Reaction. *Chem. Rev.* **2018**, *118* (5), 2302-2312.
(47) Moazzenzade, T.; Walstra, T.; Yang, X.; Huskens, J.; Lemay, S. G. Ring Ultramicroelectrodes for Current-Blockade Particle-Impact Electrochemistry. *Anal. Chem.* **2022**, *94*, 10168-10174.
(48) Deng, Z.; Elattar, R.; Maroun, F.; Renault, C. In Situ Measurement of the Size Distribution and Concentration of Insulating Particles by Electrochemical Collision on Hemispherical Ultramicroelectrodes. *Anal. Chem.* **2018**, *90*, 12923-12929.
(49) Boika, A.; Thorgaard, S. N.; Bard, A. J. Monitoring the Electrophoretic Migration and Adsorption of Single Insulating Nanoparticles at Ultramicroelectrodes. *J. Phys. Chem. B* **2013**, *117*, 4371-4380.
(50) Bonezzi, J.; Boika, A. Deciphering the Magnitude of Current Steps in Electrochemical Blocking Collision Experiments and Its Implications. *Electrochim. Acta* **2017**, *236*, 252-259.
(51) Lemay, S. G.; Moazzenzade, T. Single-Entity Electrochemistry for Digital Biosensing at Ultralow Concentrations. *Anal. Chem.* **2021**, *93*, 9023-9031.
(52) Weiß, L. J. K.; Music, E.; Rinklin, P.; Banzet, M.; Mayer, D.; Wolfrum, B. On-Chip Electrokinetic Micropumping for Nanoparticle Impact Electrochemistry. *Anal. Chem.* **2022**, *94*, 11600-11609.
(53) Moazzenzade, T.; Yang, X.; Walterbos, L.; Huskens, J.; Renault, C.; Lemay, S. G. Self-Induced Convection at Microelectrodes via Electroosmosis and Its Influence on Impact Electrochemistry. *J. Am. Chem. Soc.* **2020**, *142*, 17908-17912.
(54) Thorgaard, S. N.; Jenkins, S.; Tarach, A. R. Influence of Electroosmotic Flow on Stochastic Collisions at Ultramicroelectrodes. *Anal. Chem.* **2020**, *92*, 12663-12669.
(55) Fosdick, S. E.; Anderson, M. J.; Nettleton, E. G.; Crooks, R. M. Correlated Electrochemical and Optical Tracking of Discrete Collision Events. *J. Am. Chem. Soc.* **2013**, *135*, 5994-5997.

(56) Fu, A.; Yao, B.; Dong, T.; Chen, Y.; Yao, J.; Liu, Y.; Li, H.; Bai, H.; Liu, X.; Zhang, Y.; et al. Tumor-Resident Intracellular Microbiota Promotes Metastatic Colonization In Breast Cancer. *Cell* **2022**, *185*, 1356-1372.e1326.
(57) Tajerian, T.; Monsefi, M.; Rowan, A. Simple Chemistry Drives Controlled Synthesis Of Platinum Nanocrystal To Micron Size. *J Nanostructure Chem* **2019**, *9*, 197-202.

Designing a microparticle-based competitive displacement assay for the detection of ssDNA

Employing particles as a label is a common approach for signal amplification in various surface-based biosensors. However, due to the size-dependency of non-specific adhesive forces, employing microscale particles in collision-based methodologies like sandwich assays can increase the probability of non-specific interactions and consequently the occurrence of false-positive signals. In addition, due to the slow diffusion of microparticles, the particle concentration needs to be high enough to not become the limiting factor in real-time sandwich assays, which can exacerbate non-specific adsorption and false-positive signals. To circumvent this issue, here we introduce a microparticle-based competitive displacement assay for the detection of single-strand DNA (ssDNA). We implement toehold-mediated strand displacement as a dynamic actuator in the microparticle-substrate interface to dissociate specifically anchored particles from the surface upon displacement of target ssDNA. We employ quartz crystal microbalance with dissipation monitoring (QCM-D) to monitor DNA displacement, and a particle dissociation assay on poly(L-lysine) with appended oligo(ethylene glycol) (PLL-OEG$_4$) and hydroxy-terminated alkanethiol self-assembled monolayer (SAM)-coated surfaces. Although this assay intrinsically can diminish the false-positive signals during real-time measurements, non-specific adsorption of microparticles nonetheless occurs in the sensor preparation step, during which particles are bound to the surface. We observed that negatively charged particles cannot be fully dissociated from the PLL-OEG$_4$-coated surface by DNA displacement, which can be due to non-specific electrostatic adsorption. We show that suppressing the surface charge in a PLL-coated surface by an anionic passivant, polyacrylic acid (PAA), can improve the dissociation of the negatively charged microparticles upon DNA displacement. In parallel with the displacement assay, we show that the specificity of particle binding can be inferred from the comparing QCM-D harmonics in the particle binding step. We utilize the frequency of zero-crossing (f_{ZC}) in the coupled-resonator model to explain the particle binding specificity and the displacement efficiency for the different modified surfaces. Particles on a hydroxy-terminated SAM, and PLL/PAA-coated surfaces, which exhibit a smaller f_{ZC}, present an improved particle dissociation in comparison to the PLL-coated surface. This suggest that f_{ZC} can be used to characterize the nature of particle binding, in particular its specificity, on the modified surfaces.

Moazzenzade, T.; Lemay, S. G.; Huskens, J. Designing a microparticle-based competitive displacement assay for the detection of ssDNA (*Manuscript in preparation*).

6.1 Introduction

Micro and nanoparticles have shown remarkable promise as signal amplification labels in surface-based biosensors.[1,2] Various types of particles have been utilized for generating signals in electrochemical, optical, magnetic, and mass sensors.[3] In particular, particle-based mechanisms have been implemented in DNA biosensors where specific hybridization of DNA biomarkers generates signals *via* the proximity of DNA-coated particles to the surface.[4]

Despite improvements in the sensitivity, however, employing particles may undermine the specificity of biosensing by interfering with the biorecognition interaction and by increasing non-specific interactions.[5-8] Employing particles in sensing schemes can increase the probability of non-specific interactions because additional adhesive forces such as Van der Waals, hydrophobic, and electrostatic forces are exerted at the surface.[9] In addition, due to the size dependency of non-specific adhesion forces,[10-14] the conditions can become even worse when microscale particles are employed as the label.[14,15] For instance, in a sandwich assay where the proximity of probe-coated particles to the probe-coated surface generates a signal upon binding of the target,[4] employing microparticles as the label may increase non-specific binding and generate false-positive signals.[15,16] In addition, the slow diffusion of microparticles can be the limiting factor in real-time sandwich assays that require simultaneous binding of the partner probes. In such measurements, the concentration of the particle needs to be high enough to ensure simultaneous binding of the partners. This increases the probability of non-specific adsorption and consequently false-positive signals. Finally, although external forces can be used for decreasing the reaction time in collision-based microparticle assays, they can also increase non-specific adsorption.[17]

To sidestep the issues regarding the occurrence of false-positive signals upon non-specific interactions of microparticle collision in real-time measurements, we focus here on a target-induced microparticle displacement assay for the detection of single-strand DNA (ssDNA) oligonucleotides. The assay is based on toehold-mediated strand displacement:[18,19] microparticles bound to the surface by a dynamic double-strand DNA (dsDNA) actuator can be dissociated upon the displacement by a target ssDNA. Hence, this competitive assay starts with the microparticles anchored strongly to the surface, and only the specifically bound particles can be dissociated from the surface upon target DNA binding to generate a signal. Quartz crystal microbalance with dissipation monitoring (QCM-D) is used for analysing the surface modification, including particle binding and dissociation on different modified surfaces. In addition, we utilize the frequency of zero crossing (f_{ZC}), together with a coupled-resonator model,[20] to elucidate particle binding specificity as well as particle dissociation upon displacement by the target ssDNA. This assay requires methodologies for the improvement of antifouling properties of the surface and to suppress non-specific adhesive forces in the particle binding step to increase the population of specifically anchored particles on the surface. As a case study we employed modified poly(L-lysine) (PLL) polymers with appended oligo(ethylene glycol) (OEG_4) and methyl-tetrazine (Tz) moieties (PLL-OEG_4-

Tz)[21,22] and hydroxy-terminated alkanethiol self-assembled monolayer (SAM)-coated surfaces[23] We show how neutralizing the surface charge of the PLL-OEG_4-coated surface by adding a passivant, polyacrylic acid (PAA), can improve the efficiency of microparticle dissociation by DNA displacement. We also show the effect of increasing the density of dsDNA on the surface on particle binding specificity and dissociation efficiency. We believe this assay can provide new opportunities that employ microparticles as a signal amplification label for detecting biomolecules, strategies that mostly have been employed in immunoassays based on magnetic microparticles.[16] We further anticipate real-time single-entity electrochemical sensors based on methods such as blockade impact electrochemistry.[24] As a proof of concept we implement this assay for the detection of ssDNA *via* current-blockade impact electrochemistry.

6.2 Results and discussion

6.2.1 Design of a competitive DNA assay based on toehold-mediated strand displacement

The competitive displacement assay was designed for the detection of a model target DNA oligonucleotide with a length of 20 nt. The design is based on the concept of toehold-mediated strand displacement (TMSD).[18] In TMSD, the reaction starts with a single-strand invader (which will be the target DNA in the sensing scheme) and a primary duplex (incumbent/substrate) which possesses an overhanging single-strand domain in the substrate strand, the so-called "toehold". The invader, which is fully complementary to the substrate, hybridizes with the toehold site of the substrate in a first-order manner, so-called toehold hybridization, and displaces the single strand incumbent in an unbiased random walk process called branch migration.[18,25] Because the invader is fully complementary to the substrate, the reaction is thermodynamically driven forward and leads to the displacement of the single-strand incumbent.[18]

Figure 6.1 illustrates the DNA displacement assay. We employ a 5'-modified incumbent strand on the surface for the hybridization of the substrate strand (20 nt), which in turn functions as the probe sequence for the target DNA. This geometry results in a toehold site at the 5' end of the hybridized substrate which is available for starting the displacement of the incumbent by the invader (*i.e.*, the target). Due to the acceleration of the reaction kinetics with toehold length,[25,26] a sufficiently long domain (9 nucleotides) was adopted for the toehold site. This accelerates the toehold hybridization step and renders the overall reaction rate insensitive to this step.[18,25] In addition, the composition and length of the incumbent/substrate duplex (11 nucleotides) were designed using the OligoAnalyzer™ tool to possess the minimum possible hairpin and self-dimer structures on the surface in the case of high probe densities. The surface-immobilized incumbent strand (length: 11 nt) undergoes hybridization with the substrate strand (20 nt) to form a primary duplex (length: 11 bp)

together with a toehold sequence (length: 9 nt) at the 5' end (Figure 6.1a). The DNA displacement process (Figure 6.1b) starts with the toehold hybridization (step 1), which consists of hybridization of the invader with the accessible single-strand toehold. The branch migration proceeds in a random walk process (steps 2-4). Ultimately the invader displaces the incumbent and releases the secondary duplex (invader/substrate, length: 20 bp), leaving the immobilized incumbent strand on the surface (step 5).

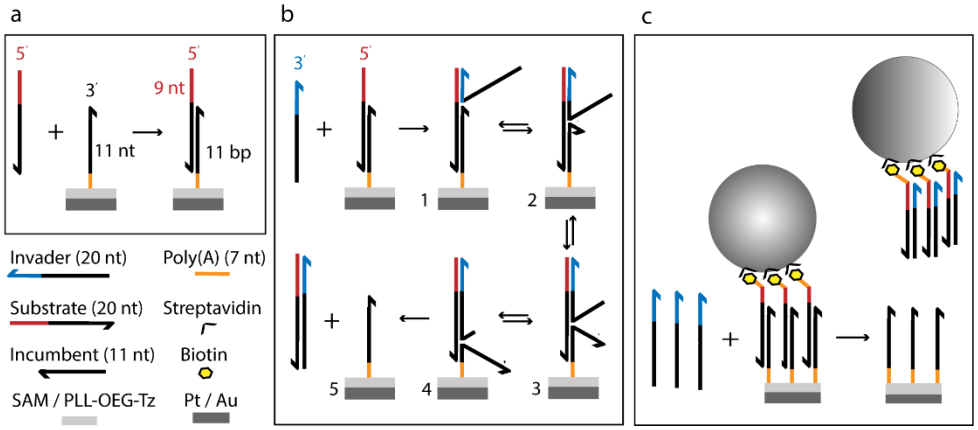

Figure 6.1. Surface-immobilized DNA displacement and particle dissociation assay. (a) Hybridization of the substrate strand on a surface with a pre-immobilized incumbent. The surface-immobilized incumbent strand can hybridize with the substrate strand to form a primary duplex with a single-strand toehold at the 5' end. (b) DNA displacement: the invader hybridizes with the toehold in the primary duplex and branch migration proceeds in a random walk process, eventually leading to the irreversible displacement of the immobilized incumbent. (c) Dissociation of the specifically anchored particles (800 nm), upon DNA displacement. Microparticles anchored to the DNA-coated surface through one or multiple strands dissociate upon displacement of the bound DNA strands.

QCM-D was employed for analyzing the displacement process using gold-coated QCM chips as sensors. QCM is a surface-sensitive real-time sensor in which deposition or desorption of a mass can affect the resonance frequency (Δf) of a driven oscillating piezoelectric crystal. In addition to the frequency shift (Δf), monitoring dissipation changes (ΔD) enables analysis of energy loss upon deposition of viscoelastic layers and microscale objects. Here, we employ multi-harmonic ΔD and Δf responses for analyzing DNA and particle displacement assays.

The incumbent strand need to be immobilized using a surface chemistry method that at the same time controls the probe density and the antifouling properties of the layer. PLL-OEG_4-Tz chemistry was used to fulfill these requirements.[21,22] Here, PLL-OEG_4-Tz with a high degree of OEG_4, 35%, was synthesized based on a previous report,[22] and used for immobilizing the incumbent DNA. In this approach, the polymer adsorbs electrostatically on the surface *via* its free amine groups, OEG_4 moieties play the role of antifouling agent, and

the functional groups (Tz) undergo reaction with *trans*-cyclooctyne (TCO)-modified incumbent DNA. Figure 6.2a shows schematic representations for the DNA immobilization, hybridization, and displacement on the PLL-OEG_4-Tz coated surface.

Figure 6.2b shows the QCM-D time traces recorded while coating the surface with PLL-OEG_4-Tz, followed by the DNA displacement assay. The negative frequency shift (step 1), reflects the mass change upon coating the QCM substrate with the PLL polymer, caused by electrostatic adsorption of the polymer onto the activated surface to form a rigid sub-nm layer.[21] The negligible dissipation change (ΔD) during the measurement confirms the small thickness and rigid nature of the adsorbed layer.[21] The PLL-coated surface was washed with PBS buffer to remove the loosely bound polymers from the surface (step 2), and then flushed with 1 µM incumbent TCO-DNA solution (step 3) for the immobilization of the TCO-modified incumbent strand. Because the dissipation change is small, we can quantify the deposited mass and the DNA density on the surface using the Sauerbrey equation; $\Delta m = -C\Delta f/n$. Here Δm is the adsorbed mass per unit area (in ng cm^{-2}), n is the overtone number, and C is the constant of value 17.7 ng cm^{-2} Hz^{-1} at f = 5 MHz for a AT cut QCM chip with a diameter of 14 mm.[28] Using this equation, the mass per unit area can be obtained as 177 ng/cm^2 for Δf = 10 Hz. Considering the hydration mass of ≈ 80 %, this value corresponds to the average density of ≈ 3.5 ssDNA molecules per $(10\ nm)^2$ on the surface for the incumbent DNA strand with a molecular weight of MW = 6150 g/mol.[22]

Step 4 shows the hybridization of the substrate strands, which leads to a negative frequency change together with a small, anticorrelated change in dissipation. Upon adding the invader strand, on the other hand, the frequency exhibits a positive shift and the anticorrelated dissipation change remains negligible, indicating a decreased mass upon DNA displacement (step 4). This process, as shown schematically in Figure 6.2a, releases the substrate/invader duplex to the solution and leads to an immobilized single-strand incumbent on the surface. When comparing Δf in the hybridization (step 3) and displacement (step 4) steps, it can be inferred that introducing the invader strand displaces the hybridized substrates completely. Hence, the complete restoration of Δf upon DNA displacement represents the dynamicity, reversibility, and accessibility of the designed DNA construct. In addition, although it might be expected that the positive charges of the free amine groups could cause non-specific binding of negatively charged (DNA) molecules, the complete restoration of Δf indicates the specificity of substrate binding of the PLL-modified surface and the ideal antifouling property of the PLL-OEG_4-Tz chemistry. Hence, the previously reported density of OEG_4 moieties[21] can properly prevent non-specific adsorption of biomolecules even when the receptor and target are highly negatively charged biomolecules such as DNA.

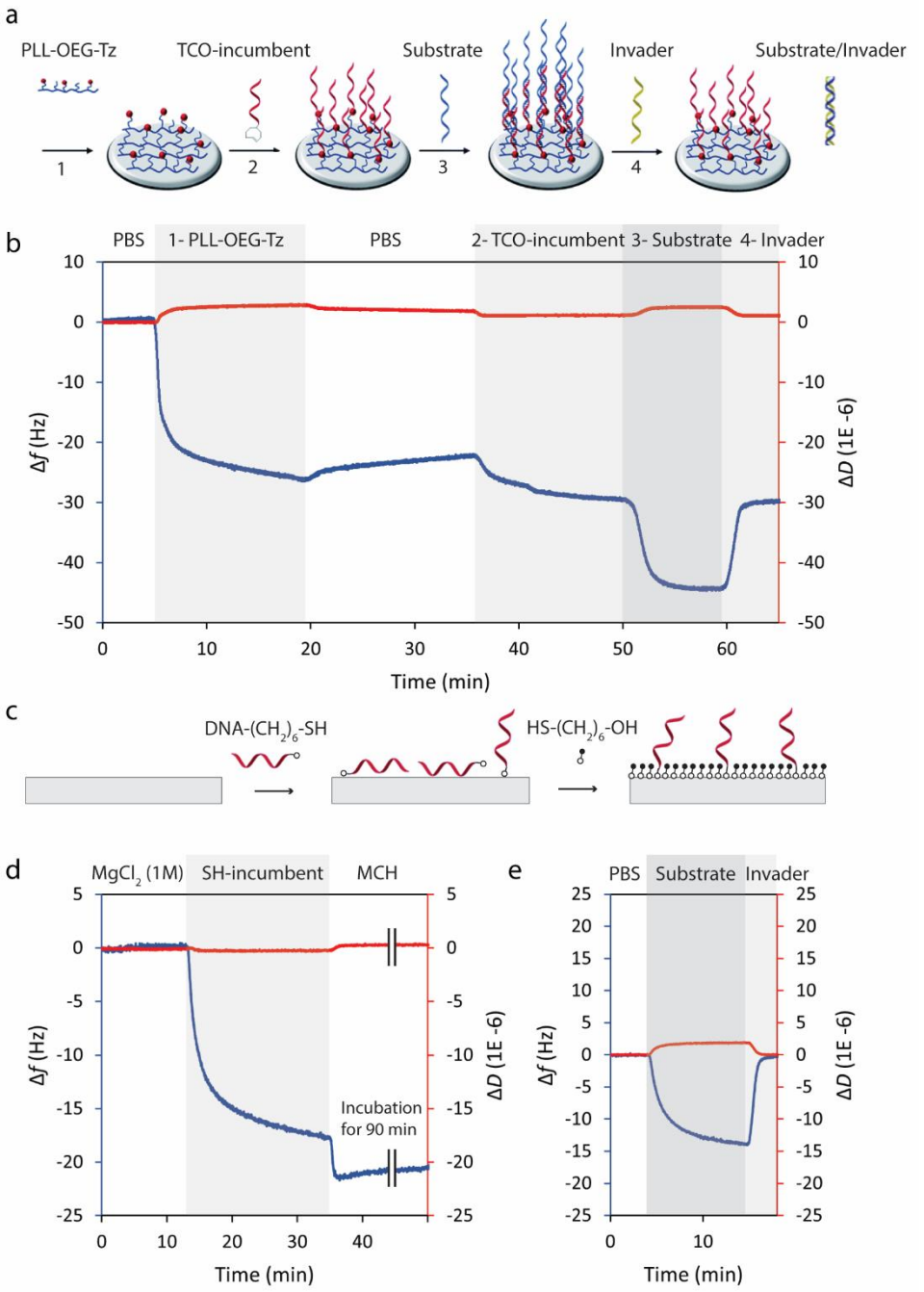

Figure 6.2. (a) Schematic representation of DNA immobilization, hybridization, and displacement on the PLL-OEG$_4$-Tz-coated surface. The scheme is adapted from ref. 20. (b)

Frequency and dissipation QCM-D time traces during coating of PLL-OEG_4-Tz (1), immobilization of the incumbent TCO-DNA (2), hybridization of the substrate ssDNA (3), and displacement of the incumbent strand upon addition of invader ssDNA strand (4). (c) Schematic representation of immobilizing the thiol-modified incumbent on a Au surface followed by backfilling the surface with a hydroxy-terminated thiol. The surface modification with thiol chemistry was performed in 1 M $MgCl_2$.[27] To compare with the PLL-coated surface, the DNA hybridization and displacement measurements were performed in PBS buffer. (d) Frequency and dissipation time traces of immobilizing thiol-DNA in 1 M $MgCl_2$ followed by coating the surface with hydroxy-terminated SAM. (e) Hybridization of the substrate ssDNA on the surface in d, and displacement of the incumbent strand upon addition of invader ssDNA strand in PBS solution. The frequency shifts for the fifth harmonic (Δf_5) are represented by the blue line and the dissipation changes (ΔD_5) by the red line. The DNA displacement measurements were performed in PBS buffer, pH 7.4, and the concentration of all DNA strands was 1 µM.

When comparing the hybridization and displacement steps in Figure 6.2b (steps 3 and 4, respectively), the steeper slope in the displacement step indicates that, for this actuator, the DNA displacement is faster than the DNA hybridization. This is even though the concentration of the substrate DNA (1 µM) is not the limiting factor in the hybridization step.[29] The faster displacement can be due to the fast hybridization of the toehold sequence at a high concentration of invader (1 µM), and the following fast branch migration of a short sequence (11 nt) which is a random walk process independent of the concentration. The displacement step is fast enough to prevent the appearance of a negative frequency shift during the toehold hybridization and branch migration steps (steps 1-4 in Figure 6.1), during which three DNA strands are anchored on the surface, and branch migration appears as a single step in QCM measurement (step 4 in Figure 6.2b).

The same assay was performed using thiol chemistry where 6-mercapto-hexanol (MCH) was used as the surface passivating agent for the immobilization of thiol-modified incumbent DNA to test the strand displacement process (Figure 6.2c, d, and e). As can be seen in Figure 6.2e. hybridization of the substrate strand and displacement of the incumbent in the hydroxy-terminated surface shows similar behaviour to the PLL chemistry, confirming the dynamicity of the actuator. The high similarity and the complete displacement show the applicability of both surface chemistries for this displacement assay.

6.2.2 Implementation of strand displacement in a particle dissociation assay

The particle competitive displacement assay (Figure 6.1c) was performed by employing the same DNA displacement construct between the particle and surface. In this assay, a biotin-labeled substrate DNA was used for the specific binding of streptavidin-coated polystyrene particles (SAv-PS, zeta potential −30 mV). With this architecture, specifically anchored particles on a layer of dsDNA bridges can be dissociated from the surface by adding the invader (target DNA) and displacing the incumbent (Figure 6.1c). Based on the density of

dsDNA on the surface, 4 dsDNA per $(10\ nm)^2$, and the contour length[30] of ≈ 3.5 nm for the 11 bp primary duplex, and also considering a high density of streptavidin proteins on the particle surface (1 protein per $(10\ nm)^2$), we estimate that about ≈ 90 dsDNA bridges can be considered between the particle and the surface (Figure 6.S1). However, the estimated number of contacts could be more because an immobilized streptavidin has a residual valency of two, and can bind to one or two available biotin-labeled dsDNA.[31,32] On the other hand, it is expected that not all available sites can bind simultaneously due to steric hindrances. Similar to the DNA displacement assay, this step is also expected to show complete restoration of Δf and ΔD after adding the invader DNA to a surface assuming an ideal antifouling property.

Figure 6.3 shows the particle displacement assay on different modified surfaces. Figure 6.3a shows the particle displacement assay on a PLL-OEG_4-Tz-coated surface. First, the incumbent-immobilized surface was hybridized with the substrate and then displaced by adding the invader to check the efficiency of the DNA actuator. After checking the dynamicity of the DNA actuator, the surface was hybridized again with the biotin-labeled substrate (biotin-subs) to create a layer of biotin-labeled dsDNA, and then flushed with the SAv-coated PS particle solution. A significant increase in the dissipation response, and marked variations in the frequency and dissipation responses for different harmonics, are characteristic for the deposition of microparticles on the surface. Addition of the invader strand led to dissociation of the specifically anchored particles from the surface. Although a considerable restoration in frequency shift was observed, the dissipation change remains almost unaffected upon invader addition. The positive frequency shift upon adding the invader can be explained as the consequence of mass decrease upon displacement of DNA strands in regions between the particles, and also dissociation of a small portion of particles that were specifically anchored. However, restoration in Δf can be misleading because the incomplete restoration of ΔD can be inferred as the continued presence of microparticles on the surface.

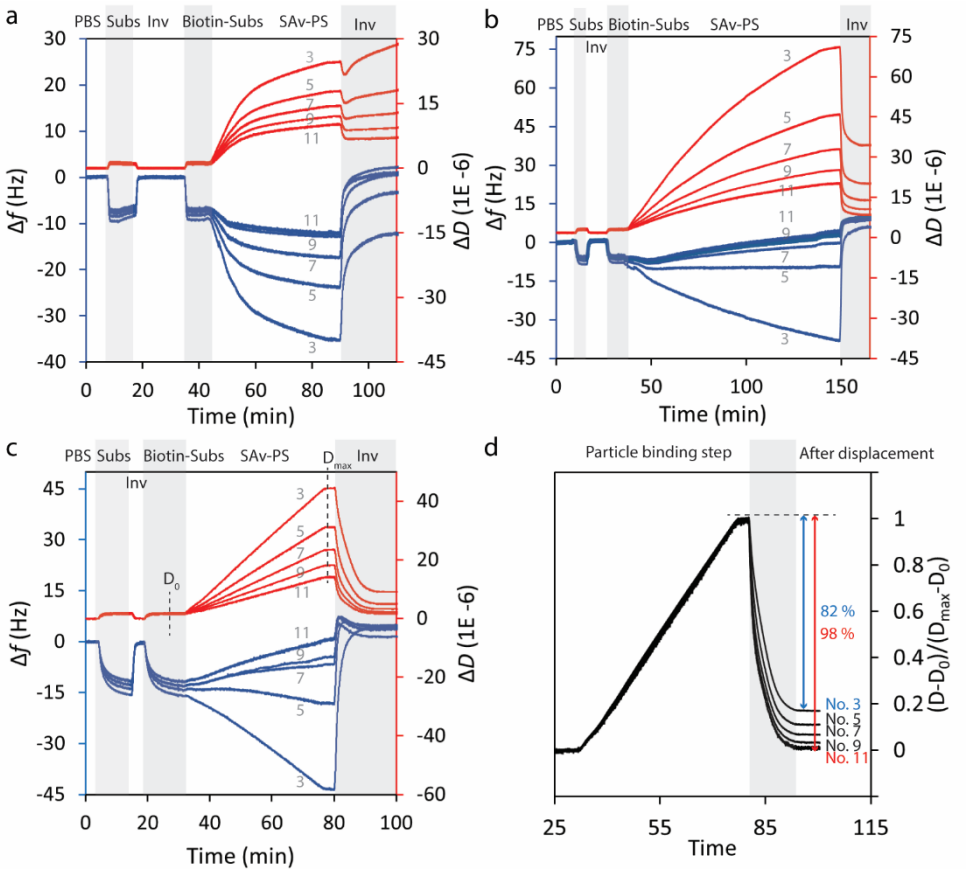

Figure 6.3. QCM-D monitoring of the particle dissociation by DNA displacement from surfaces coated with PLL (a), PLL/PAA (b), and thiol SAM (c). The particle displacement assay was performed after checking the dynamicity of the DNA actuator, as can be seen in the first and second steps of the QCM-D curves. Blue and red curves show the frequency and dissipation changes, respectively, and the integers represent the harmonic numbers. (d) The normalized dissipation responses $(D\text{-}D_0)/(D_{max}\text{-}D_0)$ for the SAM-coated surface (data from c).

The incomplete particle dissociation on the PLL-coated surface can be explained as the consequence of non-specific electrostatic adsorption of negatively charged particles on the surface that possesses an overall positive charge because of the free amine groups of the PLL. Although the antifouling property of the PLL-OEG_4 chemistry can be improved by increasing the degree of OEG_4 moieties in the structure of the polymer, there is a limitation to increasing the percentage of these antifouling agents in the structure of the polymer. A minimum degree of free amine groups (about 60 %) is required to guarantee stable adsorption of the polymer to the surface.[21] Hence, to evaluate the effects of electrostatic adsorption and also improve

the particle dissociation in PLL chemistry, a polyanionic polymer, poly(acrylic acid) (PAA), was used to suppress the surface charge of PLL.

Coating of the PAA polymer was performed after the TCO-DNA immobilization step to prevent the repulsive effect of PAA on the TCO and Tz reaction. Hence, the resulting surface presents a similar ssDNA and, consequently, biotin-labeled dsDNA density (Figure 6.S2). Figure 6.3b shows the frequency and dissipation time traces of the particle binding and dissociation assay on the PLL/PAA-coated surface. Similar to the PLL-coated surface, a significant increase in the dissipation response and increased spread frequency and dissipation responses indicate the deposition of microparticles on the surface. However both frequency and dissipation responses show a significantly better restoration than PLL-coated surface after adding the invader. This improved restoration in ΔD of individual harmonics can be explained as the result of the suppressed electrostatic force on the PAA-coated surface that can be due to the overall negative surface charge after PAA adsorption. Although suppressing the electrostatic force by PAA can improve the antifouling property of the surface and the particle dissociation, other adhesive forces like Van der Waals forces[14] may still play a role as another origin of non-specific binding of protein-coated microparticles on the PLL/PAA-coated surface (Figure 6.3b).

Performing the displacement assay on an MCH-coated surface showed an improved restoration in ΔD in different individual harmonics in comparison to the PLL and PLL/PAA surfaces (Figure 6.3d). This improved particle dissociation may be explained as the result of a different, possibly more upright,[23] presentation of the dsDNA on the hydroxy-terminated SAM-coated surface, which may facilitate particle dissociation upon DNA displacement.

6.2.3 Stiffness of contact; a signature of binding specificity?

As shown in Figures 3a, b, and c, the Δf in the particle displacement step can be misleading for analyzing the particle dissociation for differently modified surfaces. For the PLL-coated surface (without PAA adsorption), the dissipation signal remains almost unchanged after adding the invader, although the frequency change represents a very good restoration for some of the harmonics. For SAM and PLL-PAA-coated surfaces, Δf shows a restoration step that is larger than the original shift observed upon particle binding, while restoration of the related dissipation response remains incomplete. Evaluating the degree of particle dissociation using the ΔD restoration is not straightforward either. Although the restoration of ΔD in individual harmonics can give insight into the particle dissociation efficiency, normalizing the dissipation changes harmonics by $(D\text{-}D_0)/(D_{max}\text{-}D_0)$ shows different restoration values for different harmonics (Figure 6.3d). This can be seen in Figure 6.3d, where the normalized dissipation responses for the SAM-coated surface show apparent recoveries of 82% - 98% for different harmonics.

We employ the coupled-resonator model[20] to explain the particle behaviour in the binding and after the displacement steps and also explain the difficulties regarding the quantification of the dissociated particle fraction. Microparticles binding to the surface of an oscillator behave as coupled resonators.[20] In this model, the force constant between the microparticle and the oscillator affects the overall frequency response of the system. Strongly bound particles follow the inertial loading theory in which the deposited mass leads to a negative frequency response. In contrast, in a weaker particle-surface contact, the frequency change increases upon particle landing, so-called elastic loading.[33] The latter is a consequence of the microparticle's inertia, such that during oscillations the particle has insufficient time to respond and a restoring force is exerted on the quartz crystal.[34] Hence, depending on the stiffness of the contact and the mass of the particles, particle landing may cause positive or negative frequency shifts in a given harmonic when the microparticle lands on a rigid surface.[35] This model help explain particle binding and dissociation on differently modified surfaces. As can be seen in Figure 6.3a, b, and c, although the dissipation responses increase upon particle binding, dissimilar frequency responses appear for differently modified surfaces. Both positive (for large overtones) and negative (for lower overtones) frequency shifts can be observed in the frequency harmonics of the SAM and the PLL/PAA-coated surface during the particle binding steps, whereas the PLL-coated surface shows only negative shifts. The overall negative shifts in the frequency harmonics of the PLL-coated surface can be explained as the consequence of the strong binding of negatively charged particles on a positively charged, PLL-coated oscillator. By suppressing the electrostatic force in the PLL/PAA-coated surface, the particles become more free to vibrate with respect to the surface which leads to a positive shift in Δf. This is accompanied by a better restoration in ΔD during invader addition. Similar behaviour can be observed for the particle binding on the SAM-modified surface, which is in good agreement with the improved particle dissociation in the invader addition step (Figure 6.3c). It is important to consider that the density of dsDNA in the particle interface is almost similar for the modified surfaces (first steps in frequency responses in Figure 6.3a, b, and c).

The nature of particle binding can be shown by plotting the frequency shift *versus* overtone number (Figure 6.S3) to obtain the frequency of zero-crossing (f_{ZC}), *i.e.*, the frequency at which Δf changes sign from negative at $f < f_{ZC}$ to being positive at higher harmonics.[33] This quantity has been introduced to characterize the contact stiffness of microparticles on the oscillator surface in the coupled-resonator model.[33] This plot for different modified surfaces, as shown in Figure 6.4a, shows a monotonic relation with the particle dissociation efficiency. In the PLL/PAA-coated surface (red), the f_{ZC} appears at lower frequencies in comparison to the PLL-coated surface (blue). f_{ZC} in the SAM-coated surface (green) shows a smaller value in comparison to the PLL/PAA-coated surface, which is in good agreement with the improved particle dissociation from this surface. Hence, we can label the f_{ZC} as a parameter of binding specificity at a given density of receptors, because surfaces with smaller f_{ZC}, show improved particle dissociation. Hence, the relation between the f_{ZC} in the particle binding

step, and ΔD in the particle displacement step can be considered as a mutually consistent test for the specificity of particle binding on receptor-modified surfaces.

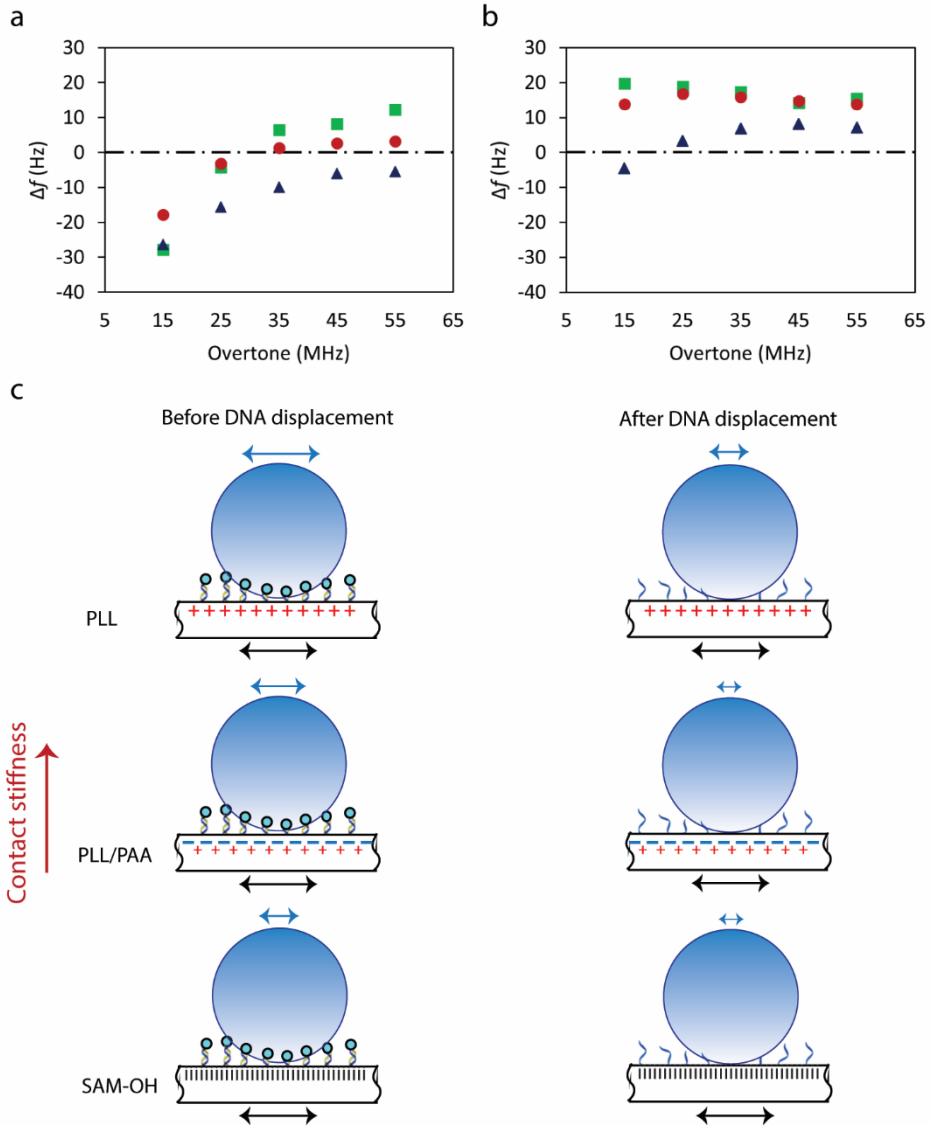

Figure 6.4. Frequency shifts *versus* harmonic numbers representing f_{ZC} in SAM-coated (■), PLL/PAA-coated (●), and PLL-coated (▲) surfaces, before (a) and after (b) adding the invader. The data points were extracted from the frequency harmonics, 45 min after flushing the surface with the particle solution where the surfaces with a similar density of biotin-labeled dsDNA receptors present similar dissipation changes. (c) Schematic representation of particle oscillation on the PLL, PLL/PAA, and hydroxy-terminated SAM-coated surfaces

before and after DNA displacement. Particles can bind to the surfaces in a multivalent manner. DNA displacement decreases the stiffness of contact between particles and the surface. This causes the particle motion to stop following the surface and exert a restoring force on the surface. Blue and black arrows show the relative magnitude of oscillation of a particle and the surface, respectively.

The same plot can be used to explain the behaviour of the non-specifically adsorbed particles after adding the invader (Figure 6.4b). Adding the invader strand and depleting the biotin-labeled dsDNA at the interface (also outside the particle contact area) can weaken the contact stiffness of non-specifically adsorbed particles, and the resonator may behave like a particle on the pristine surface.[34] This decreased stiffness can be seen in Figure 6.4b, and is illustrated schematically in Figure 6.4c. For the PLL-coated surface, non-specifically adsorbed particles (Figure 6.4b, blue) present lower contact stiffness (f_{ZC} has shifted toward lower frequencies)[34] in comparison to the condition before DNA displacement (Figure 6.4a, blue), which can be due to the effect of diminished multivalency. However, the PLL curves before and after the DNA displacement (Figures 4a, and b, blue curves), show similar behaviour, which may reflect a similar nature of particle binding due to the dominancy of electrostatic forces. PLL/PAA and SAM-coated surfaces show similar behaviour after adding the invader where the non-specifically adsorbed particles possess less stiffness. This phenomenon can be seen in the data points that are independent of the harmonic numbers and the small value of f_{ZC} that appears at such low frequencies that it cannot be observed with the current instrument (Figure 6.4b, red and green respectively). Hence, the non-specifically adsorbed particles on PLL/PAA and SAM surfaces are different from the PLL surface and may originate from other forces like Van der Waals, hydrophobic interactions, etc. Hence, analyzing the behaviour of particles after DNA displacement helps to reveal the nature of non-specific binding.

It can be inferred from the analysis above that particles show different behaviour before and after DNA displacement. Before DNA displacement, the f_{ZC} is the consequence of the oscillation of populations of specifically and non-specifically bonded particles anchored multivalently on the dsDNA-coated surface. However, after displacement, the f_{ZC} is determined solely by non-specifically adsorbed particles on the semi-pristine surface, and the effects of multivalency are diminished. Hence, implementing a model for the quantification of the fraction of the dissociated particles by ΔD restoration is not straightforward, because two inhomogeneous populations of particles (before and after DNA displacement) must be described simultaneously. This is further evidenced by noting that, in the coupled-resonator models,[33,34,36,37] f_{ZC} also corresponds to the maximum dissipation change. This cannot be observed in the particle binding steps in Figures 3a, b and c, which may result from the multivalent binding of the particles.

6.2.4 Effect of dsDNA density on particle displacement

As concluded from the calculation in Figure 6.S1, microparticles bind to the dsDNA-coated surface in a multivalent mode. However, this is not a favourable DNA density in a particle-based DNA sensor because multiple target DNAs are required to displace a specifically anchored particle from the surface. In particular, the ideal condition for a particle-based assay is a density where particles bind to the surface by one single dsDNA bridge to achieve DNA detection at a single-molecule level. On the other hand, although decreasing the density of dsDNA in the gap between the particle and surface seems to improve the concentration sensitivity and accelerate the particle displacement, it may increase the non-specific adsorption of negatively charged particles on the surface. As concluded from the PAA-coated surface experiment, inverting the surface charge can improve the dissociation of negatively charged particles. In addition, it appears that the presence of dsDNA on the SAM-coated surface can be a reason for the improved particle displacement. Hence, it should be possible to improve particle binding specificity by increasing the density of dsDNA with a neutral sequence that acts as an additional spacer. At higher densities of dsDNA, particles may get distanced more strongly from the surface, which can facilitate the dissociation in the displacement step. To analyze the effect of dsDNA density on particle displacement, a given PLL-OEG_4-Tz polymer was used for immobilizing the incumbent ssDNA with two different densities on the surface. To generate the surface with higher density, the PLL-coated surface was flushed with a 1 µM incumbent DNA solution (similar to the procedure in Figures 2 and 3), and for the lower density, a solution including 200 nM of the incumbent DNA, and 800 nM of a poly(A) ssDNA with the same length was used for the immobilization step. As shown in Figure 6.5a, the frequency responses in high and low-density samples show a similar negative shift when introducing TCO-DNA solution, indicating the equal functionalization for the TCO-DNA samples on PLL-OEG_4-Tz-coated surface with a given degree of Tz functional groups. After immobilizing TCO-DNA, the surfaces were coated with PAA and then hybridized with substrate DNA. As can be seen in the substrate hybridization steps, introducing the 1 µM biotin-labeled substrate strand shows a frequency shift Δf that is about 5 times bigger for the high-density surface, representing different densities of the incumbent strand and consequently biotin-labeled primary duplex on the surface.

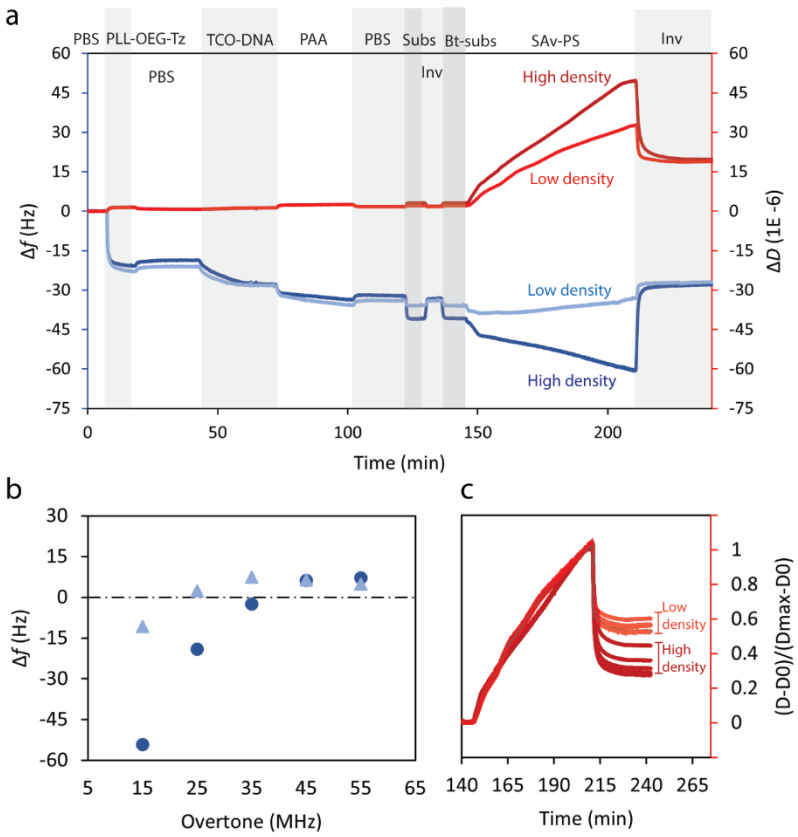

Figure 6.5. (a) Frequency and dissipation time traces of the particle displacement for different primary duplex densities (dark blue and dark red: high density, sky blue and red: low density). (b) Frequency shifts *versus* overtone numbers. f_{ZC} is lower for a lower probe density (sky blue). (c). Normalized dissipation responses $(D\text{-}D_0)/(D_{max}\text{-}D_0)$ in high and low-density incumbent-immobilized surfaces.

As can be seen in the particle displacement step, the surface with a higher density of the primary duplex shows an ameliorated particle displacement. This improved particle dissociation on the high-density surface can be due to the increased negative charge and also the increased gap between particle and surface due to the DNA adopting a more extended configuration at higher density of dsDNA. However, as can be seen in Figure 6.5b, the stiffness of the contact is increased at higher density leading to a bigger f_{ZC}. However, this data does not follow the monotonic relation of the smaller f_{ZC} and increased particle dissociation, as concluded from Figure 6.4. Hence, it should be considered that using f_{ZC} as a signature of binding specificity is valid only when the surfaces compared have an almost equal density of receptors. Because increasing the multivalency can increase the stiffness of contact, the f_{ZC} shifts toward higher frequencies.

6.3 Conclusions

An intrinsic advantage of employing TMSD in a DNA sensor is that nonspecific oligonucleotide strands cannot easily cause false positive signals. This is important because biofluids like urine contain oligonucleotides with different length and composition. These oligonucleotides can hybridize non-specifically with ssDNA receptors in a classic DNA sensor, especially when the measurement temperature (typically room temperature for surface biosensors) is much lower than the melting temperature (T_M) of a typical oligonucleotide marker. In comparison, in a TMSD-based sensor, sensing starts from a hybridized probe on the surface with a large portion of the receptor being protected as dsDNA. Hence, the biorecognition can proceed only when a given oligonucleotide in the sample is fully complementary with both the toehold and the primary duplex, so that it can accomplish the toehold hybridization and branch migration steps.

Here, we explored the use of TMSD as a dynamic actuator in the microparticle-substrate interface in a competitive displacement assay for the detection of ssDNA. The main motivation for designing this approach was to avoid false-positive signals during the real-time measurement in microparticle-based biosensors. In this method, specifically anchored particles dissociate only when the target ssDNA accomplishes the DNA displacement and lead to a measurable signal. However, this method requires proper surface chemistries to suppress the non-specific adsorption of particles in the particle binding step. Using QCM-D, we showed that, although PLL chemistry with a high degree of OEG_4 moieties shows an ideal antifouling property at the biomolecular level, non-specific adsorption of negatively charged microparticles can hamper particle dissociation upon DNA displacement. We showed that suppressing the electrostatic forces by an anionic passivant, PAA, can improve the particle dissociation on the PLL-coated surface. However, the results showed that other adhesive forces may play a role and hamper particle dissociation upon DNA displacement in PLL/PAA coated surface. The highest particle dissociation was observed for the hydroxy-terminated SAM-coated surface.

In parallel with the displacement assay, we employed the frequency of zero-crossing (f_{ZC}) to explain the nature of particle binding and validate the restoration of ΔD in the particle dissociation step on different modified surfaces. We observed that for a given density of dsDNA, surfaces with a smaller f_{ZC}, show an improved particle dissociation, leading to the hypothesis that f_{ZC} can be employed as a signature of binding specificity. Hence, the relation between f_{ZC} in the particle binding step and ΔD in the displacement step can be regarded as a *double-controlled* method for the specificity of particle binding on dsDNA-modified surfaces. Further measurements showed that increasing the density of dsDNA in the particle-substrate interface can improve the particle displacement efficiency. However, higher densities showed a positive shift in the f_{ZC} due to multivalency, which is not in agreement with the correlation between small f_{ZC} and high particle displacement reported above.

On the other hand, an increased multivalency guarantees the strong binding of particles on the surface before the specific binding of the target DNA, which can diminish spontaneous particle release by thermal activation and the appearance of false-positive signals during the real-time measurement. Hence, although multivalency showed an improvement in the particle displacement, and also intrinsically can sidestep the false-positive signals in particle displacement assay, it can decrease the sensitivity of the sensor because multiple target ssDNAs are required to displace a single microparticle. Hence, to achieve a microparticle-based biosensing at single-entity level, instead of increasing the number of contacts to improve the particle displacement, this assay needs to improve the antifouling property of surface modification methods to guarantee specific binding of microparticles with a single dsDNA bridge. On the other hand, the length of the primary duplex needs to be increased to reach a lower dissociation rate (k_d) and guarantee the long-lasting binding of particles on the surface with only one ssDNA bridge.

As a proof of concept, we implemented this displacement assay for the detection of ssDNA targets in blockade impact electrochemistry (Figure 6.S4). However, due to the multivalent binding of the particles, this biosensor is still far from being a single-entity DNA biosensor.[38] Decreasing the density of dsDNA, employing smaller particles, and boosting the sensitivity of the readout, we anticipate that it is possible to reach a single-entity DNA sensor. Although this competitive displacement assay has been designed for detecting a ssDNA, the methodology can be extended for any receptor/target binding architecture where a specifically interacted microparticle can be dissociated by specific binding of a target molecule with higher affinity.

6.4 Supporting information

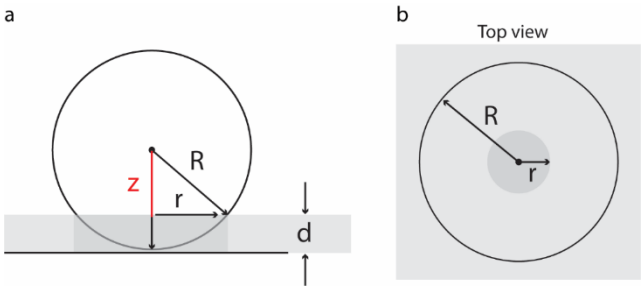

Figure 6.S1. (a) and (b), Schematic representations of the contact area between the SAv-PS with a diameter of 400 nm and the dsDNA-coated surface. The contour length (d) of the B-DNA[30] for the primary duplex (11 bp) is considered ≈ 3.5 nm. Hence, the diameter (r) of the contact area between the particle and the dsDNA brush can be calculated by

$$z = R - d(R - d)^2 + r^2 = R^2$$

$$\Longrightarrow r = \sqrt{d\,(2R - d)}$$

$$r \approx \sqrt{2dR} \text{ when } d << R$$

$$r \approx \sqrt{2 \times 3.5 \times 400} \approx 53 \text{ nm}$$

The contact area between the particle and the surface (dark grey) can be obtained by $A = \pi r^2 \approx 8800$ nm^2

Considering the ideal stickiness of the surface due to a high density of Biotin-dsDNA, ≈ 4 dsDNA per (10 nm)^2 obtained from the Sauerbrey equation (Figure 6.2b, step 3), and the average density of 1 streptavidin per (10 nm)^2 on the particle surface, the number of contacts by dsDNA between the surface and a microparticle is ≈ 88. However, this is a very rough estimate. The average number of contacts can be more because an immobilized streptavidin can bind to maximum two biotin-labeled dsDNA. Steric hinderance can however prevent every possible pair from binding, reducing the number of bonds.

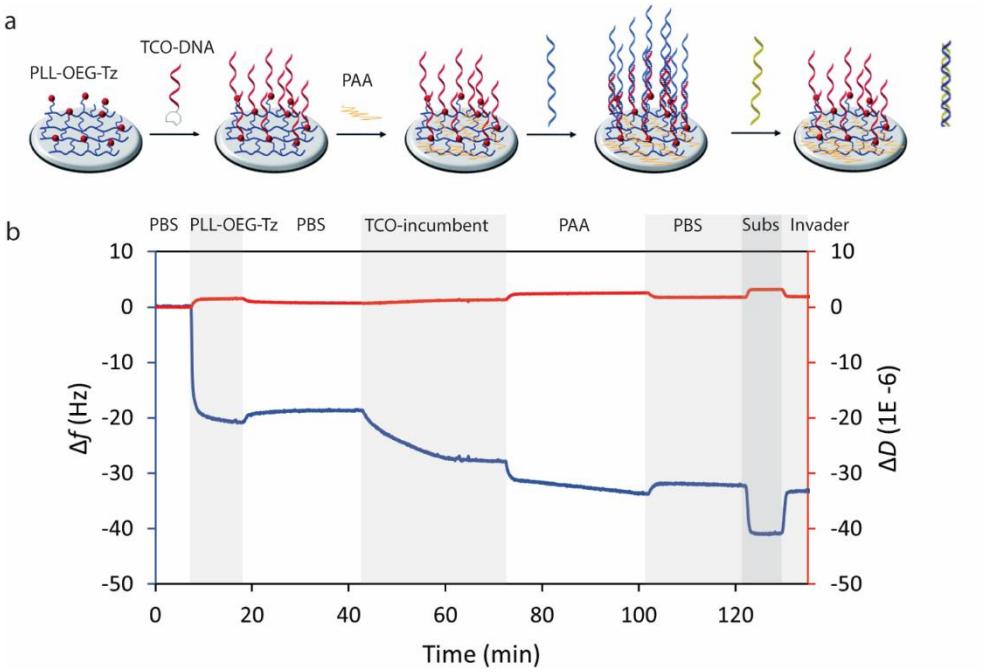

Figure 6.S2. Schematic representation (a), and the QCM-D time traces (b) for the coating of PAA on a PLL-coated surface. Coating of the PAA polymer was performed after the TCO-DNA immobilization step to prevent the repulsive effect of PAA on the TCO and Tz reaction. The scheme is adapted from ref. 20.

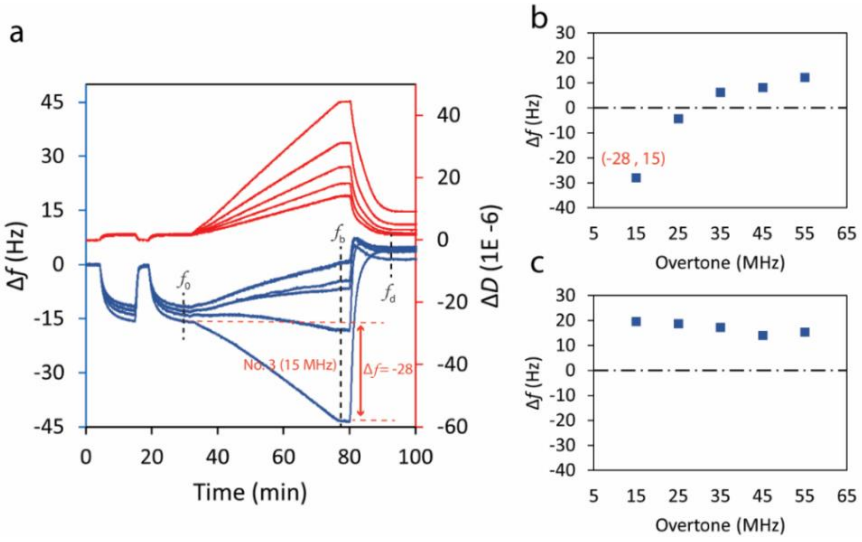

Figure 6.S3. Extracting f_{zc} from multi-harmonic QCM-D measurements. (a) Measurement over the course of the particle displacement assay. Δf versus harmonics following the particle binding step (b), and after DNA displacement (c).

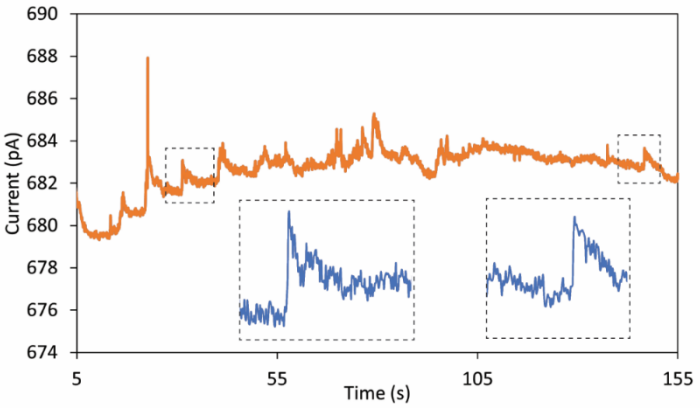

Figure 6.S4. Microparticle dissociation from the SAM-coated UME surface upon DNA displacement in blockade impact electrochemistry. The displacement of individual particles can be observed as discrete step-like increases in the current-time response.

6.5 Materials and methods

Phosphate-buffered saline tablets (PBS, pH 7.4), poly-L-lysine–HBr (PLL–HBr) (15–30 kDa), and 6-mercapto-1 hexanol were purchased from Sigma Aldrich, and methyltetrazine-OEG_4-NHS was purchased from Click Chemistry Tools, and used without further purification. Streptavidin-coated particles (0.8 µm) were purchased from Thermo-Fisher Scientific (11824992). Incumbent TCO-DNA (5′-TCO-PEG_4-AAAAAAATGTGTTGATGT -3′) and the density control TCO-incumbent strand (5′-TCO-PEG_4-AAAAAAAAAAAAAAAAA-3′) were obtained from Biomers. Thiol-modified incumbent DNA (5′-SH-C_6-AAAAAAATGTGTTGATGT-3′), the unmodified substrate strand (5′-CTTCCACTCACATCAACACA-3′), biotin-labeled substrate (5′-TEG-AAAAACTTCCACTCACATCAACACA -3′) and target DNA (5′-TGTGTTGATGTGAGTGGAAG-3′) sequences were purchased from Eurofins Genomic. Au and Pt QCM chips (AT cut, 5 MHz, 14 mm diameter) were purchased from Biolin Scientific. Milli-Q water with a resistivity >18 MΩ cm was used in all experiments. PLL–OEG_4–Tz with a high degree of OEG_4 was synthesized and characterized based on previously reported works.[21,22] QCM-D measurements were performed with a Q-Sense E4 instrument with a peristaltic pump (Biolin Scientific). All experiments were performed in PBS buffer (pH 7.4), using a flow rate of 80 µL min^{-1}. UV-ozone-treated platinum and gold substrates

were used for surface functionalization. The adsorbed mass per unit area (Δm) was calculated using the Sauerbrey model when calculating the density of dsDNA on the surface.

6.6 References

(1) Weizmann, Y.; Patolsky, F.; Willner, I. Amplified Detection Of DNA And Analysis Of Single-Base Mismatches By The Catalyzed Deposition Of Gold On Au-Nanoparticles. *Analyst* **2001**, *126*, 1502-1504.
(2) Fritzsche, W.; Taton, T. A. Metal Nanoparticles As Labels For Heterogeneous, Chip-Based DNA Detection. *Nanotechnology* **2003**, *14*, R63.
(3) Saha, K.; Agasti, S. S.; Kim, C.; Li, X.; Rotello, V. M. Gold Nanoparticles in Chemical and Biological Sensing. *Chem. Rev.* **2012**, *112*, 2739-2779.
(4) Shen, J.; Li, Y.; Gu, H.; Xia, F.; Zuo, X. Recent Development of Sandwich Assay Based on the Nanobiotechnologies for Proteins, Nucleic Acids, Small Molecules, and Ions. *Chem. Rev.* **2014**, *114*, 7631-7677.
(5) Lichtenberg, J. Y.; Ling, Y.; Kim, S. Non-Specific Adsorption Reduction Methods in Biosensing. *Sensors* **2019**, *19*, 2488.
(6) Frutiger, A.; Tanno, A.; Hwu, S.; Tiefenauer, R. F.; Vörös, J.; Nakatsuka, N. Nonspecific Binding—Fundamental Concepts and Consequences for Biosensing Applications. *Chem. Rev.* **2021**, *121*, 8095-8160.
(7) D'Agata, R.; Bellassai, N.; Jungbluth, V.; Spoto, G. Recent Advances in Antifouling Materials for Surface Plasmon Resonance Biosensing in Clinical Diagnostics and Food Safety. *Polymers (Basel)* **2021**, *13*. From NLM.
(8) Campuzano, S.; Pedrero, M.; Yáñez-Sedeño, P.; Pingarrón, J. M. Antifouling (Bio)materials for Electrochemical (Bio)sensing. *Int J Mol Sci* **2019**, *20*. From NLM.
(9) Reimhult, E.; Höök, F. Design of Surface Modifications for Nanoscale Sensor Applications. *Sensors* **2015**, *15*, 1635-1675.
(10) Lundgren, A.; Agnarsson, B.; Zirbs, R.; Zhdanov, V. P.; Reimhult, E.; Höök, F. Nonspecific Colloidal-Type Interaction Explains Size-Dependent Specific Binding of Membrane-Targeted Nanoparticles. *ACS Nano* **2016**, *10*, 9974-9982.
(11) Petean, P. G. C.; Aguiar, M. L. Determining The Adhesion Force Between Particles And Rough Surfaces. *Powder Technol.* **2015**, *274*, 67-76.
(12) Ermis, E.; Farnish, R. J.; Berry, R. J.; Bradley, M. S. A. Centrifugal Tester Versus A Novel Design To Measure Particle Adhesion Strength And Investigation Of Effect Of Physical Characteristics (Size, Shape, Density) Of Food Particles On Food Surfaces. *J. Food Eng.* **2011**, *104*, 518-524.
(13) Lam, K. K.; Newton, J. M. Influence Of Particle Size On The Adhesion Behaviour Of Powders, After Application Of An Initial Press-On Force. *Powder Technol.* **1992**, *73*, 117-125.
(14) Kemper, M. Non-Specific Protein-Surface Interactions In The Context Of Particle Based Biosensors. 2013.
(15) Buskermolen, A. D.; Lin, Y.-T.; van Smeden, L.; van Haaften, R. B.; Yan, J.; Sergelen, K.; de Jong, A. M.; Prins, M. W. J. Continuous Biomarker Monitoring With Single Molecule Resolution By Measuring Free Particle Motion. *Nat. Commun.* **2022**, *13*, 6052.

(16) De Palma, R.; Reekmans, G.; Laureyn, W.; Borghs, G.; Maes, G. The Optimization of Magnetosandwich Assays for the Sensitive and Specific Detection of Proteins in Serum. *Anal. Chem.* **2007**, *79*, 7540-7548.
(17) Luxton, R.; Badesha, J.; Kiely, J.; Hawkins, P. Use of External Magnetic Fields To Reduce Reaction Times in an Immunoassay Using Micrometer-Sized Paramagnetic Particles as Labels (Magnetoimmunoassay). *Anal. Chem.* **2004**, *76*, 1715-1719.
(18) Srinivas, N.; Ouldridge, T. E.; Šulc, P.; Schaeffer, J. M.; Yurke, B.; Louis, A. A.; Doye, J. P. K.; Winfree, E. On The Biophysics And Kinetics Of Toehold-Mediated DNA Strand Displacement. *Nucleic Acids Res.* **2013**, *41*, 10641-10658.
(19) Simmel, F. C.; Yurke, B.; Singh, H. R. Principles and Applications of Nucleic Acid Strand Displacement Reactions. *Chem. Rev.* **2019**, *119*, 6326-6369.
(20) Dybwad, G. L. A Sensitive New Method For The Determination Of Adhesive Bonding Between A Particle And A Substrate. *J. Appl. Phys.* **1985**, *58*, 2789-2790.
(21) Movilli, J.; Rozzi, A.; Ricciardi, R.; Corradini, R.; Huskens, J. Control of Probe Density at DNA Biosensor Surfaces Using Poly(l-lysine) with Appended Reactive Groups. *Bioconjug. Chem.* **2018**, *29*, 4110-4118.
(22) Di Iorio, D.; Marti, A.; Koeman, S.; Huskens, J. Clickable Poly-L-Lysine For The Formation Of Biorecognition Surfaces. *RSC Adv.* **2019**, *9*, 35608-35613.
(23) Levicky, R.; Herne, T. M.; Tarlov, M. J.; Satija, S. K. Using Self-Assembly To Control the Structure of DNA Monolayers on Gold: A Neutron Reflectivity Study. *J. Am. Chem. Soc.* **1998**, *120*, 9787-9792.
(24) Quinn, B. M.; van't Hof, P. G.; Lemay, S. G. Time-Resolved Electrochemical Detection Of Discrete Adsorption Events. *J. Am. Chem. Soc.* **2004**, *126*, 8360-8361.
(25) Zhang, D. Y.; Winfree, E. Control of DNA Strand Displacement Kinetics Using Toehold Exchange. *J. Am. Chem. Soc.* **2009**, *131*, 17303-17314.
(26) Yurke, B.; Mills, A. P. Using DNA to Power Nanostructures. *Genet. Program. Evolvable Mach.* **2003**, *4*, 111-122.
(27) Gong, P.; Levicky, R. DNA Surface Hybridization Regimes. *Proc. Natl. Acad. Sci. U.S.A.* **2008**, *105*, 5301-5306.
(28) Sauerbrey, G. Verwendung von Schwingquarzen zur Wägung dünner Schichten und zur Mikrowägung. *Z. Phys.* **1959**, *155*, 206-222.
(29) Dunn, K. E.; Trefzer, M. A.; Johnson, S.; Tyrrell, A. M. Investigating the dynamics of surface-immobilized DNA nanomachines. *Sci. Rep.* **2016**, *6*, 29581.
(30) Manning, G. S. The Persistence Length Of DNA Is Reached From The Persistence Length Of Its Null Isomer Through An Internal Electrostatic Stretching Force. *Biophys J* **2006**, *91*, 3607-3616.
(31) Dubacheva, G. V.; Araya-Callis, C.; Geert Volbeda, A.; Fairhead, M.; Codée, J.; Howarth, M.; Richter, R. P. Controlling Multivalent Binding through Surface Chemistry: Model Study on Streptavidin. *J. Am. Chem. Soc.* **2017**, *139*, 4157-4167.
(32) Hamming, P. H. E.; Huskens, J. Streptavidin Coverage on Biotinylated Surfaces. *ACS Appl. Mater. Interfaces* **2021**, *13*, 58114-58123.
(33) Olsson, A. L. J.; van der Mei, H. C.; Johannsmann, D.; Busscher, H. J.; Sharma, P. K. Probing Colloid–Substratum Contact Stiffness by Acoustic Sensing in a Liquid Phase. *Anal. Chem.* **2012**, *84*, 4504-4512.
(34) Johannsmann, D. Towards Vibrational Spectroscopy On Surface-Attached Colloids Performed With A Quartz Crystal Microbalance. *Sens. Bio-Sens. Res.* **2016**, *11*, 86-93.

(35) Pomorska, A.; Shchukin, D.; Hammond, R.; Cooper, M. A.; Grundmeier, G.; Johannsmann, D. Positive Frequency Shifts Observed Upon Adsorbing Micron-Sized Solid Objects to a Quartz Crystal Microbalance from the Liquid Phase. *Anal. Chem.* **2010**, *82*, 2237-2242.
(36) Tarnapolsky, A.; Freger, V. Modeling QCM-D Response to Deposition and Attachment of Microparticles and Living Cells. *Anal. Chem.* **2018**, *90*, 13960-13968.
(37) van der Westen, R.; Sharma, P. K.; De Raedt, H.; Vermue, I.; van der Mei, H. C.; Busscher, H. J. Elastic And Viscous Bond Components In The Adhesion Of Colloidal Particles And Fibrillated Streptococci To Qcm-D Crystal Surfaces With Different Hydrophobicities Using Kelvin–Voigt And Maxwell Models. *Phys. Chem. Chem. Phys.* **2017**, *19*, 25391-25400.
(38) Baker, L. A. Perspective and Prospectus on Single-Entity Electrochemistry. *J. Am. Chem. Soc.* **2018**, *140*, 15549-15559.

Single-entity electrochemistry for digital biosensing at ultralow concentrations

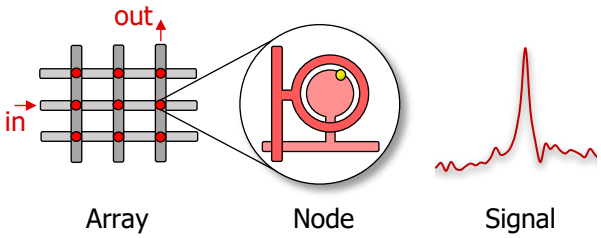

Quantifying ultralow analyte concentrations is a continuing challenge in the analytical sciences in general and in electrochemistry in particular. Typical hurdles for affinity sensors at low concentrations include achieving sufficiently efficient mass transport of the analyte, dealing with slow reaction kinetics, and detecting a small transducer signal against a background signal that itself fluctuates slowly in time. Recent decades have seen the advent of methods capable of detecting single analytes ranging from the nanoscale to individual molecules, representing the ultimate mass sensitivity to these analytes. However, single-entity detection does not automatically translate into a superior concentration sensitivity. This is largely because electrochemical transducers capable of such detection are themselves miniaturized, exacerbating mass transport and binding kinetic limitations. In this chapter we discuss how these challenges can be tackled through so-called digital sensing: large arrays of separately addressable single-entity detectors that provide real-time information on individual binding events. We discuss the advantages of this approach and the barriers to its implementation.

The contents of this chapter are adapted from: Lemay, S. G.; Moazzenzade, T. Single-Entity Electrochemistry for Digital Biosensing at Ultralow Concentrations. *Anal. Chem.* **2021**, *93*, 9023-9031.

7.1 Introduction

A salient theme in analytical science in recent decades has been the miniaturization of detection methods. Driven by the nanotechnology revolution, an important end point of this process has been the development of methods capable of detecting and interrogating individual microscopic entities ranging from inorganic and biological nanoparticles to single molecules. These methodological developments have opened new windows into the microscopic world and enabled fundamental and exploratory studies at the molecular scale in practically all areas of the physical sciences.

Electrochemistry is no exception to this trend. Conventional methods such as voltammetry and amperometry are in principle straightforward to scale down, even to the nanoscale, by decreasing the size of the electrodes employed. Interestingly, the detection of individual target particles or molecules can become possible when the size of the working electrode(s) approaches that of the targets. This has led to the development of so-called single-entity electrochemistry (SEE), as recently expounded by Baker.[1]

The best-known example of a SEE analytical method is the classic Coulter counter, in which modulation of the ionic conduction through an aperture is utilized to count and size particles.[2] This concept has been scaled down to molecular scale in both solid-state[3,4] and biological[5] nanopores, the latter having become so sophisticated as to permit the sequencing of nucleic acids.[6-9] Other examples of nanoscale SEE approaches include nanoelectrode-based studies for single-cell studies,[10] electrogeneration of surface nanobubbles,[11] single-ion-channel patch clamp recordings,[12,13] scanning-probe methods ranging from electrochemical scanning tunneling microscopy[14,15] to scanning electrochemical cell microscopy (SECCM),[16-18] single-molecule redox cycling,[19,20] and various forms of particle-impact electrochemistry.[21-24]

Typical SEE signals have a different character from that of conventional electrochemical data. Because individual single-entity events occur at random intervals, data typically consist of a mixture of quiescent periods in which very little happens, punctuated by sudden jumps or spikes in the signal corresponding to the detection of the analyte. This phenomenology is illustrated in Figure 7.1 for various amperometry-based methods. Determining a concentration from these signals requires counting events in time rather than measuring an average response.

Single-entity methods have however made relatively few inroads in the sensing of ultralow analyte concentrations. This may at first appear surprising: doesn't detecting single molecules represent the ultimate sensitivity? Indeed, the ability to detect a single analyte particle or molecule represents remarkable mass sensitivity for that analyte. One cannot detect fewer than one elementary entity. In practice, however, the goal is typically to determine the concentration of an analyte, and concentration sensitivity represents the key of merit. A high mass sensitivity does not necessarily translate into a high concentration

sensitivity. The very characteristics lending a high mass sensitivity to a transducer can even explicitly preclude a high concentration sensitivity.

We argue that SEE detectors are intrinsically handicapped in measuring low concentrations due to their small physical dimensions. Our main thesis is however that these limitations can be circumvented by employing large arrays of independently addressable transducers. Consistent with recent usage in both SEE and single-molecule optical measurements,[25-28] we employ the term 'digital sensing' to refer to this combination of single-entity, real-time and parallelized detection. This terminology evokes the high degree of integration characteristic of modern electronics. It also reflects the discrete nature of the output signals, which in an abstract sense consist of a stream of discrete events as a function of time rather than an averaged sensor response. This represents a more stringent use of the term compared to digital microfluidics[29,30] or digital ELISA,[31,32] where discrete events are usually detected via chemical post-amplification.

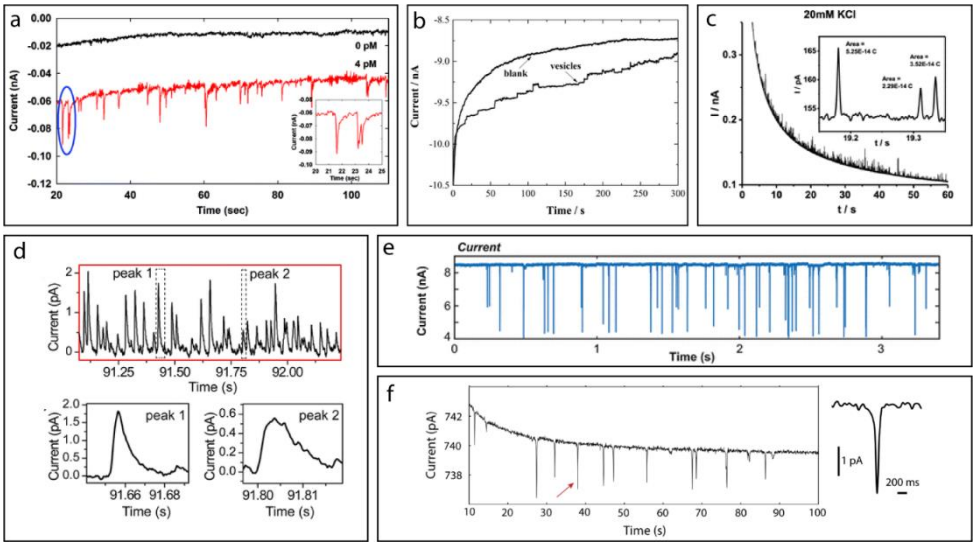

Figure 7.1. Examples of discrete signals in amperometry-based SEE. (a) Mediated faradaic impact: current spikes occur due to electrocatalytic water oxidation upon impact of IrOx nanoparticles on a NaBH4-treated Pt UME.[33] Adapted with permission from (Kwon, S. J.; Fan, F.-R. F.; Bard, A. J., Observing Iridium Oxide (IrOx) Single Nanoparticle Collisions at Ultramicroelectrodes. Journal of the American Chemical Society 2010, 132 (38), 13165-13167). Copyright (2010) American Chemical Society. (b) Current blockade impact: steps in the anodic current from oxidation of the $Fe(CN)6^{4-}$ mediator are observed upon impact of vesicles on a Pt ultramicroelectrode.[34] Adapted with permission from (Lebègue, E.; Anderson, C. M.; Dick, J. E.; Webb, L. J.; Bard, A. J., Electrochemical Detection of Single Phospholipid Vesicle Collisions at a Pt Ultramicroelectrode. Langmuir 2015, 31 (42), 11734-11739). Copyright (2015) American Chemical Society. (c) Direct faradaic impact: Ag nanoparticles are oxidized upon making contact with an electrode, leading to current spikes.[35]

Adapted with permission from (Li, X.; Batchelor-McAuley, C.; Compton, R. G., Silver Nanoparticle Detection in Real-World Environments via Particle Impact Electrochemistry. ACS Sensors 2019, 4 (2), 464-470). Copyright (2019) American Chemical Society. (d) Scanning electrochemical cell microscopy (SECCM): current spikes are observed when Au nanoparticles are immobilized upon an alkanethiol-modified Au electrode.[36] Adapted with permission from (Chen, C.-H.; Ravenhill, E. R.; Momotenko, D.; Kim, Y.-R.; Lai, S. C. S.; Unwin, P. R., Impact of Surface Chemistry on Nanoparticle–Electrode Interactions in the Electrochemical Detection of Nanoparticle Collisions. Langmuir 2015, 31 (43), 11932-11942). Copyright (2015) American Chemical Society. (e) Solid-state nanopore: transient dips occur in the ionic current through the (plasmonic) nanopore upon translocation of single DNA molecules.[37](https://pubs.acs.org/doi/10.1021/acs.nanolett.8b04146; further permissions related to the material excerpted should be directed to the ACS). (f) Electroosmotically-driven current blockade: current from oxidation of the ferrocene dimethanol mediator dips during convectively driven transient passage of polystyrene beads over a Pt ultramicroelectrode.[38] (https://pubs.acs.org/doi/10.1021/jacs.0c08450; further permissions related to the material excerpted should be directed to the ACS).

More precisely, we define a digital sensor as an ensemble of independent nodes, each consisting of a device capable of single-entity detection. In practice this corresponds to generating a (usually sudden) time-resolved signature each time that a microscopic event of interest takes place. Photomultiplier tubes and Geiger counters are classic examples that generate a burst of charge when a single photon or ionizing radiation particle impinges upon the detector. For an electrochemical sensor, each node consists of a separate SEE experiment that can be independently sampled and analyzed. In its simplest form, each feature in the node signal (such as the steps and pulses in Figure 7.1) can be assigned one-to-one to the occurrence of an event of interest (the binding of an analyte to a receptor, for example). More generally, the amplitude, duration and shape of single SEE events can be further analyzed to enhance specificity, as done for example in the analysis of nanopore signals.[6-9] Such fingerprinting can be employed to selectively ignore false positives from interfering species, suppress instrumental noise and eliminate baseline drift. Somewhat abstractly, the final output of the sensor as a whole can be considered to be the aggregate events from all of the nodes. In this sense the output consists of a sequence of times at which each event took place together with the nature of that event, from which analyte concentrations are inferred. Translating the raw signals from the individual nodes into event counts and combining this information into a total sensor output can be carried out as post-experimental analysis, although performing parts of it in real time can help mitigate the sheer volume of data.

It is not necessarily a priori obvious that digital sensing can deliver performance superior to that of conventional approaches, which are based on large detectors integrating over a large number of microscopic events. Here we first summarize fundamental challenges inherent to detecting ultra-low concentrations. We pay particular attention to the main limitations of single-entity methods, and address how parallelization can help lift some of the main obstacles. We then discuss the properties of the signals resulting from digital sensing. Finally,

we argue that modern electronics are poised to provide the ideal platform for realizing digital sensors, noting that this may involve a shift from popular amperometry-based SEE approaches to high-frequency methods. While our focus is on electrochemical sensors, many of the general concepts that we consider here apply equally well to miniaturized optical and mechanical transducers.

7.2 The need for parallelization

SEE methods typically rely on electrodes with critical dimensions of a size that is not much larger than the size of the target itself. Simply put, it is easier to detect a small change in an electrical signal when it is not superimposed on a much larger background signal and the associated noise. However, decreasing the size of the working electrode comes at a price as it can limit the ultimate achievable performance of a sensor in several ways. In this section we focus on the mechanisms by which minimization impacts theoretical detection limits.

First, decreasing the electrode size hinders mass transport of the analyte. Targets need to reach the sensor detection domain in order to be detected; the smaller the sensor, the lower the likelihood that a target will find the sensor in a given time interval. For nanoscale sensors, the time needed for analyte molecules to come into contact can become prohibitively large. This is best illustrated with a simple numerical example, as emphasized by Sheehan and Whitman.[39] The steady-state diffusive flux (in analytes/second), k_{diff}, to a miniaturized detector with characteristic lateral size d has the general form[40,41]

$$k_{\text{diff}} = 10^3 \cdot D N_A C \gamma d \qquad (1)$$

Here D is the diffusion coefficient of the analyte, N_A is Avogadro's number, C is the molar concentration of the analyte, d is the characteristic size of the detector and γ is a geometry-dependent factor of order unity (for example, $\gamma = 2$ for a shrouded disk of diameter *d*). The total flux is proportional to *d* and thus increases with increasing electrode size. Eq 1 is valid in the steady state, which is established after a brief transient with a duration comparable to the diffusion time, $d^2/4D$.[42] In practice, for miniaturized sensors this transient is too short to be accessed and eq 1 holds at essentially all times.

For small macromolecules ($D \approx 10^{-6}$ cm^2/s) at a low concentration of C = 1 pM diffusing to a nanoscale disk sensor ($d = 100$ nm), steady state is achieved on the time scale of 25 μs. The probability of even a single analyte reaching the electrode during this time is $\ll 1$. The steady-state flux then settles to a constant value of ~0.01 analytes/s. That is, one needs to wait on average ≈100 s between the moments when single analyte arrive at the detector. Lower concentrations or larger analytes with lower diffusion coefficients demand correspondingly longer times, placing increasing limitations on the average number of detection events expected for a given electrode size and measurement time.

The above observations may at first appear to contradict the rule of thumb that 'mass transport is more effective at miniaturized electrodes.' It is true that, based on eq 1, the analyte flux density scales as d^{-1} and thus increases upon decreasing the electrode size. But, when working at the single-analyte limit, what matters is the time needed for each analyte to reach the detector. This is determined by the total flux, not the flux density. Hence the measurement time increases with smaller detector size.

A second complication introduced by sensor miniaturization stems from the properties of chemical equilibria and kinetics. These can place additional – and often more severe – limitations on concentration sensitivity. As illustration, consider Langmuir kinetics[43] between an analyte at concentration C and a single receptor, as described by the equation

$$p = \frac{C}{K_D + C}\left(1 - e^{-t/\tau}\right) \qquad (2)$$

Here p is the probability of the receptor being occupied by an analyte at time t (starting from $p = 0$ at $t = 0$), K_D is the dissociation constant and τ is the time constant for the reaction. In terms of the association and dissociation rates, k_a (units $M^{-1}s^{-1}$) and k_d (units s^{-1}), respectively, the model parameters take the form $K_D = k_d/k_a$ and $\tau = (k_a C + k_d)^{-1}$.

Eq 2 indicates that at low concentration ($C \ll K_D$) and in equilibrium ($t \to \infty$) the probability of the receptor being occupied, $p \approx C/K_D$, is much smaller than unity. That is, a receptor is most likely to remain unoccupied even at equilibrium. For a device incorporating a large number of receptors, N_{rec}, the average number of occupied receptors is $\langle N_{\mathrm{occ}} \rangle = pN_{\mathrm{rec}}$. In order to have at least one receptor occupied on average ($\langle N_{\mathrm{occ}} \rangle = 1$), the minimum number of receptors is then $N_{\mathrm{rec}} = 1/p = K_D/C \gg 1$. If the detector is too small to accommodate this number of receptors, then $\langle N_{\mathrm{occ}} \rangle < 1$ and the sensor ceases to function in a conventional sense. In principle it is still possible to determine $\langle N_{\mathrm{occ}} \rangle$ when $\langle N_{\mathrm{occ}} \rangle < 1$ by measuring a time average over multiple association and dissociation cycles, but this usually requires an impractically long time.

Furthermore, the minimum requirement $\langle N_{\mathrm{occ}} \rangle \geq 1$ is highly optimistic. Analyte binding is a stochastic process taking place at independent receptors, and random fluctuations occur around the average occupancy $\langle N_{\mathrm{occ}} \rangle$. According to the binomial distribution, the root-mean-square fluctuation in the instantaneous value of the occupancy, N_{occ}, is $\Delta N_{\mathrm{occ}} = \sqrt{\langle N_{\mathrm{occ}} \rangle}$ when $p \ll 1$. In order to use a measurement of N_{occ} to deduce the analyte concentration C, it is therefore necessary to increase $\langle N_{\mathrm{occ}} \rangle$ to a point where the relative error $\Delta N_{\mathrm{occ}}/\langle N_{\mathrm{occ}} \rangle$ is sufficiently small. For example, based on the above, a 10% and 1% accuracy in the average occupancy $\langle N_{\mathrm{occ}} \rangle$ require $N_{\mathrm{rec}} = 10^2/p$ and $10^4/p$, respectively. Fitting these additional receptors onto the sensor increases its minimum size by a significant factor.

Finally, we have so far assumed that the receptors are in equilibrium with solution. Reaching equilibrium requires incubating the sample for a period equal to several times the relaxation

time τ. In the limit where $C \ll K_D$, the expression for τ reduces to $\tau \approx k_d^{-1}$. For molecules with a low dissociation rate, τ can thus prove prohibitively long (up to days). Alternatively, one does not wait for equilibrium and makes use of eq 2 to extract a concentration from the transient response. For short measurement times ($t \ll \tau$) and low concentrations, eq 2 reduces to $p \approx (C/K_D)(t/\tau)$. This occupancy is a factor of $t/\tau \ll 1$ smaller than the equilibrium result. Consequently, for a given desired average occupancy $\langle N_{\mathrm{occ}} \rangle$, the required number of receptors further increases by a factor $\tau/t \gg 1$.

Summarizing, low equilibrium occupancy and long equilibration times combine to place rather stringent limitations on the minimum size of a sensor. For example, substituting typical numbers for short DNA at a concentration of 1 pM, 10% accuracy and 100 s measurement time yields $N_{\mathrm{rec}} \geq (10^2)(K_D/C)(\tau/t) \approx 2 \times 10^7$. This estimate is based on representative values[44] of K_D = 0.2 nM and $\tau = 10^5$ s. Although specific values quoted in the literature vary substantially based on the specifics of different experiments, the conclusion that N_{rec} is a very large number holds generally. At optimal packing these receptors occupy ≈40 nm^2/receptor or ≈1000 μm^2 in total, corresponding to the area of a ≈36 μm diameter disk electrode. This footprint is much larger than the typical nanoscale dimensions of devices capable of single-entity detection. Conversely, detecting a mere 100 target molecules at such a large electrode is at present essentially impossible by purely electrochemical means.

While here we have focused solely on diffusive mass transport and first-order kinetics using order-of-magnitude estimates, these illustrate a more general pattern. On the time scales deemed desirable for point-of-need assays, the number of single-entity events expected for a nanoscale sensor easily becomes far smaller than unity, let alone large enough to provide sufficient statistics for an accurate measurement. While performance may be somewhat improved using convection, this is usually insufficient to significantly alter the picture sketched above. For a more extensive and quantitative discussion we refer the reader to the excellent review by Squires, Messinger and Manalis.[45]

These considerations lead to the conclusion that individual SEE detectors are largely unsuitable for detection at ultra-low analyte concentrations, while devices large enough to satisfy the mass transport and binding kinetics requirements are too large to serve as SEE detectors. The same reasoning however suggests that the main limitations can be overcome through the massive parallelization of SEE detectors. This is most readily achieved through pixelation: replacing the single large electrode with a dense array of many individually addressable small electrodes, or nodes, each capable of SEE detection.

Consider an array of N_{node} nodes arranged in the form of a disk, each consisting of a shrouded disk electrode of diameter d supporting N_{rec} receptors and separated by an average distance Δ. Trivially, the total number of receptors in the array is increased by a factor N_{node} compared to a single node. Mass transport is also substantially increased. When $N_{\mathrm{node}} \ll (\Delta/d - 1)^4$, each electrode behaves independently and obeys eq 1.[46] In this case the total rate of mass

transport is also boosted by a factor N_{node}. In the opposite limit where the number of nodes becomes large or the spacing between electrodes becomes small such that $N_{\mathrm{node}} \gg (\Delta/d-1)^4$, mass transport becomes limited by hemispherical diffusion from the far field to the array as a whole and k_{diff} increases by a large yet more modest factor $\Delta\sqrt{N_{\mathrm{node}}}/d$.[46] Interestingly, however, convective mass transport can be much more effectively employed in this last case due to the larger Peclet numbers associated with the diameter of the array compared to a single electrode.[47]

For illustration, consider again the numerical example above where 2×10^7 DNA receptors are required. For $d = 100$ nm electrodes this corresponds to $\approx 10^5$ electrodes. If these are positioned 1 μm apart, the array has a diameter of 360 μm. These parameters satisfy $N_{\mathrm{node}} \gg (\Delta/d-1)^4 = 6600$, hence the diffusion-limited flux is essentially the same as to a 360 μm electrode, yielding $k_{\mathrm{diff}} \approx 40$ analyte/s^{-1}. This is sufficient to accommodate the maximum binding rate $k_{\mathrm{bind}} = N_{\mathrm{node}} N_{\mathrm{rec}} k_a C = 1$ analyte/s.

In order to paint a more quantitative picture of the properties of digital sensors, we focus on an affinity sensor at low occupancy ($p \ll 1$). We ignore mass transport limitations and analyte unbinding, which corresponds to short times ($t \ll \tau \approx k_d^{-1}$). Under these assumptions, the analyte binding rate for one receptor is then given by $k_a C$ and the total binding rate is $k_{\mathrm{ideal}} = N_{\mathrm{node}} N_{\mathrm{rec}} k_a C$. The response of the sensor consists of a series of random events, or counts, as a function of time. This is illustrated in Figure 7.2a for two values of k_{ideal} using numerically generated data. Each trajectory has a random character that nonetheless reflects an average rate k_{ideal}. The time required to achieve a certain number of counts is different for each trajectory, but it fluctuates around a mean value such that the average response remains predictable. This is illustrated in Figure 7.2b and Figure 7.2c, which show histograms of the distribution of times required to reach a fixed number of events, $N_{\mathrm{event}} = 20$. These values cluster around a mean value but with a significant spread.

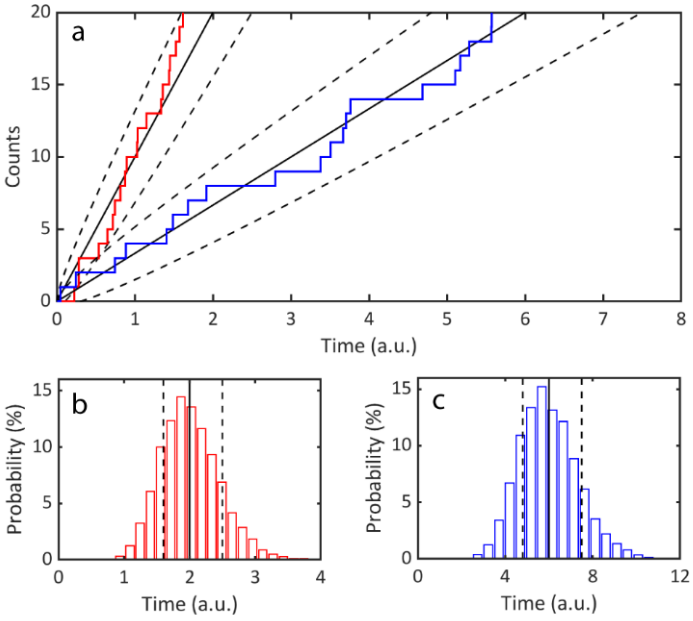

Figure 7.2. Simulated response of an ideal digital sensor. The sensor is described by a Poisson process with rate k_{ideal}. (a) Typical individual trajectories for $k_{\text{ideal}} = k_0$ (red) and $k_{\text{ideal}} = k_0/3$ (blue), where k_0 is an arbitrary rate constant. The solid black lines represent the average number of events at each time, $\langle N_{\text{event}} \rangle$. The dashed lines represent one standard deviation in N_{event} as predicted by Poisson statistics. The trajectories were generated numerically *via* a simulated Poisson process.[48] (b, c) Histograms showing the distribution of the time needed to generate 20 events for $k_{\text{ideal}} = k_0$ (b, red) and $k_{\text{ideal}} = k_0/3$ (c, blue) based on 10^4 trajectories.

This example demonstrates how an electrode array can allow simultaneously reconciling the demands of mass transport and chemical kinetics. More generally, the size and number of nodes, the geometry of the array and of the nodes, and the spacing between nodes can be concomitantly optimized using theoretically derived mass transport equations[46] or numerical simulations. This optimization process will necessarily be subject to constraints imposed by the nature of the SEE measurement, the contents of a node and the technology employed to implement the array.

7.3 Benefits of digital detection

Here we discuss qualitatively the potential gains made by employing SEE detection methods.

Insensitivity to baseline drift. An important requirement for detecting a low concentration is to be able to detect a response above the background or baseline signal. Background may result for example from parasitic electrochemical reactions or small offsets in the measurement electronics. If the background signal was perfectly stable, the ability to measure small changes in detection signal would be limited only by the resolution of the readout electronics. In practice, however, the baseline signal fluctuates due to, e.g., temperature variations, electrode aging, and the ubiquitous $1/f$ noise characteristic of nonequilibrium processes. This renders the smallest signals occurring over long time scales, such as occur in affinity sensors, essentially impossible to distinguish from baseline drift.

A SEE detector, on the other hand, is often relatively insensitive to baseline drift. This is because there exists a clear separation of time scales between abrupt SEE events and the (usually much slower) baseline fluctuations. Intuitively, it is clear that steps and spikes that occur on a sub-second time scale are easily identified against a smoothly varying background signal that evolves on the scale of minutes or longer. This remains true even when the amplitude of the discrete events is smaller than the amplitude of the slow background fluctuations.

Insensitivity to electrode fouling. In electrochemical methods, it is common for the surface of a working electrode to become fouled after prolonged exposure to a sample. In a conventional sensor, the corresponding change in sensitivity can lead to error. In digital sensing, slow changes in the response of individual nodes to discrete events do not a priori prevent identification. As long as the individual event signatures can be recognized, they can be counted and analyzed independently of their exact shape. This additional degree of robustness is especially relevant in analyses requiring long measurement times.

Accuracy. When considering the features of a digital sensor, it is crucial to make a distinction between the properties of the individual nodes and those of the sensor as a whole. Ideally, digital sensing would allow detecting every binding event and would exhibit no false positives from interfering species. In this idealized case the sensor could exhibit near-perfect accuracy (vide infra). Importantly, however, this would not require that the individual node signals (e.g., the current in an amperometric measurement) exhibit perfect accuracy. Since the role of the node signals is to allow the identification and counting of events, it is sufficient that the characteristic signature of an event can be reliably recognized. Offsets or distortion of the signal are tolerable, insofar as they are taken into consideration so as not to preclude event detection and identification. The absolute accuracy of the raw output signal of the node thus becomes largely irrelevant in determining the accuracy of the sensor as a whole. This reduces the demands on the node instrumentation required to achieve a high sensor accuracy.

Advanced signal processing. There has been considerable effort devoted to applying modern statistical methods to the analysis of single-entity measurements. As a primary example, so-called hidden Markov model descriptions[49,50] permit the construction of sophisticated models

of microscopic dynamics from complex time-resolved measurements even with limited a priori knowledge. These approaches have been extensively applied for example to the interpretation of single-ion-channel recordings[51] and Förster resonance energy transfer (FRET) measurements.[52,53] While so far underutilized in most SEE experiments, these methods can be harnessed in the future for interpreting signals in digital SEE sensing, with expected boosts in both sensitivity and selectivity.

7.4 Implementation of digital sensing

A very significant disadvantage of an electrochemical digital sensing architecture is the enormous increase in complexity associated with implementing a (very) large array of separately addressable SEE detectors. Approaches for doing so fall mostly outside the laboratory-based instrumentation typically associated with SEE.

Most high-quality electrodes employed for electrochemistry on the nanoscale rely on macroscopic techniques such as laser-assisted pulling. These are eminently unsuited to large-scale parallelization. Material-based methods for creating electrode arrays down to the nanoscale have become increasingly sophisticated, but separately reading out each electrode is challenging (although in principle possible, e.g., by optical methods[54]). Simple lithographically-based approaches, in which electrodes are patterned on the surface of a chip and passively connected to external instrumentation via individual wires,[55] are also unfeasible due to the sheer number of connections that would be required between the chip and the outside world.

One way we can begin to address this problem using a purely electrochemical strategy is to employ array architectures for measurements involving two working electrodes. For illustration, consider a generator-collector experiment, in which a species is electrogenerated at one electrode and collected at a second, nearby electrode. The measurement nodes are arranged on a two-dimensional square grid, as illustrated schematically in Figure 7.3a. Rather than connecting each electrode separately to the outside world, the generator electrode from each node is short-circuited with all the other generator electrodes from the same row and a single external connection exists for that row. The collector electrodes are similarly connected in a column-wise fashion (Figure 7.3b). During measurements, a single row is set to a generating potential while the remaining rows and all the columns are set to a collecting potential. In this way generation takes place only in the row being addressed. The collector current from each node in that row can then be measured by measuring the collector current through the corresponding column, even though each column is also connected to the collector electrodes from the inactive rows. In order to scan the whole array, the active row is cycled in time. For each row, readout of the collector current can be done for each column in succession, for several columns at a time, or for all columns in parallel. Such a square array

with N^2 nodes requires $2N$ wires, a factor N reduction when compared to the $2N^2$ wires needed to connect each electrode separately. This geometry lends itself well to a lithography-based approach in which the individual nodes and their interconnects are fabricated on an insulating substrate.

An important compromise in this approach is that only a subset of the nodes is being actively monitored at any given time. The SEE process under investigation must therefore be sufficiently slow that it can be resolved despite each node being only intermittently probed. Another issue is that the inactive nodes still contribute to the noise and background current of the column signals, degrading the overall noise properties of the measurement.

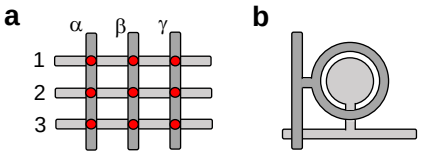

Figure 7.3. Two-dimensional array architecture. (a) Individual nodes (red dots) can be individually addressed via their row (1, 2, 3) and column (α, β, γ) interconnects. In a generator-collector experiment, all of the generator electrodes on the same row are excited simultaneously and the collector current for each node on that row can be read out via the corresponding column interconnect. Alternatively, in an active array, the row and column wires can control transistor switches to dynamically control which node(s) are active. (b) Example of a generator-collector node geometry in which a disk electrode acts as generator and a surrounding ring electrode acts as collector. The horizontal and vertical bars at the left and bottom represent the row and column interconnects, respectively.

A more general strategy is to separate the function of addressing individual nodes from that of performing the electrochemical measurement. This requires active switches being incorporated into the array to select which electrode(s) are polarized and/or read out. This approach lends itself naturally to an integrated circuit implementation in which the active elements take the form of transistors that are incorporated together with the electrodes and their interconnects on the same chip. Having taken that step, it becomes possible to implement additional functionality on the chip such as amplification and even digitization.

In recent decades, a wide variety of electrochemical instrumentation has been implemented using complementary metal-oxide-semiconductor (CMOS) technology, the workhorse of the semiconductors industry. While this field is far too broad to review here,[56] some recent examples of CMOS-based massively parallelized electrochemical devices include ion-sensitive field-effect transistors (ISFETs) for DNA sequencing,[57] microelectrode arrays (MEAs) for electrogenic cell recording and stimulation,[58,59] and high-density nanocapacitor arrays for high-frequency detection.[60] This directly exploits some of the strengths of CMOS technology, in particular the means to create miniaturized electrode structures (although this can require post-processing following standard CMOS fabrication), the ability to arrange

these in large arrays of separately addressable nodes, high switching speeds, and the flexibility to integrate additional functionality.

Implementing electrochemical instrumentation on chip may however entail significant compromises. For example, $1/f$ noise plays an increasingly large role upon decreasing transistor dimensions.[61] This directly impacts the noise properties of transimpedance amplifiers employed in amperometry (the method of choice for many SEE experiments, as illustrated in Figure 7.1). While $1/f$ noise is not a main limiting factor in many present-day implementations,[62] it can severely limit downscaling amperometric arrays to the sub-micron scale. This may ultimately favor transducers that are less sensitive to $1/f$ noise, such as high-frequency switched capacitor methods.[63,64]

7.5 Conclusions

SEE is a rapidly evolving sub-field that is extending fundamental understanding and pushing the capabilities of electrochemical techniques into new territory. While SEE detectors have exquisite mass sensitivity, translating this into a high concentration sensitivity still represents a formidable challenge. This is in no small part due to the size mismatch between typical SEE detectors and the much larger dimensions that are required to overcome the limitations imposed by mass transport and binding kinetics. Large-scale parallelization suggests a solution to this conundrum, but this comes at a significant increase in complexity and most likely requires implementing digital SEE sensing in the form of integrated circuits. This necessarily involves significant design compromises since microelectronic processing and circuit architectures are not always in harmony with electrode materials and instrumentation most commonly employed in electrochemistry.

A potentially disruptive factor that we have ignored in our analysis of mass transport and binding kinetics is targeted active transport. There is a growing set of methods in micro- and nanofluidics for selectively enriching the local concentration of target molecules at a sensor (e.g., isotachophoresis[65], ion concentration polarization focusing[66], AC electrokinetic methods[67]). These techniques are beneficial for both conventional and digital sensors, but in particular they may help alleviate the stringent requirements for implementing digital detection by decreasing the minimum number of nodes.

A key ingredient of (bio)sensors that has not yet been explicitly addressed at the experimental level for most SEE methods is receptor compatibility. So far, many SEE measurements have focused on the development of signal transduction methods with minimal attention to specificity. How best to couple an affinity-based assay to most SEE detection methods remains a largely open question. This is further complicated by the fact that electrochemical processes can locally influence biochemical kinetics, an encouraging example being the enhancement of the rate of DNA hybridization at an electrode under potential modulation.[68]

Can SEE-based digital (bio)sensors advance to the point where they can revolutionize trace-level detection? This is at the moment an open question. Most SEE methods are still at an early stage of development and the technical challenges ahead are very significant. By comparison, optical methods provide a more straightforward entry for the development of digital sensing concepts. This is in no small part due to digital cameras that permit high-sensitivity measurements over large areas and with high spatial resolution. The SEE equivalent of mature CCD and CMOS image sensors does not exist yet. It is difficult to underestimate the potential of CMOS technology, however. Past the initial hurdle of development, in terms of both time and resources, all-electrical assays incorporating colossal numbers of active elements could be mass produced at low cost. For this to happen, however, will require continued close collaboration between nanoelectrochemists and circuit engineers.

7.6 References

(1) Baker, L. A. Perspective and Prospectus on Single-Entity Electrochemistry. *J. Am. Chem. Soc.* **2018**, *140*, 15549-15559.
(2) Coulter, W. H. Means for counting particles suspended in a fluid. **US Pat., 2656508, 1953**.
(3) Li, J.; Stein, D.; McMullan, C.; Branton, D.; Aziz, M. J.; Golovchenko, J. A. Ion-Beam Sculpting at Nanometre Length Scales. *Nature* **2001**, *412*, 166-169.
(4) Li, J.; Gershow, M.; Stein, D.; Brandin, E.; Golovchenko, J. A. DNA Molecules and Configurations in A Solid-State Nanopore Microscope. *Nat. Mater.* **2003**, *2*, 611-615.
(5) Kasianowicz, J. J.; Brandin, E.; Branton, D.; Deamer, D. W. Characterization of Individual Polynucleotide Molecules Using A Membrane Channel. *Proc. Natl. Acad. Sci. U.S.A.* **1996**, *93*, 13770-13773.
(6) Clarke, J.; Wu, H.-C.; Jayasinghe, L.; Patel, A.; Reid, S.; Bayley, H. Continuous Base Identification for Single-Molecule Nanopore DNA Sequencing. *Nat. Nanotechnol.* **2009**, *4*, 265-270.
(7) Deamer, D.; Akeson, M.; Branton, D. Three Decades Of Nanopore Sequencing. *Nat. Biotechnol.* **2016**, *34*, 518-524.
(8) Jain, M.; Koren, S.; Miga, K. H.; Quick, J.; Rand, A. C.; Sasani, T. A.; Tyson, J. R.; Beggs, A. D.; Dilthey, A. T.; Fiddes, I. T.; et al. Nanopore Sequencing and Assembly of A Human Genome with Ultra-Long Reads. *Nat. Biotechnol.* **2018**, *36*, 338-345.
(9) Depledge, D. P.; Srinivas, K. P.; Sadaoka, T.; Bready, D.; Mori, Y.; Placantonakis, D. G.; Mohr, I.; Wilson, A. C. Direct Rna Sequencing on Nanopore Arrays Redefines the Transcriptional Complexity of A Viral Pathogen. *Nat. Commun.* **2019**, *10*, 754.
(10) Liu, Y.; Li, M.; Zhang, F.; Zhu, A.; Shi, G. Development of Au Disk Nanoelectrode Down to 3 nm in Radius for Detection of Dopamine Release from a Single Cell. *Anal. Chem.* **2015**, *87*, 5531-5538.
(11) Luo, L.; White, H. S. Electrogeneration of Single Nanobubbles at Sub-50-nm-Radius Platinum Nanodisk Electrodes. *Langmuir* **2013**, *29*, 11169-11175.

(12) Neher, E.; Sakmann, B. Single-Channel Currents Recorded from Membrane of Denervated Frog Muscle Fibres. *Nature* **1976**, *260*, 799-802.
(13) Hamill, O. P.; Marty, A.; Neher, E.; Sakmann, B.; Sigworth, F. J. Improved Patch-Clamp Techniques for High-Resolution Current Recording from Cells and Cell-Free Membrane Patches. *Pflügers Archiv* **1981**, *391*, 85-100.
(14) Liu, H. Y.; Fan, F. R. F.; Lin, C. W.; Bard, A. J. Scanning Electrochemical and Tunneling Ultramicroelectrode Microscope for High-Resolution Examination of Electrode Surfaces in Solution. *J. Am. Chem. Soc.* **1986**, *108*, 3838-3839.
(15) Itaya, K.; Tomita, E. Scanning Tunneling Microscope for Electrochemistry - A New Concept for The in Situ Scanning Tunneling Microscope in Electrolyte Solutions. *Surf. Sci.* **1988**, *201*, L507-L512.
(16) Ebejer, N.; Schnippering, M.; Colburn, A. W.; Edwards, M. A.; Unwin, P. R. Localized High Resolution Electrochemistry and Multifunctional Imaging: Scanning Electrochemical Cell Microscopy. *Anal. Chem.* **2010**, *82*, 9141-9145.
(17) Kleijn, S. E. F.; Lai, S. C. S.; Miller, T. S.; Yanson, A. I.; Koper, M. T. M.; Unwin, P. R. Landing and Catalytic Characterization of Individual Nanoparticles on Electrode Surfaces. *J. Am. Chem. Soc.* **2012**, *134*, 18558-18561.
(18) Bentley, C. L.; Kang, M.; Unwin, P. R. Scanning Electrochemical Cell Microscopy: New Perspectives on Electrode Processes in Action. *Curr. Opin. Electrochem.* **2017**, *6*, 23-30.
(19) Fan, F. R. F.; Bard, A. J. Electrochemical Detection of Single Molecules. *Science* **1995**, *267*, 871-874.
(20) Zevenbergen, M. A. G.; Singh, P. S.; Goluch, E. D.; Wolfrum, B. L.; Lemay, S. G. Stochastic Sensing of Single Molecules in a Nanofluidic Electrochemical Device. *Nano Lett.* **2011**, *11*, 2881-2886.
(21) Quinn, B. M.; van't Hof, P. G.; Lemay, S. G. Time-resolved Electrochemical Detection of Discrete Adsorption Events. *J. Am. Chem. Soc.* **2004**, *126*, 8360-8361.
(22) Xiao, X.; Bard, A. J. Observing Single Nanoparticle Collisions at An Ultramicroelectrode by Electrocatalytic Amplification. *J. Am. Chem. Soc.* **2007**, *129*, 9610-9612.
(23) Zhou, Y. G.; Rees, N. V.; Compton, R. G. The Electrochemical Detection and Characterization of Silver Nanoparticles in Aqueous Solution. *Angew. Chem., Int. Ed.* **2011**, *50*, 4219-4221.
(24) Banks, C. E.; Rees, N. V.; Compton, R. G. Sonoelectrochemistry understood via Nanosecond voltammetry: sono-emulsions and the measurement of the potential of zero charge of a solid electrode. *J. Phys. Chem. B.* **2002**, *106*, 5810-5813.
(25) Visser, E. W. A.; Yan, J.; van Ijzendoorn, L. J.; Prins, M. W. J. Continuous Biomarker Monitoring By Particle Mobility Sensing With Single Molecule Resolution. *Nat. Commun.* **2018**, *9*, 2541.
(26) Nouri, R.; Tang, Z.; Guan, W. Calibration-Free Nanopore Digital Counting of Single Molecules. *Anal. Chem.* **2019**, *91*, 11178-11184.
(27) Jing, W.; Wang, Y.; Yang, Y.; Wang, Y.; Ma, G.; Wang, S.; Tao, N. Time-Resolved Digital Immunoassay for Rapid and Sensitive Quantitation of Procalcitonin with Plasmonic Imaging. *ACS Nano* **2019**, *13*, 8609-8617.

(28) Huang, Q.; Li, N.; Zhang, H.; Che, C.; Sun, F.; Xiong, Y.; Canady, T. D.; Cunningham, B. T. Critical Review: Digital Resolution Biomolecular Sensing for Diagnostics and Life Science Research. *Lab Chip.* **2020**, *20*, 2816-2840.
(29) Teh, S.-Y.; Lin, R.; Hung, L.-H.; Lee, A. P. Droplet Microfluidics. *Lab Chip.* **2008**, *8*, 198-220.
(30) Guo, M. T.; Rotem, A.; Heyman, J. A.; Weitz, D. A. Droplet Microfluidics for High-Throughput Biological Assays. *Lab Chip.* **2012**, *12*, 2146-2155.
(31) Rissin, D. M.; Kan, C. W.; Campbell, T. G.; Howes, S. C.; Fournier, D. R.; Song, L.; Piech, T.; Patel, P. P.; Chang, L.; Rivnak, A. J.; et al. Single-Molecule Enzyme-Linked Immunosorbent Assay Detects Serum Proteins at Subfemtomolar Concentrations. *Nat. Biotechnol.* **2010**, *28*, 595-599.
(32) Cohen, L.; Walt, D. R. Single-Molecule Arrays for Protein and Nucleic Acid Analysis. *Annu. Rev. Anal. Chem.* **2017**, *10*, 345-363.
(33) Kwon, S. J.; Fan, F.-R. F.; Bard, A. J. Observing Iridium Oxide (IrOx) Single Nanoparticle Collisions at Ultramicroelectrodes. *J. Am. Chem. Soc.* **2010**, *132*, 13165-13167.
(34) Lebègue, E.; Anderson, C. M.; Dick, J. E.; Webb, L. J.; Bard, A. J. Electrochemical Detection of Single Phospholipid Vesicle Collisions at a Pt Ultramicroelectrode. *Langmuir* **2015**, *31*, 11734-11739.
(35) Li, X.; Batchelor-McAuley, C.; Compton, R. G. Silver Nanoparticle Detection in Real-World Environments via Particle Impact Electrochemistry. *ACS Sens.* **2019**, *4*, 464-470.
(36) Chen, C.-H.; Ravenhill, E. R.; Momotenko, D.; Kim, Y.-R.; Lai, S. C. S.; Unwin, P. R. Impact of Surface Chemistry on Nanoparticle–Electrode Interactions in the Electrochemical Detection of Nanoparticle Collisions. *Langmuir* **2015**, *31*, 11932-11942.
(37) Shi, X.; Verschueren, D. V.; Dekker, C. Active Delivery of Single DNA Molecules into a Plasmonic Nanopore for Label-Free Optical Sensing. *Nano Lett.* **2018**, *18*, 8003-8010.
(38) Moazzenzade, T.; Yang, X.; Walterbos, L.; Huskens, J.; Renault, C.; Lemay, S. G. Self-Induced Convection at Microelectrodes via Electroosmosis and Its Influence on Impact Electrochemistry. *J. Am. Chem. Soc.* **2020**, *142*, 17908-17912.
(39) Sheehan, P. E.; Whitman, L. J. Detection Limits for Nanoscale Biosensors. *Nano Lett.* **2005**, *5*, 803-807.
(40) Liu, X.; Lu, J.; Cha, C. Square Root Law for the Diffusion Current at A Microelectrode. *J. electroanal. chem. interfacial electrochem.* **1990**, *294*, 289-292.
(41) Oldham, K. B. Steady-State Voltammetry at Microelectrodes of Arbitrary Shape. *J. Electroanal. Chem.* **1992**, *323*, 53-76.
(42) Bard, A. j.; Faulkner, L. R. *Electrochemical Methods: Fundamentals and Applications*; John Wiley & Sons, 2001.
(43) Langmuir, I. The Adsorption of Gases on Plane Surfaces of Glass, Mica and Platinum. *J. Am. Chem. Soc.* **1918**, *40*, 1361-1403.
(44) Liebermann, T.; Knoll, W.; Sluka, P.; Herrmann, R. Complement Hybridization from Solution to Surface-Attached Probe-Oligonucleotides Observed by Surface-Plasmon-Field-Enhanced Fluorescence Spectroscopy. *Colloids Surf. A: Physicochem. Eng. Asp.* **2000**, *169*, 337-350.
(45) Squires, T. M.; Messinger, R. J.; Manalis, S. R. Making It Stick: Convection, Reaction and Diffusion in Surface-Based Biosensors. *Nat. Biotechnol.* **2008**, *26*, 417.
(46) Morf, W. E. Theoretical Treatment of the Amperometric Current Response of Multiple Microelectrode Arrays. *Anal. Chim. Acta* **1996**, *330*, 139-149.

(47) Sokolov, S. V.; Bartlett, T. R.; Fair, P.; Fletcher, S.; Compton, R. G. Femtomolar Detection of Silver Nanoparticles by Flow-Enhanced Direct-Impact Voltammetry at a Microelectrode Array. *Anal. Chem.* **2016**, *88*, 8908-8912.
(48) Kostiuchenko, Z. A.; Zhang, B.; Lemay, S. G. Stochastic Charge Fluctuations in Bipolar Electrodes. *J. Phys. Chem. C.* **2016**, *120*, 22777-22783.
(49) Bilmes, J. A Gentle Tutorial of the EM Algorithm and its Application to Parameter Estimation for Gaussian Mixture and Hidden Markov Models. Techanical Report, University of California Berkeley: 1998.
(50) Eddy, S. R. What Is A Hidden Markov Model? *Nat. Biotechnol.* **2004**, *22*, 1315-1316.
(51) Chung, S. H.; Moore, J. B.; Xia, L.; Premkumar, L. S.; Gage, P. W. Characterization of Single Channel Currents Using Digital Signal-Processing Techniques Based on Hidden Markov-Models. *Philos. Trans. R. Soc. B: Biol. Sci.* **1990**, *329*, 265-285.
(52) McKinney, S. A.; Joo, C.; Ha, T. Analysis of Single-Molecule FRET Trajectories Using Hidden Markov Modeling. *Biophys. J.* **2006**, *91*, 1941-1951.
(53) Bronson, J. E.; Fei, J. Y.; Hofman, J. M.; Gonzalez, R. L.; Wiggins, C. H. Learning Rates and States from Biophysical Time Series: A Bayesian Approach to Model Selection and Single-Molecule FRET Data. *Biophys. J.* **2009**, *97*, 3196-3205.
(54) Fan, Y.; Anderson, T. J.; Zhang, B. Single-Molecule Electrochemistry: from Redox Cycling to Single Redox Events. *Curr. Opin. Electrochem.* **2018**, *7*, 81-86.
(55) Rassaei, L.; Singh, P. S.; Lemay, S. G. Lithography-Based Nanoelectrochemistry. *Anal. Chem.* **2011**, *83*, 3974-3980.
(56) Li, H. T.; Liu, X. W.; Li, L.; Mu, X. Y.; Genov, R.; Mason, A. J. CMOS Electrochemical Instrumentation for Biosensor Microsystems: A Review. *Sensors* **2017**, *17*, 26.
(57) Rothberg, J. M.; Hinz, W.; Rearick, T. M.; Schultz, J.; Mileski, W.; Davey, M.; Leamon, J. H.; Johnson, K.; Milgrew, M. J.; Edwards, M.; et al. An Integrated Semiconductor Device Enabling Non-Optical Genome Sequencing. *Nature* **2011**, *475*, 348-352.
(58) Ballini, M.; Muller, J.; Livi, P.; Chen, Y. H.; Frey, U.; Stettler, A.; Shadmani, A.; Viswam, V.; Jones, I. L.; Jackel, D.; et al. A 1024-Channel CMOS Microelectrode Array With 26,400 Electrodes for Recording and Stimulation of Electrogenic Cells In Vitro. *IEEE J. Solid-State Circuit.* **2014**, *49*, 2705-2719.
(59) Tsai, D.; Sawyer, D.; Bradd, A.; Yuste, R.; Shepard, K. L. A Very Large-Scale Microelectrode Array for Cellular-Resolution Electrophysiology. *Nat. Commun.* **2017**, *8*, 1802.
(60) Laborde, C.; Pittino, F.; Verhoeven, H. A.; Lemay, S. G.; Selmi, L.; Jongsma, M. A.; Widdershoven, F. P. Real-Time Imaging Of Microparticles And Living Cells With Cmos Nanocapacitor Arrays. *Nat. Nanotechnol.* **2015**, *10*, 791-795.
(61) Tuinhout, H.; Duijnhoven, A. Z. Evaluation of 1/f noise variability in the subthreshold region of MOSFETs. In *2013 IEEE International Conference on Microelectronic Test Structures (ICMTS)*, 25-28 March 2013, 2013; pp 87-92.
(62) Hartel, A. J. W.; Shekar, S.; Ong, P.; Schroeder, I.; Thiel, G.; Shepard, K. L. High Bandwidth Approaches in Nanopore and Ion Channel Recordings - a Tutorial Review. *Anal. Chim. Acta.* **2019**, *1061*, 13-27.
(63) Widdershoven, F.; Cossettini, A.; Laborde, C.; Bandiziol, A.; Swinderen, P. P. v.; Lemay, S. G.; Selmi, L. A CMOS Pixelated Nanocapacitor Biosensor Platform for High-Frequency Impedance Spectroscopy and Imaging. *IEEE Trans. Biomed. Circuits Syst.* **2018**, *12*, 1369-1382.

(64) Hu, K.; Kennedy, E.; Rosenstein, J. K.; Ieee. High Frequency Dielectric Spectroscopy Array with Code Division Multiplexing for Biological Imaging. In *2019 Ieee Biomedical Circuits and Systems Conference*, Biomedical Circuits and Systems Conference, 2019.
(65) Smejkal Petr, P.; Bottenus, D.; Breadmore, M. C.; Guijt, R. M.; Ivory, C. F. Microfluidic Isotachophoresis: A Review. *Electrophor. 34*, 1493-1509.
(66) Berzina, B.; Anand, R. K. Tutorial Review: Enrichment and Separation af Neutral and Charged Species by Ion Concentration Polarization Focusing. *Anal. Chim. Acta.* **2020**, *1128*, 149-173.
(67) Salari, A.; Thompson, M. Recent Advances in AC Electrokinetic Sample Enrichment Techniques for Biosensor Development. *Sens. Actuators B Chem.* **2018**, *255*, 3601-3615.
(68) Tymoczko, J.; Schuhmann, W.; Gebala, M. Electrical Potential-Assisted DNA Hybridization. How to Mitigate Electrostatics for Surface DNA Hybridization. *ACS Appl. Mater. Interfaces.* **2014**, *6*, 21851-21858.

Summary and outlook

8.1 Summary

Early-stage cancer detection is crucial for the successful treatment of patients and reduction of the mortality rate.[1] Liquid biopsy as a non-invasive method enables detection of tumor-derived biomarkers in biofluids such as blood, plasma, and urine.[1-6] However, detecting cancer markers at an early stage is not straightforward because the concentration of biomarkers is very low. Hence, biosensors with a high sensitivity are required for this aim. Driven by the progress in nanotechnology, cancer research has witnessed the development of methods that employ micro and nanoscale sensing elements for biosensing applications. However, these devices are still in the research phase. Employing miniaturized sensors requires methodologies for improving the sensitivity and selectivity of biosensors to fulfil detection at ultralow concentrations and provide early-stage diagnostics.[1,7]

Single-entity electrochemistry (SEE) constitutes a category of highly sensitive systems that employ miniaturized electrodes for the detection of individual analytes.[8] In one example of SEE, the collision of analytes at the electrode surface can be detected real-time as discrete events in the current-time responses. Among SEE methods, particle-blockade impact electrochemistry studies the collision of non-electroactive particles to the micro or nanoelectrode surface, where individual collisions lead to step-like decreases in the current-time response.[9]

Detecting at the single-entity level is the ultimate mass sensitivity that can be imagined for a sensing system. However, this improved sensitivity can be misleading when these methods are employed for the detection of analytes at ultralow concentrations. Employing a miniaturized transducer decreases the probability of interaction between the target and the electrode surface.[10] Hence, the time scale of the biosensing becomes impractical and the stability of the recognition elements and the target biomolecules becomes an issue. For instance, detecting a DNA oligonucleotide (20 nt) may take ~1 hour to ~1 day for a 1 fM sample using transducers with a size of 1 μm to 10 nm (see *Chapter 2*). Hence, despite the high mass sensitivity, employing micro and nanoscale elements for detecting biomolecules cannot achieve biosensing at ultralow concentrations on a practical time scale. *Chapter 2* in this thesis discusses this trade-off situation and the challenges of biomolecular detection at ultralow concentrations. This chapter proposes parallelization of the miniaturized transducing elements as a methodology to overcome the mass transport limitation in single-entity sensing. In addition, different SEE methods and their mechanism of signal transduction were discussed in this chapter.

In the experimental section of the thesis, the aim was to study current-blockade particle-impact electrochemistry and to investigate utilizing microparticles as a signal amplification label for the detection of ssDNA oligonucleotides. However, investigating blockade impact shed light on different aspects of this method and also touched upon various fundamental aspects of electrochemical measurements with microelectrodes.

As the first empirical observation, the collision of DNA-coated microparticles to a DNA-coated surface caused atypical signals in the current-time response: spike-like decreases. Further investigations showed that the same signals could be observed for pristine particles on a pristine electrode. However, spikes could be observed only when measurements were performed at low salt concentrations. Simultaneous optical-electrochemical measurements and analysis of the trajectory of particles showed that particles can be repelled from the surface after the collision. Repelling a negatively charged particle from an electrode oxidizing a mediator molecule cannot be explained by electrophoresis. *Chapter 3* explains this phenomenon as a consequence of electrochemically induced convection by electroosmosis at microelectrodes, and this effect can be observed in the trajectory of particles in blockade impact electrochemistry. The results show that electroosmotic flow can be the dominant form of transport in measurements at low salt concentrations.

Chapter 4 aimed to improve the signal size uniformity in blockade impact electrochemistry. Blockade impact measurements with a disk UME cause a broad distribution of current step sizes for particles of a given diameter.[11,12] This is because the flux of the redox mediator is not uniform at the surface of the disk UME. Hence, the current density at the edge of the disk is higher than at the center. As a consequence of the inhomogeneous flux, the current step size depends on the particle collision site on the UME in such a way that landed particles at the edge of the disk cause larger signals. This discrepancy complicates signal identification and processing in single-entity measurements. In this chapter, a microfabricated ring UME was developed to possess a similar current density on the electrode surface. Hence, particles landing anywhere on the ring UME led to similar current blockade signals. The ring geometry exhibited a narrower distribution of signal sizes and a higher relative size sensitivity compared to the conventional disk UME. The second consequence of non-uniform current density in a disk UME is the migration of collided particles from the center to the edge of the disk, which leads to false positive signals.[11,13] The ring geometry can intrinsically solve this issue because the current density is similar anywhere on the ring surface.

Chapter 5 aimed to develop a mediator-free single-entity electrochemical (bio)sensor. An intrinsic aspect of amperometric electrochemical methods is the use of a redox mediator for signal generation. In blockade impact electrochemistry, oxidation or reduction of redox mediators is hampered by microparticle collision and leads to discrete signals. In this chapter, the measurements showed that blockade impact can be performed without employing a synthetic redox mediator. Microparticles can block the oxygen reduction reaction (ORR) on

the surface of a UME and generate discrete current steps. In addition, it was shown that the concentration of dissolved oxygen in physiological solutions such as PBS is high enough to generate signals in blockade impact electrochemistry. Circumventing the employment of redox mediators in single-entity measurements opens routes toward mediator-free detection in solutions such as cell culture media where employing synthetic mediators is not favored.

As represented in *Chapters 3*, *4*, and *5*, blockade impact electrochemistry is mostly performed at low salt concentrations. This is because, at low salt conditions, migration becomes the dominant form of particle transport, enabling the detection of particles at ultralow concentrations on a practical time scale.[9,13,14] However, a low salt solution is not a proper medium when the aim is biosensing. In this regime, both the immobilized receptors and the target biomolecules may lose their native structures, resulting in a failed biorecognition. In the case of ssDNA receptors, due to the highly negative charges of the DNA backbone, a given ssDNA shows a lower hybridization rate at low salt in comparison to physiological salt concentrations. Hence, one has to increase the concentration of salt close to the physiological salt concentrations to guarantee the specificity of the biorecognition process.
Employing a physiological salt concentration in blockade impact changes the regime of transport of microparticles to a diffusion-limited regime.[9,13,14] Hence, for a given concentration of microparticles that provides a high collision frequency in a practical time scale at low salt, the measurement may require days to observe the same frequency of signals. This regime of transport can complicate utilizing microparticles as a label in a sandwich assay, the most common methodology in label-based surface biosensors.[15] In a real-time sandwich assay, the concentration of the label should be saturated to not become the limiting factor and ensure binding and signal generation at a low target concentration. This requirement can be problematic when microparticles with a slow diffusion rate are utilized as the label in blockade impact sensors. On the other hand, due to the size dependence of non-specific adhesion forces, increasing the concentration of these big microparticles can increase the probability of non-specific adsorption of these particles at the UME surface, leading to false-positive signals.

To avoid this issue, in *Chapter 6*, a particle-based competitive assay was designed for the detection of the ssDNA oligonucleotide where specifically anchored particles can be dissociated from the surface upon target DNA binding. The assay was designed based on the concept of toehold-mediated strand displacement. Different surface chemistries, such as PLL-OEG-Tz[16] and thiol monolayers, were used as the surface modification methods in this assay. The results showed that employing microparticles as a label in competitive assays requires strategies for suppressing non-specific adsorption. To improve the particle dissociation efficiency in PLL-OEG-Tz chemistry, an anionic polymer, polyacrylic acid (PAA) was employed to suppress non-specific electrostatic forces. In addition, in this chapter, the coupled resonator model in QCM-D was used to explain the specificity of particle binding.

As a proof of concept, a particle-based competitive assay was used for the detection of ssDNA by blockade impact electrochemistry. However, as discussed in *Chapter 2*, although single-entity electrochemistry can be optimized for biosensing applications, SEE sensors need to be parallelized to accomplish biosensing at ultralow concentrations. *Chapter 7* investigates this idea in detail and introduces the concept of *digital electrochemical biosensing* in which SEE elements are employed as separately addressable transducing elements. This chapter explains that this parallelized SEE sensor can achieve the ultimate concentration sensitivity because of benefits from both the high mass sensitivity in single elements and overcoming the mass transport problem because of the availability of the sensing elements in parallel.

8.2. Outlook

Optimizing SEE methods, in particular blockade impact electrochemistry, for biomolecular detection at ultralow concentrations requires strategies for improving sensitivity and selectivity. These strategies include methodologies to improve the sensitivity of the micro/nanoelectrodes, the specificity of particle binding, the compatibility of faradaic reactions, and the durability and stability of sensors for sensing real biological samples. In this outlook, the future directions in biosensing with impact electrochemistry is discussed, together with their limitations and challenges associated with particle-based biosensing using impact electrochemistry.

8.2.1 Single-biomolecule detection in a microparticle-based assay

As explained in *Chapter 6*, employing microparticles as the signal amplification label in a displacement assay needs to be optimized to suppress the non-specific adsorption of particles. On the other hand, the methodology needs to be improved to fulfil single-molecule detection in such a way that the binding of a single DNA target dissociates a single particle from the surface. As described in *Chapter 6*, lowering the density of dsDNA in the particle-substrate interface showed a lower binding specificity and consequently particle dissociation. Hence, it seems that dsDNA molecules may play a role as spacers and help the dissociation of particles. A suggestion for utilizing the same strategy at lower densities of DNA receptors can be employing dummy dsDNA molecules as the spacer in the gap between the particle and the surface. Hence, particles at a very low density of receptors can bind to the surface by a single dsDNA receptor, and a high density of dsDNA spacers prevents non-specific adsorption of particles.

Although decreasing the density of dsDNA receptors can push the assay to a single-molecule level, low densities of receptors decrease the probability of target binding. Hence, an efficient scheme can be achieved by employing smaller particles such as nanoparticles at a high density of dsDNA. With such a design, both single-molecule detection and the mass transport

problem can be solved. In addition, employing smaller particles can diminish the issues regarding the size-dependent, non-specific adsorption of particles, as well as slow diffusion of labels. However, employing nanoparticles in blockade impact electrochemistry needs smaller electrodes possessing a high mass sensitivity.

8.2.2 Increasing the mass sensitivity in blockade impact sensors

The average signal size, ΔI, in blockade impact electrochemistry is approximately proportional to the projected area of the particle on the electrode surface. Hence, a non-electroactive particle with a minimum diameter is required for blocking the redox flux to a UME surface and generating a discrete signal. For instance, although a 100-nm insulating particle can block the mediator flux on a 10-µm disk UME, this blockade cannot easily be observed in the current-time response because the ΔI is smaller than the noise level. Hence, smaller electrodes are required to guarantee the required particle-to-electrode ratio and to generate signals with a high signal-to-noise ratio. However, there is a limitation in patterning sub-micron planar disk electrodes by conventional lithography techniques. In *Chapter 4*, a ring geometry was suggested for blockade impact measurements. Although the main goal of designing this device was to achieve uniform signals, the ring geometry also showed a bigger relative step size in comparison to the disk UME with a similar diameter. Even higher sensitivities can be achieved by decreasing the thickness of the ring in the metal sputtering step. In addition, employing electron-beam lithography facilitates the fabrication of electrodes with nanoscale diameters. The resulting nanoring electrodes with a small diameter and ultrathin thicknesses can be used to detect insulating nanoparticles. This high sensitivity enables single-molecule detection with nanoparticles at higher densities of receptors where the transport of the target molecules to the receptor is not a limiting factor. In addition, the issues regarding the non-specific adsorption and slow diffusion of particles can be diminished when nanoparticles are employed as the label in a highly sensitive blockade impact sensor.

The ultimate sensitivity can be achieved by using this geometry as a label-free blockade sensor where binding or dissociation of biomolecules can block the mediator flux and leads to discrete signals in the current-time response. However, as explained in *Chapter 2*, employing smaller electrodes will suffer from the mass transport limitations that need to be diminished by parallelizing these electrodes.

8.2.3 Parallelizing miniaturized electrodes

As explained in *Chapters 2 and 7*, miniaturized electrodes need to be parallelized to overcome mass transport limitations. This methodology can increase the probability of interaction between the target molecules and the sensing elements. However, the main limitation in parallelizing electrodes that are patterned on the chip surface is connecting them to the outside world *via* individual wires, which makes parallelization impractical

for amperometric sensors like blockade impact electrochemistry. As an alternative method, complementary metal-oxide-semiconductor (CMOS)-based massively parallelized electrochemical devices, with the ability to parallelize large arrays of separately addressable nodes can be used to fulfil this approach.[17]

8.2.4 Mediator-free electrochemical biosensing

Blockade impact electrochemistry employs different oxidative and reductive faradaic reactions for detecting particles. However, optimizing this method for biosensing applications requires selecting a proper reaction with a minimum effect on biorecognition. For example, employing an intercalating redox mediator may affect the overall reaction rate in a DNA displacement sensor. In particle displacement assays, employing an oxidation reaction yields the continuous generation of positively charged species that may cause non-specific adsorption of negatively charged particles on the surface and prevents particle dissociation upon DNA displacement. *Chapter 5* presented the possibility of employing a biocompatible mediator, dissolved O_2 in physiological solutions, in blockade impact electrochemistry. As a future work, this reaction can be utilized in a particle-based DNA displacement assay. However, it should be considered that the electric field generated by this reductive reaction may repel specifically anchored particles from the surface before DNA binding. Hence, a particle-based DNA displacement assay with a reductive reaction such as ORR requires designing primary duplexes with a small dissociation rate constant that guarantees long-lasting particles on the surface before target DNA binding.

8.2.5 Digital biosensing in complex biofluids

Complex biofluids such as blood plasma contain a high content of proteins, vesicles, and cell debris that can interfere with the biosensing procedure. The main issue in electrochemical biosensing is that a high concentration of these adsorbents may cause electrode fouling. In amperometric sensors, they can adsorb to the electrode surface, and by inhibiting the faradaic reactions and electron transfer decrease the current level. In addition, these substances can increase the background noise level in electrical measurements, diminishing the signal-to-noise ratio. This issue can be more problematic when miniaturized electrodes are employed as the transducing elements where electrode fouling decreases the current level significantly. An advantage of amperometric digital biosensors is that discrete signals can be detected even at very low current levels. For instance, in blockade impact electrochemistry, a measurement is valid as long as the step size, ΔI , is bigger than the noise level. Hence, biosensing can be continued even when the faradaic reaction is hampered significantly due to the non-specific adsorption of proteins and cell debris. However, extended exposure to complex biofluids can eventually cause electrode fouling and decrease the signal-to-noise ratio, even in a digital biosensor. Parallelization, as explained in *Chapters 2* and *7*, can decrease the time scale of

biosensing and indirectly diminish this issue. In addition, other strategies like employing reductive reactions such as ORR (*Chapter 4*) may help to decrease the adsorption of negatively charged proteins such as albumin (the most abundant protein in the blood plasma) on the electrode surface. However, non-specific adsorption of biomolecules and debris caused by other forces, such as Van der Waals and hydrophobic forces, remains an issue. Hence, parallelized digital biosensors, despite the benefits of rapid detection and the ability to detect discrete events at low current levels, require surface modification methods with improved antifouling properties to suppress adsorption and electrode fouling and improve the stability and longevity of the biosensor. In addition, the implementation of a parallelized blockade impact or CMOS-based digital biosensors in a medical device may need pre-purification steps to decrease the concentration of proteins, vesicles, and debris, and diminish the electrode fouling to ensure highly selective and sensitive biosensing.

8.3 References

(1) Arya, S. K.; Bhansali, S. Lung Cancer and Its Early Detection Using Biomarker-Based Biosensors. *Chem. Rev.* **2011**, *111*, 6783-6809.
(2) Ignatiadis, M.; Sledge, G. W.; Jeffrey, S. S. Liquid Biopsy Enters The Clinic — Implementation Issues And Future Challenges. *Nat Rev Clin Oncol* **2021**, *18*, 297-312.
(3) Cescon, D. W.; Bratman, S. V.; Chan, S. M.; Siu, L. L. Circulating tumor DNA and liquid biopsy in oncology. *Nat Cancer* **2020**, *1*, 276-290.
(4) Siravegna, G.; Marsoni, S.; Siena, S.; Bardelli, A. Integrating Liquid Biopsies Into The Management Of Cancer. *Nat Rev Clin Oncol* **2017**, *14*, 531-548.
(5) Toden, S.; Goel, A. Non-Coding Rnas As Liquid Biopsy Biomarkers In Cancer. *Br J Cancer* **2022**, *126*, 351-360.
(6) Ding, Z.; Wang, N.; Ji, N.; Chen, Z.-S. Proteomics Technologies For Cancer Liquid Biopsies. *Mol Cancer* **2022**, *21*, 53.
(7) Hinestrosa, J. P.; Kurzrock, R.; Lewis, J. M.; Schork, N. J.; Schroeder, G.; Kamat, A. M.; Lowy, A. M.; Eskander, R. N.; Perrera, O.; Searson, D.; et al. Early-Stage Multi-Cancer Detection Using An Extracellular Vesicle Protein-Based Blood Test. *Commun Med* **2022**, *2*, 29.
(8) Baker, L. A. Perspective and Prospectus on Single-Entity Electrochemistry. *J. Am. Chem. Soc.* **2018**, *140*, 15549-15559.
(9) Quinn, B. M.; van't Hof, P. G.; Lemay, S. G. Time-Resolved Electrochemical Detection Of Discrete Adsorption Events. *J. Am. Chem. Soc.* **2004**, *126*, 8360-8361.
(10) Sheehan, P. E.; Whitman, L. J. Detection Limits for Nanoscale Biosensors. *Nano Lett.* **2005**, *5*, 803-807.
(11) Fosdick, S. E.; Anderson, M. J.; Nettleton, E. G.; Crooks, R. M. Correlated Electrochemical and Optical Tracking of Discrete Collision Events. *J. Am. Chem. Soc.* **2013**, *135*, 5994-5997.
(12) Deng, Z.; Elattar, R.; Maroun, F.; Renault, C. In Situ Measurement of the Size Distribution and Concentration of Insulating Particles by Electrochemical Collision on Hemispherical Ultramicroelectrodes. *Anal. Chem.* **2018**, *90*, 12923-12929.

(13) Boika, A.; Thorgaard, S. N.; Bard, A. J. Monitoring the Electrophoretic Migration and Adsorption of Single Insulating Nanoparticles at Ultramicroelectrodes. *J. Phys. Chem. B* **2013**, *117*, 4371-4380.
(14) Lemay, S. G.; Renault, C.; Dick, J. E. Particle mass transport in impact electrochemistry. *Curr. Opin. Electrochem.* **2023**, *39*, 101265.
(15) Shen, J.; Li, Y.; Gu, H.; Xia, F.; Zuo, X. Recent Development of Sandwich Assay Based on the Nanobiotechnologies for Proteins, Nucleic Acids, Small Molecules, and Ions. *Chem. Rev.* **2014**, *114*, 7631-7677.
(16) Di Iorio, D.; Marti, A.; Koeman, S.; Huskens, J. Clickable poly-l-lysine for the formation of biorecognition surfaces. *RSC Advances* **2019**, *9*, 35608-35613.
(17) Laborde, C.; Pittino, F.; Verhoeven, H. A.; Lemay, S. G.; Selmi, L.; Jongsma, M. A.; Widdershoven, F. P. Real-Time Imaging Of Microparticles And Living Cells With Cmos Nanocapacitor Arrays. *Nat. Nanotechnol.* **2015**, *10*, 791-795.

Samenvatting

Vroegtijdige kankerdetectie is cruciaal voor een succesvolle behandeling van patiënten en vermindering van het sterftecijfer. Vloeistofbiopsie als een niet-invasieve methode maakt detectie mogelijk van tumor-afgeleide markers in een lichaamssappen, zoals bloed, plasma en urine. Het opsporen van kankermarkers in een vroeg stadium is echter niet eenvoudig omdat de concentratie van deze markers erg laag is. Hiervoor zijn dus biosensoren met een hoge gevoeligheid nodig.

Single-entity electrochemistry (SEE) vormt een categorie van zeer gevoelige systemen die geminiaturiseerde elektroden gebruiken voor de detectie van individuele analyten. Detecteren op het niveau van één entiteit (bv. molecuul of nanodeeltje) is de ultieme gevoeligheid die men zich kan voorstellen voor een sensorsysteem. Echter, deze hoge gevoeligheid kan misleidend zijn wanneer deze methoden worden gebruikt voor de detectie van analyten bij ultra-lage concentraties. Het gebruik van een geminiaturiseerde transducer verkleint de kans op interactie tussen de entiteit en het elektrode-oppervlak. Daarom kunnen, ondanks de hoge massagevoeligheid, elementen op micro- en nanoschaal deze ultra-lage concentraties niet detecteren op een praktische tijdschaal. *Hoofdstuk 2* in dit proefschrift stelt parallellisatie van de geminiaturiseerde meetelementen voor als een methodologie om deze beperking te overwinnen.

Binnen de SEE-methoden bestudeert *blockade impact electrochemistry* de stochastische botsing van niet-elektroactieve deeltjes met het micro- of nano-elektrode-oppervlak, waarbij individuele botsingen leiden tot een stapsgewijze afname van de elektrische stroom in de tijd. De experimentele hoofdstukken van dit proefschrift zijn gericht op het bestuderen *van blockade impact electrochemistry* en het gebruik ervan als een SEE-methodologie voor de digitale detectie van enkelstrengs DNA (ssDNA).

In *Hoofdstuk 3* zijn de effecten van oplossingen met lage zoutconcentraties onderzocht in *blockade impact electrochemistry*. In dit hoofdstuk gaf het onderzoeken van de signaalvorm en de trajecten van microdeeltjes inzicht in een fundamenteel aspect van elektrochemische metingen bij lage zoutgehaltes, namelijk de elektro-osmotische stroming (EOF). Dit onderzoek liet zien hoe Faraday-reacties in laag-zoutregimes convectie veroorzaken in de vloeistof rond een *ultramicroelectrode* (UME) als gevolg van EOF. De resultaten toonden aan dat elektro-osmotische stroming de dominante vorm van transport kan zijn bij metingen bij lage zoutconcentraties.

Hoofdstuk 4 is gericht op het verbeteren van de uniformiteit van de signaalsterkte in *blockade impact electrochemistry*. In dit hoofdstuk is een microschaal-gefabriceerde

ringvormige UME ontwikkeld om een homogene stroomdichtheid op het elektrode-oppervlak te verkrijgen. De ringgeometrie vertoonde een smallere verdeling van signaalsterktes en een hogere relatieve gevoeligheid in vergelijking met de conventionele schijfvormige UME.

Hoofdstuk 5 had tot doel een mediator-vrije SEE-(bio)sensor te ontwikkelen. Een intrinsiek aspect van amperometrische elektrochemische methoden is het gebruik van een redox-mediator voor het genereren van signalen. In dit hoofdstuk is de zuurstofreductiereactie (*oxygen reduction reaction*, ORR) gebruikt in *blockade impact electrochemistry* om het gebruik van synthetische mediatoren te omzeilen. De metingen toonden aan dat microdeeltjes de flux van O_2 op het oppervlak van een UME kunnen blokkeren en zo discrete stroomsignalen kunnen genereren.

In *Hoofdstuk 6* werd een deeltjes-gebaseerde competitieve assay ontworpen voor de detectie van een ssDNA-oligonucleotide waarbij specifiek verankerde deeltjes kunnen worden losgekoppeld van het oppervlak na binding aan het ssDNA. De motivatie voor deze studie was het ontwerpen van een elektrochemische detectiemethode die biomoleculen op een digitale aan/uit-manier kan detecteren. Ter onderbouwing van het concept is deze assay gebruikt voor de detectie van ssDNA door *blockade impact electrochemistry*. Zoals besproken in hoofdstuk 2, moeten SEE-sensoren worden geparallelliseerd om biosensing bij ultra-lage concentraties te bewerkstelligen. In *hoofdstuk 7* is dit idee in detail onderzocht en is het concept van digitale elektrochemische biosensing geïntroduceerd waarin SEE-elementen worden gebruikt als afzonderlijk adresseerbare meetelementen. Bovendien is er uitgelegd dat deze geparallelliseerde SEE-sensor de ultieme concentratiegevoeligheid kan bereiken vanwege de voordelen van zowel de hoge massagevoeligheid in afzonderlijke geminiaturiseerde elementen als het overwinnen van het massatransportprobleem vanwege de beschikbaarheid van de parallelle sensorelementen.

Scientific output

Papers:

Moazzenzade, T., Yang, X., Walterbos, L. , Huskens, J. , Renault, C. , & Lemay, S. G. Self-Induced Convection at Microelectrodes via Electroosmosis and Its Influence on Impact Electrochemistry. Journal of the American Chemical Society. 2022, 142, 17908-17912. https://doi.org/10.1021/jacs.0c08450.

Moazzenzade, T., Walstra, T., Yang, X., Huskens, J,. & Lemay, S. G. Ring ultramicroelectrodes for current-blockade particle-impact electrochemistry. Analytical chemistry. 2022, 94, 28, 10168–10174. doi.org/10.1021/acs.analchem.2c01503.

Moazzenzade, T. , Huskens, J. , & Lemay, S. G. Stochastic electrochemistry at ultralow concentrations: The case for digital sensors. Analyst. 2020, 145, 750-758. https://doi.org/10.1039/c9an01832h.

Lemay, S. J. G. , & Moazzenzade, T. (2021). Single-Entity Electrochemistry for Digital Biosensing at Ultralow Concentrations. Analytical chemistry. 2021, 93, 9023-9031. https://doi.org/10.1021/acs.analchem.1c00510.

Moazzenzade, T.; Huskens, J.; Lemay, S. G. Utilizing the oxygen reduction reaction in particle impact electrochemistry: a step toward mediator-free digital electrochemical sensors. *ACS Omega*. 2023, https://doi.org/10.1021/acsomega.3c03576.

Moazzenzade, T.; Lemay, S. G.; Huskens, J. Designing a microparticle-based competitive displacement assay for the detection of ssDNA (Manuscript in preparation).

Conference talks:

Digital detection of ssDNA *via* Blockade Impact Electrochemistry. Human Electrochemistry 2022, Wageningen, Netherlands.

Self-Induced Convection at Microelectrodes via Electroosmosis and Its Influence on Impact Electrochemistry. Elecnano 2020, Paris, France (online).

Poster presentations:

Moazzenzade, T.; Huskens, J.; Lemay, S. G. Digital detection of DNA *via* blockade impact electrochemistry. BioEL 2022, Kirgberg in Tirol, Austria.

Moazzenzade, T., Yang, X., Walterbos, L. , Huskens, J. , Renault, C. , & Lemay, S. G.Self-Induced Convection at Microelectrodes via Electroosmosis and Its Influence on Impact Electrochemistry. NWO chain 2020, Veldhoven, The Netherlands.

Moazzenzade, T.; Nieuwenhuis, A. F.; Reurslag, C.; Duarte Sanches, D.F.; Lemay, S. G. Stochastic electrochemistry: the case for digital sensors. MESA+ Conference, 2019, Enschede, The Netherlands.

M.J. Goodwin, R.W. Kolman, T. Moazzenzade, J. Movilli, Fl. Falke, G.A.J. Besselink, J.J.L.M. Cornelissen, A. Rozzi, R. Corradini, S,G. Lemay, L.I. Segerink, J. Huskens. Enabling biosensing with Poly-L-lysin. MESA+ Conference, 2019, Enschede, The Netherlands.

Acknowledgment

I am immensely grateful to my supervisors, **Serge** and **Jurriaan**, whose support and guidance have been instrumental throughout my doctoral journey. Their deep knowledge, expertise, and dedication have shaped my research in immeasurable ways. Without their invaluable mentorship and encouragement, this thesis would not have been possible. Their guidance has been pivotal in making this doctoral pursuit a fulfilling and transformative experience, and I am truly honored to have had the opportunity to work with such outstanding mentors.

Serge, I would like to extend my heartfelt appreciation to you for your exceptional mentorship and support. I am thankful for your keen insights, which challenged me to think critically and pushed the boundaries of my understanding. I am thankful for your patience and encouragement during challenging times, which kept me motivated and focused. Moreover, your willingness to spare time for detailed discussions and constructive feedback has immensely enriched the quality of my work. Thank you, Serge, for being an integral part of this chapter in my life and for making it an extraordinary one. I am truly fortunate to have had you as my supervisor and will forever cherish the experience and wisdom gained under your guidance.

Jurriaan, I want to express my profound gratitude to you for your consistent support and encouragement throughout my doctoral journey. Your approachability and open-door policy fostered a collaborative and intellectually stimulating environment, allowing fruitful discussions and brainstorming sessions. I deeply appreciate the time and effort you invested in reviewing my work, offering constructive feedback, and guiding me to refine my research methodology. Your ability to see the bigger picture and provide insightful advice has been truly invaluable. Working with you has been an enriching experience that will undoubtedly leave a lasting impact on my academic and professional journey.

Dear committee members, prof. dr. **H. Zuilhof**, dr. **F. Kanoufi**, dr. ir. **S. Faez**, prof. dr. ir. **P. Jonkheijm**, and prof. dr. ir. **L.I. Segerink,** I want to express my appreciation for taking the time to review and evaluate my work. Your valuable feedback and thoughtful suggestions have been invaluable in refining my research and enhancing the quality of the thesis.

I want to express my heartfelt gratitude to my colleagues in the Bioelectronics (**BE**) group, **Ab, Daniel, Mohammad, Selvaraj, Suria,** and all students and researchers who joined BE during my Ph.D. Throughout these years, you have been more than just friends; you have been an invaluable support system and an integral part of my academic and personal life. Together, we have tackled complex problems, celebrated successes, and navigated through challenges, always inspiring each other to strive for excellence.

Thank you, **Ab**, for your invaluable contributions to our research group and for being a wonderful colleague. Your responsiveness, positive attitude, and willingness to lend a helping hand have created a collaborative and supportive environment within the group. I am honored to have had the opportunity to work alongside you and to having shared this transformative experience with such an exceptional colleague.

Daniel, our shared office space became more than just a place to work; it became a hub of intellectual exchange that made the entire Ph.D. experience truly special. Beyond our academic pursuits, I am grateful for the countless moments we spent sharing our favorite music, recommending novels and poems to each other. These moments of shared joy and cultural exploration added a unique dimension to our friendship, making our bond even more meaningful.

Mohammad, your presence and friendship have been a constant source of support during both the highs and lows of this journey. Your genuine kindness, sense of humor, and intellectual curiosity have made this Ph.D. experience unforgettable. Our shared love for Persian poems created bonds that extended beyond academia, making our friendship all the more special.

Surya, your unique blend of scientific expertise and artistic creativity has added a special dimension to the group, and I want to express my heartfelt appreciation for the friendship we have cultivated.

Jacopo, **Daniele**, **Ruben, Nico, Hazal,** and all friends and colleagues in the **MNF** group, I extend my deepest appreciation for your friendship and academic support. The memories we created together will be cherished for a lifetime, and I am truly fortunate to have shared this experience with such remarkable individuals. Thank you for being an integral part of my Ph.D. journey and for making it truly memorable.

Being the daily supervisor of MSc and BSc students has been an enriching experience for me. **Xiaojun, Luna, Tieme,** and **Reinder,** your collaboration, curiosity, and hard work have been a significant contribution to the success of our research, and I am thankful for the opportunity to work with you. I am excited to see the contributions you will make to the scientific community, and I am proud to have been part of your academic growth.

Jurriaan, Serge, Loes, Albert, Dodo, Nienke, and all the **Weijerhorst** team members, your diverse expertise brought a unique perspective to our research discussions and paved the way for innovative solutions to complex challenges. Our biweekly meetings served as the cornerstone of our collaboration, providing a platform for open and constructive discussions. Thanks for your commitment to advancing the field of biosensing.

Richard, Marcel, Ab, and the entire technical team in MNF, BE, and the **MESA+** cleanroom. Your commitment to maintaining a well-organized research environment was crucial in my work processes, allowing me to focus on the core aspects of my research. **Nicole**, **Izabel**, and **Marthe**, your commitment and organizational skills have played a pivotal role in ensuring the smooth functioning of administrative tasks, allowing me to focus on my research without unnecessary distractions.

I also want to express my gratitude to my previous colleagues, and my friends in the **MCS** group; **Han**, **Niels**, **Erwin**, **Stefan**, and **Yasser**. The experiences, knowledge, and skills I gained during my time in MCS have been invaluable in my research, and I am thankful for the enriching experience.

Yasser, your friendship, support, and presence throughout this Ph.D. journey have been a constant source of motivation. Your infectious enthusiasm and positive outlook on life have brightened even the toughest days. The encouragement you have given me to stay resilient and persevere through challenges has made all the difference in my pursuit of this Ph.D. I am grateful for the countless hours of conversations, and shared memories that have made this journey not only academically rewarding but also personally fulfilling.

To my family:

I want to express my deepest gratitude to my parents. **Pedar** and **Madar**, your unwavering love, support, and endless sacrifices have been the driving force behind my academic pursuit, and I am profoundly thankful for everything you have done for me. You have been my constant pillars of strength from the very beginning. Your guidance, wisdom, and encouragement have been instrumental in shaping me into the person I am today. The freedom you provided allowed me to explore different fields, make my own decisions, and learn from both successes and setbacks, all of which have been essential to my personal and intellectual growth. I am forever grateful for the values you instilled in me and the life lessons you taught me.

Dear **grandfather**, your endless support and love throughout my life have been a guiding light, and I am profoundly thankful for all that you have done for me. Your belief in my potential and your words of wisdom motivated me to strive for excellence in everything I did, including my Ph.D. studies. Your kindness and strength of character have left a lasting impact on my life.

My dear uncle **Moslem**, your support during my education has been a pivotal force that guided me towards finding my academic path. Your intellectual guidance, vast knowledge, and experience have provided me with insights and perspectives that have enriched my life, shaped my thinking, and expanded my horizons.

My dear sisters **Zarvandokht, Zahra, Nastaran, Kimia,** and my dear family members **Ali** and **Mahoora**, you have been my closest confidants and friends. I want to thank all of you for being the pillars of support in my life. Your constant encouragement during both the highs and lows of this journey have made all the difference. **Mehrnoosh**, I thank you for your presence and your supports during this time.

My dear spouse **Narges**, I want to thank you from the bottom of my heart for standing by me with unwavering love. Your support and understanding have been the foundation upon which I built my academic pursuit, and I am profoundly grateful for all that you have done for me. Your belief in my abilities, even during times of self-doubt, has given me the strength to overcome challenges and stay focused on my research goals. Throughout these years, we have walked this academic path hand in hand, supporting each other's dreams and aspirations. I am immensely proud of your own pursuit of knowledge and your commitment to excellence in your own Ph.D. journey. Your dedication to your research has always been a true inspiration to me. I know that you will shine brightly and make a significant impact in your field of research. I am truly blessed to have you as my wife, friend, and lovely mother of our child.

As I conclude this Ph.D. journey, I want to dedicate a special acknowledgment to the light of my life, **Setiya**. My universe, you have brought immeasurable joy and love into my life. From the moment you came into this world, you have filled my heart with an overwhelming sense of love and purpose. Your curious eyes and smile have been a constant source of inspiration. One day, as you grow older, you will look back on this time, knowing that you were the guiding light in your parent's academic and personal journey.

With all my love,

Taghi (Keykhosro)